Department of Micro and Nanosciences

Thin film technology for chemical sensors

Antti J. Niskanen

Aalto University

DOCTORAL DISSERTATIONS

Aalto University publication series
DOCTORAL DISSERTATIONS 146/2011

Thin film technology for chemical sensors

Antti J. Niskanen

Doctoral dissertation for the degree of Doctor of Science in Technology to be presented with due permission of the School of Electrical Engineering for public examination and debate in the Large Seminar Hall of Micronova at the Aalto University School of Electrical Engineering (Espoo, Finland) on the 27th of January 2012 at 12 noon.

Aalto University
School of Electrical Engineering
Department of Micro and Nanosciences
Microfabrication Group

Supervisor
Prof. Pekka Kuivalainen

Instructor
Prof. Sami Franssila

Preliminary examiners
Prof. Steven M. George, University of Colorado at Boulder, USA
Prof. Keijo Haapakka, University of Turku, Finland

Opponent
Prof. Jürgen Brugger, École Polytechnique Fédérale de Lausanne, Switzerland

Aalto University publication series
DOCTORAL DISSERTATIONS 146/2011

ISBN 978-952-60-4450-7 (printed)
ISBN 978-952-60-4451-4 (pdf)
ISSN-L 1799-4934
ISSN 1799-4934 (printed)
ISSN 1799-4942 (pdf)

Unigrafia Oy
Helsinki 2011

Finland

The dissertation can be read at http://lib.tkk.fi/Diss/

441 697
Printed matter

Author
Antti J. Niskanen

Name of the doctoral dissertation
Thin film technology for chemical sensors

Publisher School of Electrical Engineering

Unit Department of Micro and Nanosciences

Series Aalto University publication series DOCTORAL DISSERTATIONS 146/2011

Field of research Semiconductor technology

Manuscript submitted 6 June 2011 **Manuscript revised** 5 December 2011

Date of the defence 27 January 2012 **Language** English

☐ **Monograph** ☒ **Article dissertation (summary + original articles)**

Abstract

Microfabrication and thin film technologies were applied in the fabrication of miniaturized chemical sensors. Two types of devices were developed: an electrochemiluminescence device utilizing tunnel-emitted hot electrons, and a microhotplate semiconductor gas sensor with an atomic layer deposited (ALD) tin dioxide sensing film.

The hot electron-induced electrochemiluminescence (HECL) device is an integrated microelectrode device that combines an insulator-covered working electrode and a platinum counter electrode on a single chip. Two types of fluidic systems were integrated on the same type of electrode chip: either an enclosed sample chamber made of polydimethylsiloxane (PDMS) elastomer, or hydrophobic sample confinement on the chip surface. Different metals were tested as the working electrode, and different types of insulator films made by various methods were tested as the tunneling dielectric, to determine the optimal working electrode structures for HECL. These were then used in the integrated microelectrode devices, which were fabricated on silicon and glass substrates. A variety of electrode geometries were tested with the different fluidic systems, and sub-nanomolar sensitivity and wide dynamic range were demonstrated with the best devices. Ongoing work with polymeric substrates is briefly presented.

In the review, latest results are presented on the restoration of the hydrophilic properties of enclosed PDMS microfluidic channels. While a PDMS surface quickly reverts to its naturally hydrophobic state, thus preventing capillary filling, this plasma treatment enables capillary filling even after extended periods of storage.

The gas sensor is a microhotplate (MHP) device, utilizing a tin dioxide sensing layer deposited by ALD for the first time in a MHP sensor. Unconventional solutions were developed for the fabrication sequence to accommodate the demands of the deposition method. Also, metallizations and intermetal dielectrics not commonly used in MHP devices were tested to enable rapid processing of prototype devices with available methods and equipment. Fast response to various analyte gases, as well as good recovery and short-term stability were observed, demonstrating the potential of ALD tin dioxide films in gas sensor applications.

Keywords ultrathin insulating films, electrochemiluminescence, microhotplate gas sensor, atomic layer deposition

ISBN (printed) 978-952-60-4450-7 **ISBN (pdf)** 978-952-60-4451-4

ISSN-L 1799-4934 **ISSN (printed)** 1799-4934 **ISSN (pdf)** 1799-4942

Location of publisher Espoo **Location of printing** Helsinki **Year** 2011

Pages 156 **The dissertation can be read at** http://lib.tkk.fi/Diss/

A! Aalto-yliopisto

Tiivistelmä

Aalto-yliopisto, PL 11000, 00076 Aalto www.aalto.fi

Tekijä
Antti J. Niskanen

Väitöskirjan nimi
Ohutkalvoteknologian käyttö kemiallisissa antureissa

Julkaisija Sähkötekniikan korkeakoulu

Yksikkö Mikro- ja nanotekniikan laitos

Sarja Aalto University publication series DOCTORAL DISSERTATIONS 146/2011

Tutkimusala Puolijohdeteknologia

Käsikirjoituksen pvm 06.06.2011 **Korjatun käsikirjoituksen pvm** 05.12.2011

Väitöspäivä 27.01.2012 **Kieli** Englanti

☐ **Monografia** ☒ **Yhdistelmäväitöskirja (yhteenveto-osa + erillisartikkelit)**

Tiivistelmä

Mikrovalmistus- ja ohutkalvoteknologioita hyödynnettiin pienikokoisten kemiallisten anturien valmistuksessa. Työssä kehitettiin kahdenlaisia antureita: kuumien elektronien aiheuttamaan elektrokemiluminesenssiin perustuvia antureita, sekä atomikerroskasvatuksella (ALD:llä) valmistettua tinadioksidiohutkalvoa käyttävä mikrovalmistettu kaasuanturi.

Kuumien elektronien aiheuttamaan elektrokemiluminesenssiin perustuvassa anturissa on samalle sirulle integroitu sekä ohuella eristekalvolla päällystetty työelektrodi, että platinaohutkalvosta valmistettu vastaelektrodi. Sirulle on myös valmistettu kahdenlaisia rakenteita nesteen käsittelyä varten: polydimetyylisiloksaanista (PDMS:stä) valmistettuja suljettuja nestekammioita, sekä hydrofobisia rakenteita sirun pinnalla. Useita materiaaleja kokeiltiin työelektrodeissa, tavoitteena löytää elektrokemiluminesenssin kannalta tehokkain elektrodirakenne. Näitä materiaaleja käytettiin integroiduissa elektrodisiruissa, joita valmistettiin sekä pii- että lasikiekoille. Useita eri elektrodigeometrioita testattiin erilaisten nesteenkäsittelyrakenteiden kanssa, ja parhailla geometrioilla saavutettiin alle nanomolaarisia herkkyyksiä. Muovisille alustoille valmistetuista komponenteista esitetään myös alustavia tuloksia.

Yhteenveto-osassa esitetään uusimpia, vielä julkaisemattomia tuloksia PDMS:stä valmistetun nestekammion pinnan palauttamisesta hydrofiiliseksi. PDMS:n pinta palautuu luonnostaan hydrofobiseksi, mikä estää kammion täyttymisen pelkällä kapillaarivoimalla. Tässä esitetyllä plasmakäsittelyllä PDMS-kammion saa täyttymään pelkällä kapillaarivoimalla myös pitkän säilytyksen jälkeen.

Kaasuanturikomponentti on mikrolämpölevytyyppinen, ja siinä käytetään tinadioksidia kaasuherkkänä materiaalina. Tinadioksidi on valmistettu atomikerroskasvatuksella ensimmäistä kertaa tämäntyyppisessä anturissa. Tämän mahdollistamiseksi komponentin valmistusprosessissa tarvittiin useita erikoisia ratkaisuja. Lisäksi, mikrolämpölevyssä käytettiin poikkeuksellisia materiaaleja ja menetelmiä mahdollistamaan nopea valmistus käytettävissä olevilla laitteilla. Valmiilla komponenteilla mitattiin nopeita vasteaikoja eri kaasuille, täydellistä palautumista altistuksen jälkeen, sekä vakaita ominaisuuksia lyhyellä aikavälillä. Tämä osoittaa ALD-menetelmän sopivuuden kaasuanturikäytössä.

Avainsanat ultraohuet eristekalvot, elektrokemiluminesenssi, mikrovalmistettu kaasuanturi, atomikerroskasvatus

ISBN (painettu) 978-952-60-4450-7 **ISBN (pdf)** 978-952-60-4451-4

ISSN-L 1799-4934 **ISSN (painettu)** 1799-4934 **ISSN (pdf)** 1799-4942

Julkaisupaikka Espoo **Painopaikka** Helsinki **Vuosi** 2011

Sivumäärä 156 **Luettavissa verkossa osoitteessa** http://lib.tkk.fi/Diss/

Preface

This thesis is the result of multiple lucky coincidences and plenty of collaboration with people from different fields. First and foremost, I offer my warmest thanks to Tiina Ylinen-Hinkka, my chemist colleague, without whose tireless work performing luminescence measurements on countless series of samples, some even during her leaves of absence, none of this could ever have materialized. My thanks also to Professor Sakari Kulmala, whose pet subject hot electron electrochemiluminescence was—a few samples of thermally oxidized silicon led to a long and fruitful collaboration on the subject, and returned me in a sense from microfabrication back to chemistry. Sakari also plays a mean electric guitar. His performance of *Sunshine of your love* rules.

Many of my colleagues in the Microfabrication Group and the staff of TKK Micronova provided crucial expertise and support in the processing of my samples, but all of them deserve special thanks for creating a fun and inspirational atmosphere to work in. I can state with the experience of thousands of coffee breaks, you are a wonderful bunch of people. I would also like to thank my supervisor Sami Franssila for his unending support and enthusiasm for my research, Professor Pekka Kuivalainen for enjoyable sailing trips, and my pre-examiners, Professors Steven M. George and Keijo Haapakka, for their encouraging remarks on my thesis manuscript.

For the research effort into the *Lakana* gas sensors, which ended all too soon, my thanks to Aapo Varpula, Mikko Utriainen, Gomathi Natarajan, David C. Cameron, Sergey Novikov and Veli-Matti Airaksinen.

The most important factor behind the existence of this thesis, however, is attributed to my parents Jouni and Riitta, who planted in me my interest in science and technology,[†] and my love and respect for nature, two of the most defining aspects of who I am today. I cannot express enough thanks in this limited space for the learning environment and opportunities you have provided me.

Finally, to my brother Sampo (a true scientist) and to all my friends, thanks for all the ~~fish~~ fun times. That's the important stuff in life. (Fish are good also.)

Espoo, 29. 11. 2011

Antti J. Niskanen

[†]See *e.g.* J. J. Notkin, S. Gulkin, *(The How and Why Wonder Book of) Electricity*, Wonder Books, New York, 1960.

Contents

List of Publications

This thesis consists of an overview and of the following publications which are referred to in the text by their Roman numerals.

I Q. Jiang, J. Suomi, M. Håkansson, A. J. Niskanen, M. Kotiranta, S. Kulmala, Cathodic electrogenerated chemiluminescence of $Ru(bpy)_3^{2+}$ chelate at oxide-coated heavily doped silicon electrodes, *Analytica Chimica Acta* **541** (2005) 159–165.

II J. Suomi, M. Håkansson, Q. Jiang, M. Kotiranta, M. Helin, A. J. Niskanen, S. Kulmala, Time-resolved detection of electrochemiluminescence of luminol, *Analytica Chimica Acta* **541** (2005) 167–169.

III A. J. Niskanen, T. Ylinen-Hinkka, S. Kulmala, S. Franssila, Ultrathin tunnel insulator films on silicon for electrochemiluminescence studies, *Thin Solid Films* **517** (2009) 5779–5782.

IV A. J. Niskanen, T. Ylinen-Hinkka, M. Pusa, S. Kulmala, S. Franssila, Deposited dielectrics on metal thin films using silicon and glass substrates for hot electron electrochemiluminescence, *Thin Solid Films* **519** (2010) 430–433.

V A. J. Niskanen, T. Ylinen-Hinkka, S. Kulmala, S. Franssila, Integrated microelectrode hot electron electrochemiluminescent sensor for microfluidic applications, *Sensors and Actuators B, Chemical* **152** (2011) 56–62.

VI A. J. Niskanen, A. Varpula, M. Utriainen, G. Natarajan, D. C. Cameron, S. Novikov, V.-M. Airaksinen, J. Sinkkonen, S. Franssila, Atomic layer deposition of tin dioxide sensing film in microhotplate gas sensors, *Sensors and Actuators B, Chemical* **148** (2010) 227–232.

Author's contribution

Publication I

Development of the thermal oxidation process and processing of the oxidized silicon samples. Contribution to writing of the article.

Publication II

Development of the thermal oxidation process and processing of the oxidized silicon samples. Contribution to writing of the article.

Publication III

Development of the thermal oxidation, plasma deposition and liquid phase deposition processes. Planning of the sample series and processing of the samples. Writing of the article.

Publication IV

Development of the plasma deposition process. Planning of the sample series and processing of the samples. Writing of the article.

Publication V

Idea of on-chip integrated counter electrodes. Design of the devices, electrode geometries and sample containment schemes, planning and development of the fabrication processes, drawing of the photomasks and processing of the devices. Design and machining of the new sample holder for measurement of the devices. Photographic study of luminescence uniformity. Writing of the article.

Publication VI

Design of the devices, planning and development of the fabrication process, drawing of the photomasks, materials testing and processing of the devices. Writing of the article.

List of Abbreviations

Abbreviation	Meaning
AFM	Atomic force microscope/microscopy
ALD	Atomic layer deposition
APCVD	Atmospheric pressure chemical vapor deposition
BHF	Buffered HF (SiO_2-etch solution), also called BOE (Buffered oxide etch)
CMOS	Complementary metal–oxide–semiconductor, an integrated circuit fabrication technology
C-V	Capacitance-voltage measurement
CVD	Chemical vapor deposition
DI	De-ionized (water)
DNA	Deoxyribonucleic acid
DRIE	Deep reactive ion etching
ECL	Electrochemiluminescence
FN	Fowler-Nordheim tunneling
HECL	Hot electron-induced electrochemiluminescence
HF	Hydrofluoric acid
HMDS	Hexamethyldisilazane
ICP	Inductively coupled plasma, a form of reactive ion etching
IR	Infrared
ITO	Indium tin oxide, an optically transparent electrical conductor
I-V	Current-voltage measurement
KOH	Potassium hydroxide
LIF	Laser-induced fluorescence
LPCVD	Low pressure chemical vapor deposition
LPD	Liquid phase deposition
MEMS	Microelectromechanical systems
MHP	Microhotplate (also µHP)
MOS	Metal–oxide–semiconductor, a common three-layer structure in transistors and integrated circuits **-or-** Metal-oxide semiconductor, a semiconducting metal oxide material
MOSFET	Metal–oxide–semiconductor field-effect transistor
PCB	Printed circuit board
PDMS	Polydimethylsiloxane, a silicone polymer
PECVD	Plasma enhanced chemical vapor deposition
PTFE	Polytetrafluoroethylene, also known by the brand name Teflon®
PVD	Physical vapor deposition
QCM	Quartz crystal microbalance (also QMB)
RAE	Rotating analyzer ellipsometer

Abbreviation	Meaning
RCA clean	A standard wafer cleaning process, originally developed at the Radio Corporation of America (RCA)
RF	Radio frequency
RH	Relative humidity
RIE	Reactive ion etching/etcher
rpm	Revolutions per minute
RT	Room temperature
SC-1, SC-2	Standard clean 1 and 2, steps in RCA cleaning
sccm	Standard cubic centimeters per minute, a unit of flow rate
SEM	Scanning electron microscope/microscopy
SOG	Spin-on glass
SOI	Silicon on insulator
SU-8	A common type of negative epoxy photoresist
TDDB	Time-dependent dielectric breakdown measurement
TEM	Transmission electron microscope/microscopy
TMA	Trimethylaluminum, a common ALD precursor
TMAH	Tetramethylammonium hydroxide
UV	Ultraviolet
XRR	X-ray reflectivity
XTEM	Cross-sectional transmission electron microscopy

List of Symbols

Symbol	Meaning
A	An empirical parameter
A, B	Rate parameters of the Deal-Grove oxidation model
$A(t)$	Some function of time (defined elsewhere)
(aq)	Species in aqueous solution
d	Period in ellipsometric measurement
e^-_{aq}	Hydrated electron
f	Frequency (of analyzer rotation in an ellipsometer)
G, G_0	Conductance
G_{air}, G_{gas}	Conductance of a gas sensor in pure air and with analyte gas
(g)	Gaseous species
h	Some function of Fourier coefficients (defined elsewhere)
I	Current
I, I_0	Intensity (of a laser beam in an ellipsometer)
k	Rate coefficient of a chemical reaction **-or-** Optical extinction coefficient **-or-** Dielectric constant
l	Thickness of film
(l)	Liquid species
n	Refractive index
p-plane	Polarization plane parallel to the plane of incidence
p_{gas}	Partial pressure of analyte gas
Q_{BD}	Breakdown charge of dielectric
R	Resistance
R_{air}, R_{gas}	Resistance of a gas sensor in pure air and with analyte gas
R_s	Sheet resistance, also known as square resistance
r^p, r^s	Fresnel coefficients for reflection
S	Sensitivity of a gas sensor
s-plane	Polarization plane perpendicular to the plane of incidence
(s)	Solid species
t	Time
V	Voltage
x	Thickness of film
α, β	Fourier coefficients
β	Another empirical parameter
λ	Wavelength
ϕ	Incidence angle in ellipsometry
Δ	Phase difference measured in ellipsometry
Ψ	Amplitude ratio measured in ellipsometry
τ	Oxidation time corresponding to existing oxide thickness

List of Figures

List of Tables

1 Introduction

Chemical sensors have always been important in many fields of science. Not only chemistry and such chemistry-related fields as environmental analysis *e.g.* of pollution and contaminants, but also most industrial processes need routine on-line monitoring. Biological sciences and medicine are also chemical at heart, and all related diagnostics rely on chemical sensors. With the proliferation of potentially harmful chemicals not only in industry, but in everyday life as well, chemical sensing is often needed for ensuring personal safety. Sadly, the importance of the latter is nowadays not due only to unintentional chemical hazards.

Traditional methods of chemical analysis typically involve sample collection and preparation, separation, preconcentration and finally analysis. Analysis may include the measurement of a calibration curve, or the use of a standard addition method to extract the desired chemical information from the detector signal. All this is labor-intensive, requires supplies of reagents and clean laboratory glassware, and probably a trained lab technician. Especially in applications where analysis should be done far from the lab—environmental monitoring, disaster control, bedside medical diagnostics, personal safety *etc.*—the ideal would be a single, self-contained instrument that requires no addition of external reagents, and where all contaminated parts are either self-cleaning or disposable.

Especially in portable instrumentation, miniaturization of chemical analysis systems presents an obvious advantage. The use of standard microfabrication techniques, originally developed for the needs of microelectronic fabrication, allows miniaturization of fluidic systems to be taken to the extreme. Just like microelectronic circuits, *microfluidic* systems offer the advantage of massively parallel fabrication, which keeps the cost of an individual fluidic chip low. This is especially important when the chip is to be single-use and disposable. Microscale sensors also minimize the amount of sample needed for analysis, thus decreasing the consumption of other reagents, and also making medical diagnostics more comfortable for the patient.

In this thesis, thin film technologies and microfabrication methods are applied to two different kinds of chemical sensor. One is an electrochemiluminescent sensor using hot electron excitation to induce luminescence. This *hot electron-induced electrochemiluminescence* (HECL) method requires ultrathin dielectric films on its working electrodes to enable tunnel emission of hot electrons into the sample solution. The method is well suited for detection in bioassay applications and integration into microanalytical systems, and is also complementary to other detection methods on the traditional laboratory scale.

The other chemical sensor is a *microhotplate gas sensor*, a widely developed microcomponent for detection of various gases. The device uses tin dioxide as a gas-sensitive material for resistive readout of gas concentration. The material works at high temperature, which is maintained with minimal power consumption by the use of a microfabricated resistively heated hotplate structure. The present device is

fabricated using tungsten metallization and plasma-deposited intermetal dielectrics, as a quick-turnaround prototype process using available materials and techniques. The gas-sensitive tin dioxide film is deposited by *atomic layer deposition*. This thin film deposition method places certain demands on the entire fabrication process of the device, as well as enables many interesting possibilities.

Organization of this thesis

Fundamentals of microfabrication are briefly presented in Chapter 2 using the fabrication processes of HECL and gas sensor devices as examples. Included are the most common thin film deposition processes, ways in which films are patterned and characterized, and some other miscellaneous yet important processes including cleaning, bulk etching, molding and bonding.

Chapter 3 is all about ultrathin films, which are needed in the HECL device. The chapter begins with an in-depth look into ellipsometry, which is the most extensively used characterization technique in this work, followed by a discussion of environmental effects on those measurements. Also measurements of native oxidation of silicon and the adsorption of atmospheric contaminants over time are presented and discussed. A look at the author's work on deposition of ultrathin films by various methods follows. A reduced temperature, low oxygen concentration oxidation process was developed to produce oxide films of ∼4 nm thickness. Aluminum oxide was deposited by atomic layer deposition on silicon and various metal thin films, and the onset of deposition on each was investigated by ellipsometry. Finally, LPCVD and PECVD processes were used to produce ultrathin films of silicon nitride and silicon dioxide.

Chapter 4 contains a literature overview of hot electron-induced electrochemiluminescence and its use as an analysis technique. Details are then presented on the author's work with various materials to investigate their suitability for HECL application. That work has been prelude to the development of an integrated microelectrode HECL device suitable for quantitative analysis in the laboratory or in the field, or for use as a detector in integrated microfluidic systems. Devices were fabricated on silicon and glass substrates, and polydimethylsiloxane (PDMS) sample chambers and patterned hydrophobic films were investigated for sample containment. Unpublished data on hydrophilic modification of enclosed PDMS fluidic systems is also presented, as well as preliminary work aiming for the use of polymeric substrates in HECL devices.

Chapter 5 begins with a brief overview of semiconductor gas sensors. The author's development of a microhotplate gas sensor platform utilizing ALD-deposited SnO_2 as its sensing film is then presented, along with the peculiarities associated in processing the ALD deposited film, and the use of tungsten metallizations and PECVD SiO_2 intermetal dielectrics in the prototype fabrication sequence.

The main results of this work are summarized in Chapter 6, with some speculation on

what future developments should be pursued. Finally, Appendices A and B contain detailed fabrication process descriptions for all variations of the HECL devices and the gas sensor device.

2 Fundamentals of microfabrication

Nearly all surface microfabrication is based on deposition and patterning of thin films, one on top of another. When properly aligned together, they form the final structure, be it an integrated circuit, a digital image sensor, or a microfluidic system. Thin films are deposited over the entire substrate by various processes, after which they are patterned. The pattern is usually reproduced from a photomask into a film of photosensitive material in a photolithography process. This is then used to pattern the newly deposited thin film. All microfabricated devices are made by combinations of these basic processes.

Figure 2.1 shows three chemical sensors made by standard microfabrication techniques (Publications **V** and **VI**). These will be used as examples in this chapter. Their complete fabrication processes are presented in full detail in Appendices A and B. The hot electron electrochemiluminescence (HECL) chips are integrated microelectrode devices for the analytical use of hot electron-induced electrochemiluminescence, which have been fabricated as silicon and glass versions. The microhotplate device is a general-purpose platform for testing new gas sensor materials and technologies.

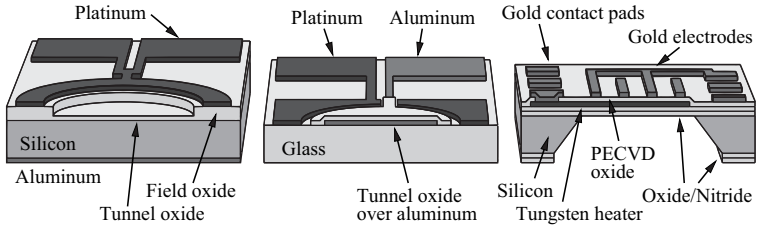

Figure 2.1: Three microfabricated chemical sensors: a silicon HECL chip (*left*), a glass HECL chip (*middle*) and a microhotplate gas sensor (*right*).

The devices are shown partly in cross-section to better demonstrate their structure. As is common in diagrams of microfabricated devices, all their dimensions are not shown correctly. Especially the vertical and lateral scales are not equal, as it would be impossible to accurately draw films of several nanometers thickness when the lateral dimensions of the chip are on the order of millimeters. It must also be noted that, while only single devices are shown in the various diagrams, the wafer contains tens, hundreds or thousands of devices all being subjected to the same processes simultaneously.

2.1 Substrate selection

Silicon is the most common substrate material for electronic applications, but it has long been recognized as a versatile mechanical material as well [1]. The combina-

tion of its excellent material properties with the already mature silicon processing technology developed for microelectronic applications made it an obvious starting point for micromechanical systems as well [2].

In many micromechanical applications, the anisotropic etching properties of crystalline silicon can be utilized. In this respect, the three common crystal orientations (100), (110) and (111)[†] differ greatly, as detailed in section 2.5.2. All are readily available in both *p*-type and *n*-type materials[‡] of various resistivities in the order of 100 Ω·cm to 0.001 Ω·cm, specialty wafers even beyond those limits. Despite their high cost, silicon-on-insulator (SOI) wafers, consisting of a thin, high-quality silicon layer isolated by an oxide layer from the handle wafer, offer many advantages in the fabrication of microelectromechanical systems (MEMS), microhotplates and optical devices [4, 5].

For non-electronic applications, a fully insulating substrate can often be of advantage, *e.g.* when high-voltage capillary electrophoresis [6] is integrated in the device. Transparency to visible light is also required *e.g.* in optical detection, and lower thermal conductivity can also be advantageous [7]. For this reason, glass wafers including quartz, borosilicate (Pyrex), soda-lime and others, are made in the same size and thickness as silicon wafers. Glass can be hermetically bonded to silicon by a process called *anodic bonding* [8], which is often utilized in the fabrication of microfluidic channels.

Plastic substrates may also be used in normal microfabrication processes, provided that process temperatures are low enough not to melt or warp the substrates. Polyimide, for example, is stable to ∼400°C or above [9, 10], which is high enough for many processes. Furthermore, plastics offer many interesting options for the fabrication of fluidic channels *e.g.* by hot embossing, injection molding *etc.* [11, 12] Adhesion of deposited materials may differ greatly on various substrates, but even PTFE can be modified by plasma treatment or graft copolymerization to improve metal adhesion [13, 14], and is commercially available in metallized form (copper-clad circuit boards). Similar methods can be used for metallization polyimide substrates [15, 16], which are commonly used as flexible PCBs, but we have found the adhesion of aluminum quite satisfactory without any pretreatment of the polyimide film.

Closely related to adhesion issues is the matter of contact angle of liquids on the substrate surface, which is dominated by the surface free energy of the material [17, 18]. Like adhesion properties, contact angle can also be modified by plasma treatment [19]. Especially in fluidic systems, the contact angle of water is critical, as it determines how easily fluidic channels can be filled. Oxygen plasma treatment is therefore extensively used for hydrophilic modification of naturally hydrophobic materials, and for enhancing bonding of PDMS, as detailed in Sections 2.5.4 and 4.6.

[†]The numbers denote the *Miller indices* [3, pp. 14–15] of the surface of the wafer.

[‡]Doped with boron or phosphorus, respectively, to create electronic holes or unbound electrons as positive or negative charge carriers.

HECL devices have in this work been fabricated on highly doped n-type silicon of (111) orientation. The dopant type and crystal orientation do not matter in this application, as silicon is used simply as a conductive substrate. The major advantage of silicon is the possibility of creating high-quality dielectric films by thermal oxidation. Borosilicate glass wafers have also been used in an alternative fabrication process. Work is ongoing to fabricate HECL devices on DuPont™ Kapton® polyimide, a material commonly used for flexible electronics, and new Teijin® Teonex® polyethylene-naphthalate [20] films as well.[†] The gas sensor devices use a (100) silicon substrate to enable micromachining of the microhotplate, but wafer doping is non-critical, as the active part of the device is electrically isolated from the substrate.

2.2 Thin film deposition

Thin films can be formed on a substrate surface by a variety of methods. Technically, *deposition* refers to methods where all atoms composing the film originate from outside the substrate. Any method where the substrate itself partakes in a chemical reaction to form the film is more accurately called film *growth* [21, pp. 298]. The most common example of film growth is thermal oxidation of silicon.

This is only a brief overview of various film growth and deposition methods. Ultrathin films will be treated in greater depth in Section 3.3.

2.2.1 Thermal oxidation of silicon

The best quality silicon dioxide films can be produced by thermal oxidation [3, pp. 68–94]. In this process, the surface of the silicon substrate itself is oxidized at high temperature (commonly up to 1100°C or even higher in some special applications) in an oxidizing atmosphere, either oxygen (*dry oxidation*):

$$\mathrm{Si\,(s)} + \mathrm{O_2\,(g)} \rightarrow \mathrm{SiO_2\,(s)}$$

or water vapor (*wet oxidation*):

$$\mathrm{Si\,(s)} + 2\,\mathrm{H_2O\,(g)} \rightarrow \mathrm{SiO_2\,(s)} + 2\,\mathrm{H_2\,(g)}$$

The oxide as well as its interface to the silicon substrate are of excellent quality, making it ideal as a MOSFET gate insulator. Wet oxidation is fast enough to be convenient for producing thicker isolation oxides (up to a micrometer or so). The practical thicknesses of thermal oxide films are limited, since the oxidation rate decreases with increasing film thickness. This is due to the reaction taking place at the $\mathrm{Si/SiO_2}$ interface, not at the surface of the substrate, requiring the oxidizing species to diffuse through the film in order to react with the silicon. The well known Deal-Grove model of silicon oxidation [3, pp. 68–75; 22] has two distinct regimes,

[†]DuPont™ and Kapton® are trademarks or registered trademarks of E. I. DuPont de Nemours and Company. Teijin® is a registered trademark of Teijin Limited. Teonex® is a registered trademark of Teijin DuPont Films Japan Limited.

in which the oxidation rate is limited either by reaction kinetics (thin films, below ∼100 nm):

$$x \approx \frac{B}{A}(t+\tau)$$

or by diffusion (thick films, above ∼100 nm):

$$x \approx \sqrt{B(t+\tau)}$$

where x is the oxide thickness, A and B are experimentally determined parameters that both follow the Arrhenius equation in temperature, t is the oxidation time and τ is a time offset that corresponds to the oxide thickness at the beginning of oxidation, *e.g.* a native oxide. Below ∼30 nm, however, the Deal-Grove model underestimates the oxide thickness, and extended versions of the model have since been published to account for the excess growth in the initial oxidation regime [23–26].

Despite the slow oxidation rate and relatively long loading, unloading and temperature ramping times, thermal oxidation is economical since it is a *batch process*, where hundreds of wafers can be processed simultaneously in a single process run. But due to its high process temperature, thermal oxidation can only be performed on wafers not containing metals or other materials that would melt, burn or diffuse, therefore oxidation is a *front-end* process only. Figure 2.2 shows the growth and patterning of oxides in the silicon HECL device. First the thicker (approx. 380 nm) field oxide or isolation oxide is grown by wet oxidation (a). It is subsequently patterned by photolithography and wet etching in BHF (b–d), as explained in Sections 2.3 and 2.4. Then the thinner (approx. 4 nm) tunneling oxide is grown in a second specially tailored dry oxidation step (e), as detailed in Section 3.3.1. Finally, the metallizations are made on the wafer (Figure 2.5, later). Conversely, the 4 nm ALD-deposited Al_2O_3 tunneling dielectric of the glass device can be made last on the wafer, as ALD is a relatively low-temperature process.

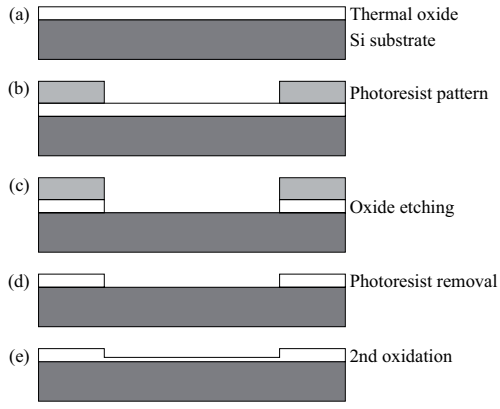

Figure 2.2: Growth and patterning of the 380 nm field oxide and 4 nm tunneling oxide in a silicon HECL device.

2.2.2 Chemical vapor deposition and atomic layer deposition

Chemical vapor deposition [3, pp. 326–350], CVD for short, uses a gas phase reaction to deposit material on the substrate surface, *e.g.*:

$$\mathrm{SiH_4\,(g) + 2\,N_2O\,(g) \rightarrow SiO_2\,(s) + 2\,H_2\,(g) + 2\,N_2\,(g)}$$

Ideally the reaction is surface activated, so nucleation does not occur in the gas phase, only on the surface. The most common deposited materials and their reactants are silicon dioxide ($\mathrm{SiH_4 + N_2O}$ or $\mathrm{SiH_2Cl_2 + O_2}$), silicon nitride ($\mathrm{SiH_4 + NH_3}$ or $\mathrm{SiH_2Cl_2 + NH_3}$) and amorphous or polycrystalline silicon ($\mathrm{SiH_4}$ or $\mathrm{SiH_2Cl_2}$ alone).

CVD can be either thermally activated (low pressure CVD, LPCVD or atmospheric pressure CVD, APCVD) or plasma activated (plasma enhanced CVD, PECVD). The former is done at high enough temperature (250–500°C for tungsten CVD, ∼400°C for low-temperature oxide, 650–800°C for silicon nitride [27, pp. 555]) to cause the gases to react, while the latter uses a plasma to activate the reactant species, enabling deposition at a considerably lower temperature (300°C or even below). Lower deposition temperatures lead to lower quality films, containing reaction byproducts (mainly hydrogen) and dangling bonds, and having non-stoichiometric film composition. All these factors lead to greatly increased etch rates and degraded electrical properties. [27, pp. 527–530]

In Publication **VI**, the gas sensor's microhotplate membrane is composed of silicon nitride deposited by LPCVD, over a thermal oxide film. The oxide and nitride films also serve as etch masks in the final silicon bulk etching step. The intermetal dielectric layer, on the other hand, is deposited by PECVD over the already metallized wafer. Both LPCVD and PECVD deposited films have been tested as tunneling dielectrics in HECL devices as well (Publications **III** and **IV**).

A special class of CVD is *atomic layer deposition*, ALD [28–30]. As in ordinary CVD, the deposition reaction occurs between two gaseous species at the substrate surface, but in ALD the two precursors are not introduced simultaneously into the reactor. Rather, they are introduced as pulses, one at a time, each followed by a purging pulse of inert gas. In a suitable temperature range, called the *ALD window*, a single monolayer of reactant is adsorbed on the substrate surface during each precursor pulse. The deposition reaction occurs between these adsorbed monolayers, and is therefore self-limiting—the precursor pulse lengths do not determine the deposition rate. The thickness of the deposited film can thus be controlled with monolayer precision by changing the number of deposition cycles.[†] For this reason it is an excellent method for producing ultrathin tunneling dielectrics. ALD-deposited aluminum oxide has been extensively used in HECL devices (Publications **III**, **IV** and **V**), and it can be deposited from TMA and water precursors at temperatures

[†]Ideally, each precursor pulse should deposit a single monolayer of atoms. In practice, effects such as the steric hindrance of attached chemical groups in the precursor molecules lead to less than a monolayer of deposited atoms per monolayer of adsorbed precursor molecules. The coverage of these sub-monolayers is, however, highly repeatable.

low enough to be compatible with glass and even plastic substrates [31]. A wide variety of materials can be deposited by ALD [30], and it is easy to make layered structures simply by alternating between different precursors. This versatility was a primary incentive for using ALD to deposit the tin dioxide sensing layer in the gas sensor device as well (Publication **VI**).

2.2.3 Physical vapor deposition

Unlike chemical vapor deposition, where a chemical reaction forms the deposited film, physical vapor deposition (PVD) relies purely on physical phenomena. The main PVD methods are *evaporation* and *sputtering* [3, pp. 295–321], and they are (especially the latter) the most common methods of metal film deposition. CVD and ALD processes do exist for *e.g.* tungsten deposition, but they are mainly used in special applications such as via filling [3, pp. 347–350] or X-ray Bragg mirrors [32].

In evaporation, metal is heated either on a resistively heated filament, or locally by an electron beam, until material begins to evaporate or sublimate. In the evaporator's high vacuum, the atoms travel along straight paths until they encounter chamber walls or the substrate surface, where they condense to form a thin film. Due to the line-of-sight nature of evaporation and the relatively small size of the evaporation source, it is especially useful when non-conformal films are desired over topography, *e.g.* for a lift-off process (see Section 2.4). To maintain true line-of-sight deposition, the mean free path of evaporated atoms must be greater than the source to substrate distance, typically some 20–30 cm. This requires high vacuum conditions of less than ∼0.1 mTorr (∼0.01 Pa) pressure. [33, pp. A 1.0:1]

In the sputtering process, an argon plasma is generated between the substrate and a *target* made of the desired material, at a pressure of ∼1–10 mTorr (∼0.1–1 Pa). Argon ions bombard the target surface, causing ejection of atoms or atom clusters, which condense on the substrate surface.[†] [33, pp. A 3.0:1] In *reactive sputtering*, a reactive gas such as nitrogen or oxygen is introduced into the process chamber, to produce nitride or oxide films of the sputtered metal. The plasma thus not only sputters the metal, but also activates the gaseous reactive species [27, pp. 547]. Since the sputtering target is rather large and close to the substrate, the spatial angle it occupies is large, and sputtering is therefore much more conformal than evaporation. If sputtered films are to be patterned by lift-off, some effort may be made to tailor the sidewall profile of the photoresist mask to help create discontinuities in the film, as detailed in Section 2.4.

All the metallizations in the HECL devices (platinum counter electrodes, as well as aluminum working electrodes in the glass devices) and gas sensors (tungsten heater resistors and gold sensing electrodes) were made by sputtering. To improve adhesion

[†]Actually, sputtering refers to the ejection of material by ion bombardment, and is therefore technically an *etching* process, where the sputter target is etched—condensation of the sputtered material elsewhere is merely a side-effect. Common use of the word, however, takes the substrate's point of view, and regards sputtering as a deposition process.

of gold and platinum to the substrate, adhesion-promoting layers of chromium or titanium, only about 10 nm thick, were used under these metals. This is common practice, and is conveniently done in a multi-target sputtering system without breaking the vacuum between depositions. In the gas sensor process, reactive sputtering was employed to create protective layers of tungsten nitride above and below the heater resistor tungsten metallizations. In one process variation, the SnO_2 sensing layer was also deposited by reactive sputtering instead of ALD.

2.2.4 Other methods

Liquid phase deposition (LPD) is a chemical process for depositing silicon dioxide out of liquid phase near room temperature. In an aqueous solution of hexafluorosilicic acid H_2SiF_6 saturated with silica, an equilibrium exists:

$$H_2SiF_6\,(aq) + 2\,H_2O\,(l) \leftrightarrows SiO_2\,(s) + 6\,HF\,(aq)$$

When HF is removed from solution by addition of a HF scavenger *e.g.* boric acid H_3BO_3 or aluminum, the equilibrium shifts to the right according to Le Châtelier's principle, and silicon dioxide is deposited on the immersed substrate [34–36]. This method was briefly tested for application as a HECL tunneling dielectric, but its performance was not satisfactory.

An alternative room-temperature process that has been extensively used to grow HECL tunneling dielectrics [37–39] is *anodization* of aluminum, an electrochemical method which allows the thickness of the alumina film to be controlled through the anodization voltage [40]. Silicon can be anodized by a similar process to reproducibly produce thin films in the range of approximately 1–10 nm in dilute solutions of NH_3 [41] or HCl [42].

One low-temperature process of growing high-quality silicon dioxide films is *plasma oxidation* or *plasma anodization*, which enables oxidation at low temperatures by ionizing the oxidizing species to enhance their reactivity, as well as using an electric field to accelerate them towards the substrate surface. Since the oxide is grown out of the silicon itself, rather than deposited from impure reactants, its quality is comparable to that of thermal oxide. The process temperature, however, is much lower, below 600°C [43, 44] or even room temperature [45].

Thick films *e.g.* for semiconductor gas sensors [46] or solar cell metallization [47] can be deposited as pastes followed by annealing to produce the solid film. If screen printing or drop deposition is used, a separate patterning step can be avoided. The pastes themselves are typically suspensions of nanoparticles produced by methods such as milling [48], sol-gel [49] or spray pyrolysis [50].

2.3 Photolithography

Direct writing of micrometer scale patterns on large-area substrates is extremely slow, therefore patterns are usually written only onto *photomasks*, also called *masks* for short. These photomasks are transparent plates of quartz or soda-lime glass with opaque patterns, typically of chromium metal. High-quality photomasks with micrometer resolution cost upwards of several hundred euros each,[†] but once a photomask has been made, the pattern can be quickly copied by optical methods onto substrates coated with a photoactive polymer material called *photoresist*, or *resist* for short. The process is called *photolithography*, or *lithography*. In essence, the method is as follows:

- Photoresist is dispensed onto the substrate in liquid form.
- The resist is spread evenly over the substrate by spinning at high speed, typically around 4 000 rpm for 30 seconds, creating a film of around 1 µm thickness.[‡]
- The resist is baked to remove the solvent from the film, typically at around 90°C for 20 minutes in an oven, or 1 minute on a hotplate, for normal positive resists.
- The photoresist film is exposed to UV light through the photomask (Figure 2.3, top). The exposed areas undergo a photochemical reaction, whereas areas under the dark patterns remain unchanged. Exposure time is typically a few seconds, depending on the light intensity.
- The exposed substrate is immersed in a developer solution, which dissolves the photoresist either from the exposed areas (*positive* resist, Figure 2.3, left) or unexposed areas (*negative* resist, Figure 2.3, right). Typical development times are on the order of a few minutes at most.

The above steps are common to all photolithographic processes, but depending on the photoresist chemistry and individual process requirements, additional steps may be required. Some negative resists *e.g.* SU-8 require another bake after exposure. It is common practice to begin by *priming* the wafer surface with an adhesion promoting material such as hexamethyldisilazane (HMDS), and to end with an additional higher-temperature bake in order to harden the photoresist by removing any remaining solvents and to enhance cross-linking of the polymer [3, pp. 191–194]. A chlorobenzene treatment can be applied before exposure or development to change the sidewall profile of the resist for lift-off purposes [3, pp. 283–285]. Alternatively, a *reversal bake* process [53, 54] can be used to develop positive resists in negative tone,

[†]For rapid prototyping and processes where linewidths and alignment tolerances are large, plastic film photomasks can be used instead. These are commonly used in PCB manufacturing, achieve linewidths down to a few tens of micrometers, and cost only a few euros each. The HECL devices have been processed exclusively with plastic photomasks.

[‡]Resists used for patterning other films are thin in order to maintain good resolution. Structural resists such as SU-8 [51, 52], on the other hand, may be hundreds of micrometers thick.

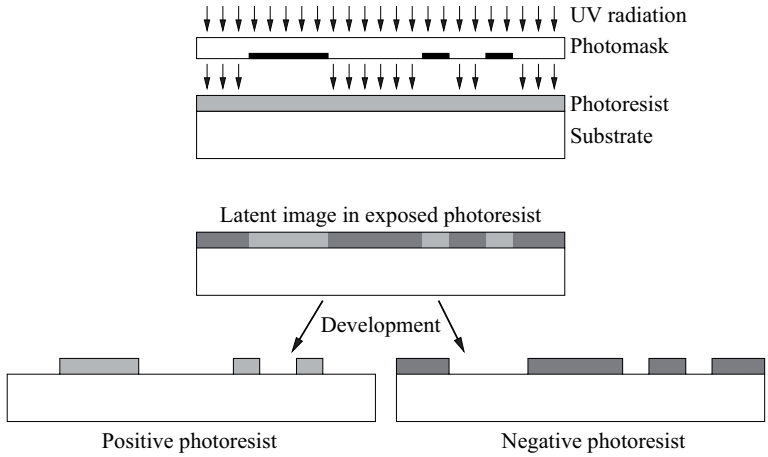

Figure 2.3: Photolithography using positive (*left*) and negative (*right*) photoresist.

which also creates a retrograde sidewall profile suitable for lift-off. Special lift-off resists such as the MicroChem LOR^{TM} [55] are also available to leave an overhang at the edge of a resist pattern. An especially in-depth treatment of many aspects of photolithography is presented in *Integrated Circuit Fabrication Technology* [56].

At this point the substrate contains a photoresist copy of the photomask's original pattern. This photoresist layer is very rarely left in the completed device, unless resists such as SU-8 are used, which are designed as photopatternable structural materials (*e.g.* the master molds for the HECL devices' PDMS lids are made of SU-8 on a silicon substrate). Instead, it is used as an intermediary to transfer the pattern to the underlying thin film, and is itself finally removed. Resist removal or *stripping* is effected by organic solvents and ultrasonic agitation, specialized caustic resist removal agents, oxygen plasma ashing, wet oxidizing solutions (*e.g. Piranha* cleaning, Section 2.5.1) or a combination of these.

2.4 Pattern transfer

As was stated previously, thin films are mostly deposited over the entire substrate. The pattern that is desired in a film is transferred by photolithography from a photomask into a photoresist layer. Next this layer is used to pattern the thin film itself.

If the thin film is grown or deposited first, and lithography is performed next, the

photoresist on top of the thin film can be used as an *etch mask*.[†] When the substrate is immersed in a suitable etchant solution, the exposed areas of the film are etched, while the areas protected by the photoresist patterns are not, as demonstrated in Figure 2.2 (page 29). This copies the photoresist pattern into the underlying film, maintaining the polarity of the image (*i.e.* film patterns remain where the photoresist pattern was).

This process of *wet etching* [3, pp. 259–264] is simple and a batch process, can exhibit excellent selectivity, but has some limitations. Firstly, wet etching is generally *isotropic*, *i.e.* etching proceeds sideways underneath the edges of the photoresist pattern at approximately the same rate as it proceeds downward. The resulting lines in the patterned film will thus be narrower than the original photoresist pattern. The thicker the film to be patterned, the more pronounced this effect is. Narrowing of the patterns can sometimes be compensated for in the photomask design, but the sidewall profiles of the produced pattern edges will always be sloped, which may or may not be an issue, depending on the application.

Secondly, the photoresist must be able to withstand the etchant for the duration of the etching process. Strongly oxidizing etch chemistries may damage the photoresist before the film is etched through, and especially positive photoresists cannot tolerate strongly alkaline etchants. Some wet etchants may cause adhesion problems either by attacking the photoresist/substrate interface at the pattern edges (as was seen during etching of the SnO_2 film in the gas sensor devices), or by diffusing through the photoresist (as unbuffered HF may do, which is why BHF is preferred for wet etching of SiO_2), causing delamination of the resist pattern in either case.

An alternative etching process, called *dry etching*, *plasma etching* or *reactive ion etching* (RIE) [3, pp. 266–283], addresses the issues of linewidth control and sidewall profile. RF power is used to create a plasma in a low-pressure atmosphere of suitable etchant gases. The combined effect of chemical etching by reactive species in the gas phase, and ion bombardment of the substrate surface in an electric field, results in strongly *anisotropic* etching, *i.e.* the etch rate downwards is much greater than sideways. All forms of dry etching cannot, however, be performed as batch processes, not all materials can be dry etched, and selectivities are often poor due to the physical effect of ion bombardment. The process may also impart much wear on the photoresist pattern, resulting in gradual erosion and ultimately failure of the etch mask.

A completely different approach to patterning a deposited film is *lift-off* [3, pp. 283–285]. In this process, lithography is used to create a photoresist pattern *first*, followed by deposition of the thin film *over* the patterned photoresist. When the

[†]A photoresist pattern, when used as an etch mask, is commonly called a photoresist mask, or *mask* for short. Likewise *e.g.* a patterned oxide film may be called an oxide mask, or simply a *mask*, when used as an etch mask during bulk etching of silicon. Referring to a photomask also as a *mask* leads to no end of confusion, especially when ordering plastic photomasks from PCB manufacturers. In their terminology, *mask* means the photoresist coating on a circuit board, whereas the photomask is called a *film*.

photoresist is removed, any deposited film over the photoresist layer is removed with it, and only the previously exposed areas of the substrate are left coated with the deposited film. This results in *reversal* of the image polarity: Film patterns remain where there was an opening in the photoresist pattern.

One major limitation in lift-off is the deposition process temperature. Photoresists begin to undergo various physical and chemical changes around 150°C, affecting linewidth, edge profiles, adhesion and ease of removal. Thus lift-off is typically used only with physical deposition methods (although some ALD processes are low enough in temperature to be compatible with photoresist). A second issue is film continuity at the photoresist pattern edges. A perfectly conformal film over the photoresist would prevent the photoresist from being removed. In practice, a reasonably thin film has enough imperfections that solvent can access and dissolve the underlying photoresist. However, unless the deposited film is discontinuous at the pattern edges, it may not be removed along with the photoresist. At the very least, jagged edges may be left where the film is torn apart by ultrasonic agitation, as seen in the SEM image in Figure 2.4. (When used in electrodes, these may concentrate electric fields, and could be disastrous in a HECL working electrode. In the counter electrode the edge quality has little effect.) To alleviate this problem, steps may be taken to tailor the sidewall profile of the photoresist pattern, as discussed in Section 2.3, to create an overhang structure that cannot be perfectly coated by the deposition process. Alternatively, sacrificial films may be employed as described below.

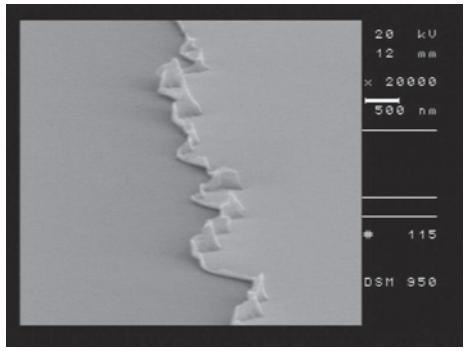

Figure 2.4: A SEM image of jagged edges in a sputtered platinum film patterned by lift-off. Standard positive photoresist was used without any overhang in the sidewalls.

Both etching and lift-off are used in the fabrication of the HECL devices. Lift-off is preferred when patterning platinum films due to the difficulty of etching them. Figure 2.5 shows both etching and lift-off, with and without a sacrificial aluminum film. Figure 2.5, left shows the silicon device from Figure 2.2 with its field and tunneling oxides already patterned (a), with a photoresist mask (b), a sputtered platinum film (c), and the platinum patterns left behind after lift-off (d). Arrows point to where the platinum film should ideally be discontinuous. Figure 2.5, right

shows an aluminized glass substrate with a photoresist pattern (a), which is used to pattern the aluminum film by etching (b). The film is intentionally overetched to leave the photoresist edge hanging over empty space, and the photoresist is not removed at this stage. When platinum is sputtered on this structure (c), discontinuities in the platinum film are created where indicated by arrows, facilitating easy lift-off with clean metal pattern edges (d). The same method could be implemented in the silicon device as well, followed by removal of all sacrificial aluminum from the wafer by etching with phosphoric acid. This would, however, add extra deposition and etching steps to the fabrication process. On the other hand, in the glass device, the same aluminum film serves a dual purpose, as it is further patterned by lithography and etching, to produce the working electrodes (e). The alumina tunneling dielectric is subsequently deposited by ALD and also patterned by lithography and wet etching (f).[†]

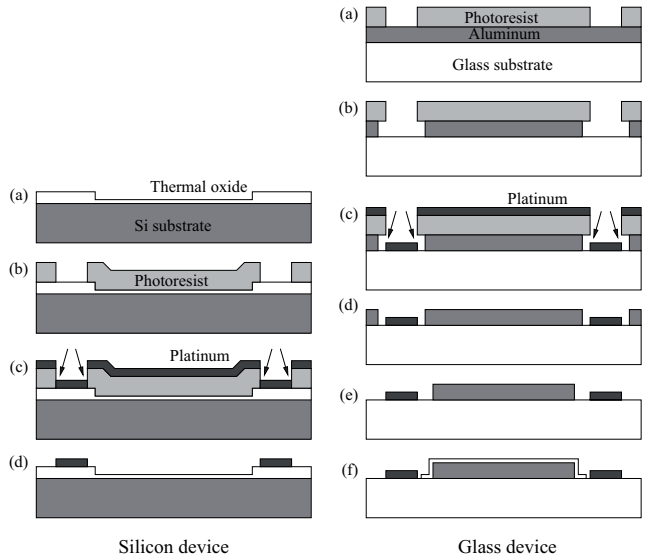

Figure 2.5: Film patterning by etching and lift-off in the fabrication processes of silicon (*left*) and glass (*right*) HECL components. Arrows indicate where discontinuities in the sputtered film are desired for the lift-off process.

Similar to lift-off, *shadow mask* technique also enables deposition directly in the desired locations on the substrate. A shadow mask, *e.g.* a thin sheet of steel, contains holes corresponding to the desired patterns. It is placed in close proximity of the substrate, and metal is then deposited by sputtering or evaporation. Metal is deposited on the substrate only where holes exist in the shadow mask, elsewhere the substrate is shielded by the mask. Resolution is worse than by lift-off, due to

[†]Since the Al_2O_3 film is only nanometers thick, the alkaline photoresist developer solution has a sufficient etch rate to be used as the etchant. Essentially, the photoresist is overdeveloped for a while, and then immediately removed, without a distinct etching step in between.

the greater thickness and separation of the shadow mask. If this is not an issue, however, the expensive and time-consuming photolithography step can be avoided entirely.

2.5 Other fabrication processes

2.5.1 Cleaning

Cleaning is a necessary step before any high-temperature process such as thermal oxidation or LPCVD, where diffusion of contaminants could degrade device performance. The cleaning step is usually performed immediately prior. A widely adopted cleaning process is the *RCA-clean* [57; 58, pp. 120], consisting of an SC-1 step (10 minutes in 5:1:1 $H_2O : NH_4OH : H_2O_2$ at 80°C)† to remove organic contaminants and to complex some metals, an SC-2 step (15 minutes in 5:1:1 $H_2O : HCl : H_2O_2$ at 80°C) to remove heavy metals, and a 10–30 second dip in ∼50:1 $H_2O : HF$ to remove the chemical oxide formed in the cleaning solutions, with a DI-water rinse after each step. It is also common practice to begin any fabrication process with an RCA or similar cleaning step to prepare the wafer surface into a known state, since storage of even a few months can deposit a significant amount of organic contamination on the wafer surface, as discussed in Section 3.2. However, once a wafer has passed initial oxidation and LPCVD steps and is metallized, such aggressive cleaning can no longer be used.

If a photoresist mask is used in extremely energetic processes such as ion implantation or some RIE processes, the edges of photoresist patterns may become carbonized and adhere strongly to the wafer surface. Highly oxidizing cleaning solutions such as *Piranha cleaning* (concentrated $H_2SO_4 + H_2O_2$ at 120°C) [58, pp. 121] can be used to burn away the organic residues in liquid phase. Like RCA, Piranha also cannot be used if *e.g.* aluminum metallization is to survive the process.

Wafer cleaning technology has evolved along with other fabrication technologies, tending towards more diluted cleaning solutions, use of additives in one cleaning solution to enable omission of another solution entirely [59, pp. 441], use of ozonated water and, increasingly, various dry cleaning (non-aqueous) chemistries [59, pp. 445–447; 60]. Especially MEMS devices with high aspect ratios and supported structures can be damaged by the high surface tension of water, and such methods as supercritical CO_2 cleaning [61] and HF vapor etching [62] may be preferred.

2.5.2 Bulk etching

Whereas microelectronic fabrication is mainly done on the silicon wafer surface, MEMS and a variety of other applications use silicon as a mechanical material.

†Chemicals used in the semiconductor industry have standardized concentrations, and are commonly specified by their volumes only. The concentrations are: NH_4OH: 28%, HCl: 37%, H_2O_2: 30%, HF: 50%, H_2SO_4: 95–97% and HNO_3: 69% by weight.

This creates a need to fabricate three-dimensional structures in the bulk of the wafer, *i.e.* to dig deeper than the surface.

Plasma etching processes have been developed to increase their etch rate and anisotropy. Two main variants of deep RIE (DRIE) are the *Bosch* process and *cryogenic* ICP RIE [63–65]. They are both usable for etching all the way through a wafer with very high aspect ratio and considerable selectivity towards certain masking materials.

A much simpler way of attaining striking etch profiles and atomic-scale smoothness is *alkaline etching* of crystalline silicon in aqueous solutions of either TMAH or KOH [66, 67]. They both have high selectivity towards silicon dioxide and silicon nitride, which can be used as masking materials, and they are also selective between the various crystal planes in crystalline silicon. In a prolonged etch process, the (111) crystal planes limit etching. In the common wafer orientations this means inverted pyramid shapes or v-profile grooves in (100) silicon, vertical-walled trenches with sloped ends in (110) silicon, and no vertical etching in (111) silicon. The latter will, however, etch laterally if trenches are first made by other methods *e.g.* plasma etching. Both KOH and TMAH etch rates are also dependent on the doping level of the silicon substrate: Heavily boron-doped silicon etches significantly slower than lightly doped material. [67]

KOH etching was utilized in the release of the microhotplate membrane of the gas sensor devices (although Bosch or cryogenic ICP RIE could also have been used, since thermal oxide works well as an etch-stop layer). For this purpose, the backside of the wafer was lithographically patterned, and holes were etched through the nitride and oxide. Figure 2.6, left shows the bulk etch process in cross-section. Since a (100) substrate is used, the sidewalls have a 54.7° angle to the plane of the wafer.

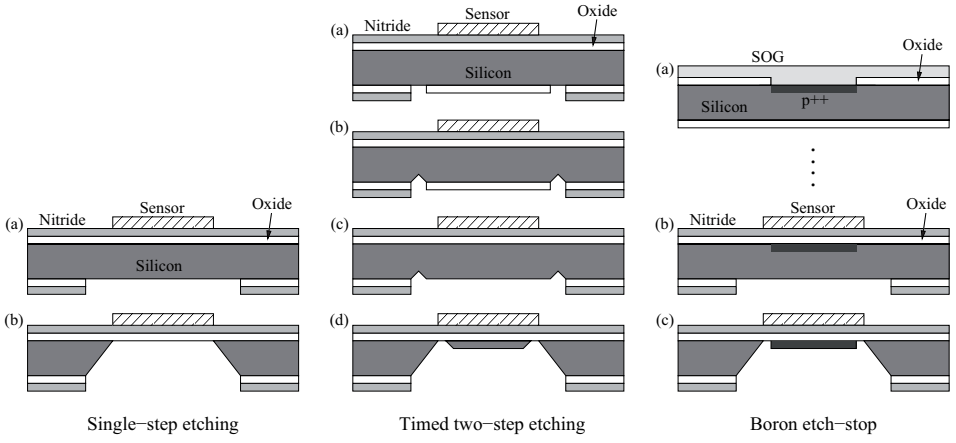

Figure 2.6: Three processes for releasing a microhotplate by alkaline etching: single-step etching (*left*), two-step timed etching (*middle*) and boron etch-stop (*right*).

Some MHP devices were also made with a silicon island in the middle of the membrane, as shown in Figure 2.6, middle. The method is similar to that presented by Briand *et al.* [68], albeit without optimization of the etchant composition. Initially, two lithographic and etching steps are used to produce the SiO_2 and Si_3N_4 mask (a), and a square ring is etched into the silicon (b). This step is nearly self-limiting (except for undercutting of the oxide square at its corners). The oxide square is removed with BHF (c), followed by a second bulk etching step (d). This step is highly critical, and etching must be stopped after the front surface oxide film is reached, but before the island is etched away.

This method was simple to implement, as the structure already contained both Si_3N_4 and SiO_2 films suitable for two-level masking, but a more controllable method utilizing *boron etch-stop* as shown in Figure 2.6, right would have been preferable. That would entail an extra oxidation step at the beginning of the fabrication process, patterning that oxide to form a doping mask, spin-coating a boron-containing spin-on-glass (SOG) and thermal drive-in of boron from the SOG into the silicon (a), and finally removal of the SOG and mask oxide by wet etching. From there, the fabrication process remains unchanged, but each device contains a highly boron-doped p^{++} area under the sensor (b). Finally, bulk etching is done in a single step through the entire wafer. The etchant is selective towards the highly p^{++} doped silicon, and that region remains after etching (c).

During alkaline etching of the wafer backside, the front surface of the wafer must be protected from the etchant, which can be accomplished with a suitable film *e.g.* PECVD-deposited silicon nitride. Lately, however, more convenient polymeric spin-on protective coatings have become available (ProTEK® by Brewer Science) [69,70], which can subsequently be removed simply by dissolution into acetone. Newest versions of these materials are also photopatternable [71]. Alternatively, the wafer may be clamped in a special sealed holder which exposes only one surface to the etchant.

2.5.3 Molding

Not all microfabricated components begin as a solid substrate. It is also possible to cast a polymer mixture onto a mold (fabricated *e.g.* on a silicon wafer) and release the cured polymer to form a three-dimensional structure containing *e.g.* fluidic microchannels. There is no intrinsic limit to the minimum feature size that can be replicated with this method, as long as the master mold can be made to the required specifications, and release of the replica can be effected without damage. In this work, capillary-filling chambers for the HECL devices were fabricated in polydimethylsiloxane (PDMS) elastomer by this method.

The master was made of SU-8 photopatternable epoxy by standard lithographic techniques on a silicon substrate. In principle, any substrate could be used, but SU-8 has good adhesion to silicon, and the wafer surface is certainly smooth enough to create a good, planar surface on the PDMS, suitable for bonding (Section 2.5.4).

Negative resists like SU-8 naturally have a retrograde sidewall profile, which is not desirable for releasing a cast replica, but the elasticity of PDMS makes release possible nevertheless. To ease peeling of the replica, a layer of anti-sticking fluoropolymer, with surface properties similar to Teflon®[†], was deposited from a CHF_3 plasma onto the master mold.[‡]

PDMS is supplied as a viscous liquid prepolymer base and a separate curing agent, which are mixed together to initiate polymerization. The reaction takes several hours, so there is plenty of time to mix the two thoroughly, pour the mixture over the mold, and outgas the mixture in vacuum. Outgassing is required to remove dissolved gases and bubbles formed during mixing, in order to ensure accurate reproduction of the mold's features, and to make the PDMS chip optically transparent. Approximately 30 minutes in a vacuum desiccator is sufficient to remove bubbles from a thin layer of liquid PDMS, after which it is cured at 50°C for two hours. The resulting PDMS slab can be peeled from the mold by hand, and manually cut into individual chips for bonding to the HECL devices.

2.5.4 Bonding

Especially when flow channels, fluid chambers and other cavities are needed in microfabricated devices, it is common to craft trenches in one substrate and bond it to another, thus creating the enclosed structure. In this work, capillary-filling fluidic chambers for the HECL chips were molded in PDMS and bonded to the silicon electrode chips.

The surface of PDMS has a great affinity to bond with other surfaces by van der Waals forces, and the material is elastic enough to accommodate substantial imperfections in either surface, and yet create a good seal. In some applications it is advantageous to be able to de-bond the PDMS from the other chip, and even re-bond them multiple times. In other cases a permanent bond is desired, especially since liquids can work their way into a non-permanent interface and cause unwanted de-bonding at inopportune times. A permanent bond can be created by treating the PDMS surface with oxygen plasma, and immediately bonding it with the silicon substrate. The plasma treatment is believed to form silanol groups on the PDMS surface. Within hours of being placed in contact, these react with corresponding groups on the other substrate, *e.g.* oxide or glass, forming permanent chemical bonds [72]:

[†]Teflon® is a registered trademark of E. I. DuPont de Nemours and Company.

[‡]The deposition was performed in a RIE reactor, commonly used for etching. By suitable selection of process gases, the RIE can be used for deposition as well. RIE and PECVD reactors in general tend to be very similar, differing mainly in process temperature and choice of gases.

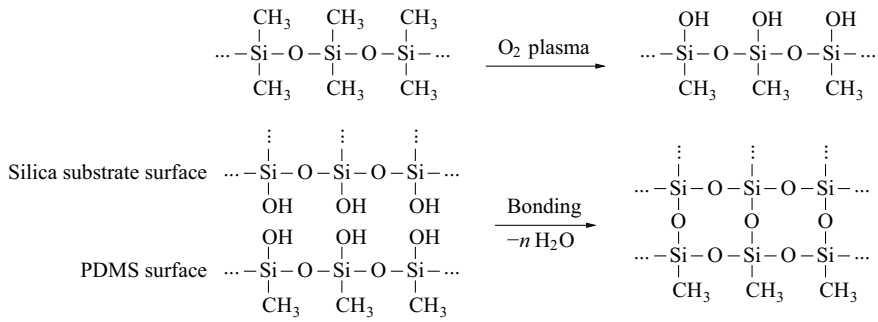

The bond is strong enough that the PDMS will often tear apart in its bulk rather than peel off at the interface [72–74]. This treatment also makes the PDMS surface hydrophilic, which is advantageous in microfluidic systems. That modification is, however, not permanent, and the surface will revert to its naturally hydrophobic state within hours or days, presumably due to diffusion of low-molecular weight oligomers from the bulk to the surface [75, 76]. The stability of the hydrophilic surface is affected by plasma or UV treatment [77], aging of the PDMS [76] and the nature of the storage medium [78, 79].

Glass can also be bonded to silicon, by *anodic bonding*. When pressure and a high voltage are applied across a glass/silicon stack at a temperature of 300–500°C, sodium ions in the glass diffuse away from the glass/silicon interface, creating a large electric field across the interface and forming a permanent chemical bond. This method, however, is highly unforgiving of any particle contamination on the surfaces to be bonded, and voids will be created surrounding any imperfections. [8]

There also exist a multitude of *adhesive bonding* methods [80], ranging from simple glue-type methods using *e.g.* PDMS as the adhesive [81] to UV photoinitiated adhesive bonding [82].

2.5.5 Dicing

Most fabrication processes are done on the wafer scale, which keeps the processing cost per individual device (of which there may be thousands on a wafer) low. At the very end of the process the wafers must finally be cut into individual chips, which are then packaged according to application. The wafers are first mounted from their backside onto an adhesive tape, after which the wafer is cut with a dicing saw, using diamond-impregnated blades of 20–250 µm thickness, depending on the substrate material. The blade cuts through the substrate and partly into the tape surface, leaving the chips separated from each other, but still attached to the tape, from which they can be plucked mechanically one by one. [83]

Since lots of dust is created during the cutting process, the surfaces of sensitive devices must first be protected with *e.g.* photoresist. A jet of water is used to cool the blade during cutting, and also to remove the dust that is formed, but this jet

may also damage sensitive membrane devices. To protect the gas sensor's membrane, the relatively thick etch-protective ProTEK® layer was left in place during cutting. Whatever material is used for protection, it must generally be removed afterwards, which must now be done for each chip individually, increasing the process time and tedium.

The coolant water, and dust along with it, may also enter any fluidic channels in the devices being diced. Removal of these contaminants from the enclosed channels may be difficult or impossible. The PDMS fluidic HECL devices, therefore, were first diced and then bonded at the chip level.

2.6 Thin film characterization

In many applications, the thickness of thin films is critical for the proper function of the completed device. Measurement of film thickness and properties is therefore important during process development, and monitoring of existing processes is necessary to indicate any random deviations or process anomalies.

2.6.1 Physical methods

In a sense, the most direct methods of film thickness measurement are *stylus profilometry* and *atomic force microscopy* (AFM). They represent the small group of methods which measure physical thickness only, without being affected by material properties of the film.

In stylus profilometry [21, pp. 160], a step is patterned in the film, and its height is measured by monitoring the vertical deflection of a sharp stylus scanned over that step. In addition to film thickness, lateral dimensions can also be measured, *e.g.* to determine the final linewidth of a metal pattern made by isotropic wet etching.

To accurately measure the thickness of a film by profilometry, a well defined step must be patterned in the film. In many cases this is easy to do, and is in fact done several times as part of the normal fabrication process, making profilometry a convenient and rapid analysis method. The film thicknesses of the heater resistors and sensing electrodes of the gas sensor, for example, are easily measured by profilometry after patterning. But especially in the case of ultrathin films, the patterning process may pose several challenges. Extreme cleanliness is, of course, required in the process, as well as ultimate selectivity between film and substrate in the etch process, and finally complete removal of the mask material. Any contamination, overetching or mask residues may easily produce errors greater than the film thickness itself. Even disregarding these potential problems, nearly atomic smoothness of the substrate is required to distinguish the step from background noise. While high-quality silicon wafers do offer the required surface smoothness, deposited films *e.g.* sputtered metals rarely do [84]. Finally, when the film to be measured is only a few atomic layers thick, the formation of a native oxide on the surrounding substrate

immediately after etching may cause a significant error in step height measurement. Some materials *e.g.* aluminum oxidize immediately in contact with air, and trying to avoid formation of a native oxide would be impractical if not impossible.

AFM is in principle the same as stylus profilometry, but it is extremely sensitive, and commonly scanned in two dimensions, thus used more as a surface imaging method than a thickness measurement method [21, pp. 176–181; 85, pp. 713–715]. It was used *e.g.* for the detection and measurement of film grains in the gas sensitive film in Publication **VI**, and the investigation of film nucleation in the early stages of ALD on a HECL device in Publication **IV**.

2.6.2 Optical methods

Ellipsometry is an optical method for determining the thickness and refractive index of transparent films. Being a rapid non-contact method, it is especially suited for routine monitoring, and it is also readily adapted to exotic research applications such as *in situ* monitoring inside a reactor. It is well suited for the measurement of films in the typical sub-micrometer thickness range, and also sensitive enough for measuring ultimately thin films of only a few nanometers thickness with sub-nanometer resolution. Thus ellipsometry has been used extensively throughout this work, and is discussed in greater detail in Section 3.1.

Another common optical method is *reflectometry*. It is based on measurement of the spectrum of light reflected off the substrate [27, pp. 300; 85, pp. 603–609]. Interference within the film causes certain wavelengths to be enhanced and others to be quenched. The reflected intensity of a single wavelength varies periodically with film thickness, and by fitting the intensities of multiple wavelengths to a mathematical model of the film, a unique solution can be found. Reflectometry can be performed via a microscope, thus requiring only a very small surface area for measurement. However, only films thick enough to show interference colors can be measured, upwards from ∼25 nm or so. With practice, quite reliable reflectometric thickness measurements can even be performed with the naked eye. Tables of film color under fluorescent lighting *vs.* thickness have been compiled for the most common films *e.g.* silicon dioxide and nitride [3, pp. 78; 85, pp. 608–609; 86, pp. 8.15–8.19].

2.6.3 Electrical methods

The resistivity of a thin conductive film, which often differs from the material's bulk resistivity, is typically measured measured using four-wire resistance measurement, also known as *Kelvin* resistance measurement [85, pp. 3].† This method eliminates the parasitic resistance of wires and connectors, as well as the contact resistance between the probe and film. From the resistance value, material resistivity can be calculated when the film thickness and the test structure's dimensions are known.

†Not to be confused with *Kelvin probe*, a method for measuring the work function or surface potential of materials.

Several standard test structures exist for this measurement [85, pp. 16–17, 620–622]. Double connections to the temperature sensing resistors in the gas sensor devices were made to enable this type of measurement.

The *sheet resistance* of a film can also be measured from an unpatterned film using a *four-point probe* [85, pp. 2–21]. Four equally spaced probe needles are pressed against the wafer surface, and voltage between the inner pair is measured as current is fed between the outer pair. The sheet resistance of an infinitely thin film on an infinitely large substrate is calculated as

$$R_s = \frac{\pi}{\ln 2}\left(\frac{V}{I}\right) \approx 4.53\,R$$

and the formula works reasonably well also for smaller insulating substrates with conductive films, if measured well away from the substrate's edge. The film's resistivity is obtained by multiplying R_s with the known film thickness.

Electrical properties of semiconductor and dielectric films can be probed by current-voltage (I-V) and capacitance-voltage (C-V) methods [27, pp. 301–312; 85, pp. 62–86]. By patterning metal or polysilicon electrodes on top of the dielectric, capacitor structures are formed, which can be used to determine the dielectric constant of a film of known thickness. Dielectric leakage current and breakdown voltage can also be measured with these structures. Figure 2.7 shows examples of leakage and breakdown measurements and statistical measurements of breakdown in LPD oxides by the author [36].

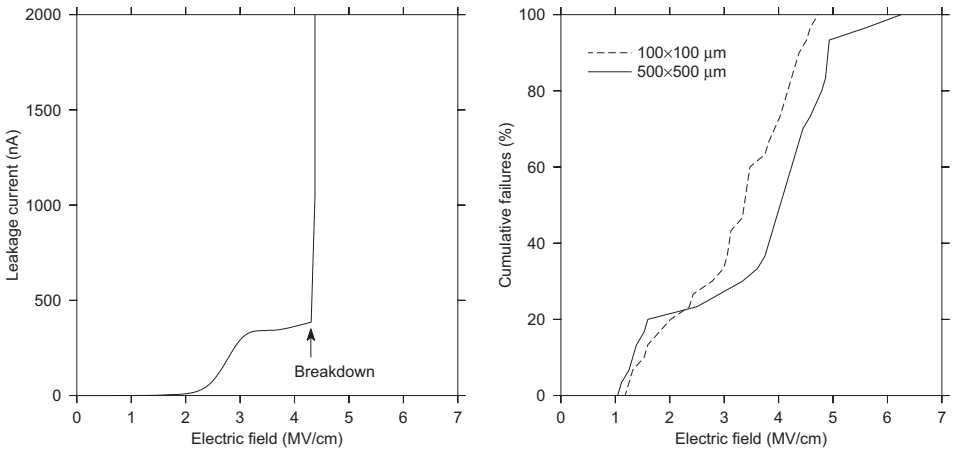

Figure 2.7: Leakage current in a 500×500 µm capacitor (*left*) and statistical breakdown voltage measurements of 100×100 µm and 500×500 µm capacitors (*right*) with a 72 nm thick oxide deposited by LPD. [36]

While breakdown voltage is a good metric of oxide quality, an alternative, closely related measurement is *time-dependent dielectric breakdown*, TDDB. The dielectric

is placed under a voltage stress below the breakdown voltage, causing current to be injected through the dielectric via various tunneling processes. Over time, the dielectric is damaged by this tunneling current, and breakdown finally occurs. The voltage can also be controlled to inject a constant current through the dielectric. When this current is measured and integrated over time from start to breakdown, a charge-to-breakdown value Q_{BD} is obtained. By repeating the measurement for multiple capacitor structures, statistical data of Q_{BD} can be accumulated, providing information not only on the intrinsic properties of the dielectric, but the distribution of extrinsic defects as well. [3, pp. 79–80; 85, pp. 394–401; 87]

2.6.4 Other methods

Film thickness is often monitored *in situ* during deposition *e.g.* in evaporators. A common method is to observe the change in resonance frequency of a *quartz crystal microbalance* (QCM) as mass accumulates on its surface during deposition [88]. A QCM can be used to monitor liquid phase deposition [88, 89] as well as deposition in a vacuum. QCMs have also been much used in biosensors, using either DNA hybridization or antibodies to detect the antigen by the associated mass increase as it binds onto the QCM's surface [88, 90, 91].

Thicker films are easily measured with reasonable precision by electron microscopy. This is especially useful if the sample is not suited for optical methods or stylus profilometry, *e.g.* in the case of a suspended membrane. Lateral dimensions of etched structures are measured as easily as film thicknesses from cross-sectional samples. *Scanning electron microscopy* (SEM) is the method of choice due to minimal sample preparation [21, pp. 58–63; 85, pp. 651–659], however the resolution of the instrument will limit thickness measurements to a minimum of tens or hundreds of nanometers. To measure ultrathin films or to observe the substrate/film interface with atomic resolution, *transmission electron microscopy* (TEM) or *cross-sectional* TEM (XTEM) is commonly used [21, pp. 46–59; 85, pp. 672–677]. The main shortcoming of TEM, however, is the extensive and tedious sample preparation required to make a suitably thin slice for TEM imaging.

X-ray reflectivity (XRR) is an analysis tool that provides thickness, density and roughness information of thin films and multi-film structures [92, 93]. A sample is illuminated by monochromatic X-rays at a narrow incidence angle, which is changed and the reflectivity of the sample is recorded at multiple angles. The obtained data is then analyzed by a variety of mathematical models. XRR is widely used especially in ALD research [29, 94–96].

3 Ultrathin films

While anything up to hundreds of micrometers thickness may be referred to as "thin films", the term gets an entirely new meaning when closing in on the lower physical limits of film thickness. When the film thickness approaches atomic dimensions, a new set of problems must be considered in both fabrication and characterization, since a single adsorbed monolayer of atmospheric contamination may constitute a significant fraction of the total film thickness. This influences the fabrication and use of such ultrathin films, and poses unusual requirements for metrology. For the HECL application (Section 4), approximately 4 nm dielectric film thicknesses are needed. That is only about 40 atomic layers, which is precisely in this ultrathin regime.

3.1 Ellipsometry and the measurement of ultrathin films

Ellipsometry is a very old method, born in the late 1800's following an observation of anomalous polarization of light reflecting off a surface close to the Brewster angle. In some cases, instead of being completely linearly polarized, the reflected beam showed a significant degree of ellipticity in its polarization, *i.e.* a superposition of two perpendicularly polarized components with a non-zero phase angle between them. The reason for this behavior was attributed by Drude [97, 98] and Rayleigh [99] to the presence of thin films on the reflective surfaces. Drude subsequently developed a relation between the material properties of the substrate and film, and the observed parameters in an ellipsometric measurement: the azimuth Ψ (the total reflection coefficients are different for light polarized in the p and s planes, see Figure 3.3; $\tan\Psi$ is the ratio between those coefficients) and phase difference Δ (the change in the phase angle between p and s components upon reflection). In its full form, this relation is the complex equation

$$\tan\Psi\, e^{i\Delta} = \frac{(r_f^p + r_m^p e^{-ix})(1 + r_f^s r_m^s e^{-ix})}{(1 + r_f^p r_m^p e^{-ix})(r_f^s + r_m^s e^{-ix})}$$

where r^p and r^s are the various Fresnel coefficients for reflection at the film (subscript f) and substrate (subscript m, for "metal") surfaces, and $x = 4n\pi\cos\phi\frac{l}{\lambda}$ where l and n are the film's thickness and refractive index, ϕ is the angle of incidence, and λ the wavelength. For extremely thin films, where $l \ll \lambda$, the simplified equations

$$\Delta - \Delta' = -A\left(1 - \frac{1}{n^2}\right)\frac{l}{\lambda} \tag{3.1}$$

and

$$2\Psi - 2\Psi' = B\,(1 - C)\left(1 - \frac{1}{n^2}\right)\frac{l}{\lambda} \tag{3.2}$$

are obtained, where A and B depend on the substrate's properties and the angle of incidence, and $C = n^2\cos\phi$. Δ' and Ψ' are the values of Δ and Ψ measured

with the same substrate but without the film. Equations 3.1 and 3.2 became known as the Drude equations, which, although valid for very thin films only, were the only practical way to approach the ellipsometry problem at the time. Following the development of digital computers, solving the exact Drude equation by numerical methods became practical, and ellipsometry became applicable to thicker films as well. [100]

The measured parameters Ψ and Δ are angles which vary periodically with film thickness in the range $\Psi = 0 \ldots 90°$ and $\Delta = 0 \ldots 360°$. The film thickness calculated from measured values of Ψ,Δ is therefore not unique, as the same Ψ,Δ values are repeated after every period d:

$$d = \frac{\lambda}{2\sqrt{n^2 - \sin^2\phi}} \tag{3.3}$$

This period is on the order of hundreds of nanometers, *e.g.* for silicon dioxide it is 281.5 nm when a helium-neon laser ($\lambda = 632.8$ nm) is used at the typical incidence angle $\phi = 70°$. Therefore in most cases the correct period can be assumed based on the film deposition process. If a unique thickness is required for a completely unknown film, the measurement can be performed at multiple wavelengths or incidence angles. [102]

The periodicity of the ellipsometric parameters can best be illustrated by calculating the values of Ψ,Δ that would result from a film of a given refractive index and varying thickness. These Ψ,Δ pairs can then be plotted as points in Ψ-Δ space. For a fully transparent film with an extinction coefficient k of zero, the *trajectory* formed by these data points closes in on itself to form a loop (or wraps around beyond the edge of the graph from $\Delta = 360°$ to $\Delta = 0°$) and repeats every period d (equation 3.3). Such a trajectory for silicon dioxide ($n = 1.465$) is presented in Figure 3.1, left.[†] Since Δ changes noticeably between thicknesses 1 and 10 nm, it is possible to measure extremely thin films by this method. The refractive index of such thin films, however, cannot be determined, as will soon become apparent.

For an absorbing film with $k > 0$, the Ψ-Δ trajectory spirals towards and settles at a single point. The greater the value of k, the sooner that point is reached. At that point, the deposited film has reached sufficient thickness that the ellipsometer's incident beam penetrates only the top layers of the film, and never reaches the substrate interface. Thus a further increase in film thickness has no effect on the measurement, and we are in essence measuring the surface of a bulk material. Examples of Ψ-Δ trajectories of absorbing films are presented in Figure 3.1, right.

One important limitation of ellipsometry is especially well demonstrated by plots of Ψ-Δ trajectories. Since two parameters are measured, it should be possible to solve for two unknowns (film thickness and refractive index). Figure 3.2 shows trajectories for hypothetical non-absorbing films of various refractive indices from $n = 1.1$ to 2.4. For the most part, any Ψ,Δ point can be correlated with a modeled trajectory (thus

[†]The trajectories in Figures 3.1 and 3.2 have been calculated using the `ONEFILM` Fortran program presented in *A User's Guide to Ellipsometry* [102, pp. 236–240].

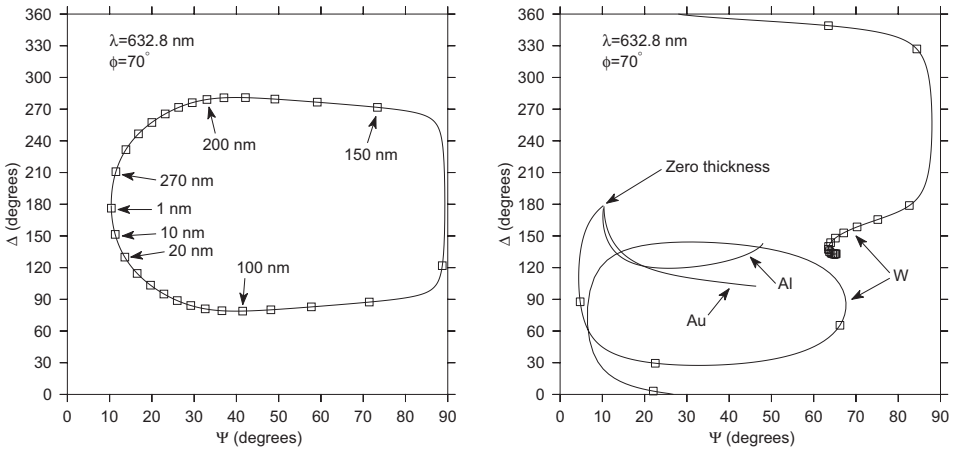

Figure 3.1: *Left:* The calculated Ψ-Δ trajectory of silicon dioxide ($n = 1.465$) on a silicon substrate. The trajectory repeats with a period of 281.5 nm. *Right:* The calculated Ψ-Δ trajectories of aluminum, gold and tungsten on a silicon substrate. The trajectories reach their endpoints at approximately 20, 40 and 70 nm film thicknesses, respectively. The latter has been marked at 5 nm intervals along the trajectory.

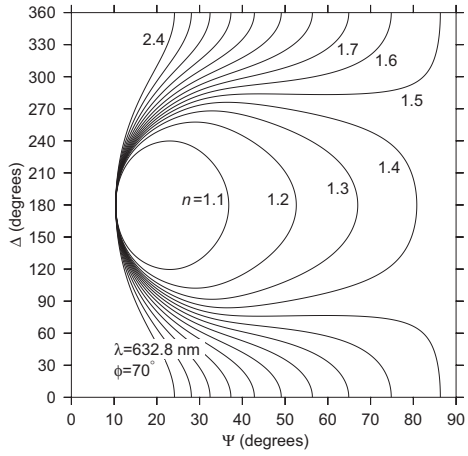

Figure 3.2: The calculated Ψ-Δ trajectories for hypothetical films of various refractive indices $n = 1.1 \ldots 2.4$ on a silicon substrate. Their periods range from 553.3 nm (for $n = 1.1$) to 143.3 nm ($n = 2.4$).

determining its refractive index) and a specific thickness value along that trajectory. Close to zero thickness, however, the various trajectories converge and cannot be differentiated from each other. Thus the refractive index of such ultimately thin films cannot be determined by ellipsometry.†

Some value of refractive index must, however, be assumed in order to calculate the film thickness. In this work, the bulk value of the material has been used, although it may differ for a deposited film, especially an ultrathin one. Furthermore, when ultimately thin films are considered, the film will seldom be uniform material throughout. Consider, for example, a silicon nitride film deposited by LPCVD. Despite all measures taken to ensure an oxide-free surface prior to deposition, some small thickness of oxide will certainly form during loading into the LPCVD furnace, and the film is in truth a bilayer of silicon dioxide and silicon nitride as the samples are unloaded. Immediately after unloading, atmospheric gases and contamination begin to adsorb on the wafer surface, creating a third layer (see section 3.2).

A further form of non-uniformity in films at their lower thickness limit is discontinuity, *i.e.* island-type growth instead of immediate full coverage of the substrate. Such growth can occur when the substrate surface is not especially reactive towards the reactant gases of the deposition process, and growth initially begins only at defect sites or other randomly distributed nucleation centers. When these islands are smaller than the wavelength of the probing light, an ellipsometer sees the discontinuous film as a uniform one with an effective refractive index somewhere between that of the film and that of the ambient air. Surface microroughness of the substrate or film are seen the same way. [102, pp. 246–251] If a bulk refractive index is used for a discontinuous film, a thickness value is obtained that is less than the thickness of the islands, but more than the thickness elsewhere on the substrate (*i.e.* zero, if the substrate is initially bare). Thus, at the onset of deposition, the deposition *rate* may appear lower than nominal, if island-like nucleation occurs. The observed deposition rate will subsequently increase until full coverage is achieved and then stabilize at that value.

With modern instruments, ellipsometric measurement of a film is simply a matter of placing the sample on the sample stage, adjusting its orientation with the help of an autocollimator, and hitting a key on a computer. Given a reasonable initial guess of film thickness, the computer instantly provides a result with an impressive number of decimal places in both thickness and refractive index. The true accuracy of these values depends on how accurately Ψ and Δ can be measured, and how accurately all other parameters in the measurement can be set. Especially the incidence angle ϕ is critical, and misalignment of only 0.05° can produce a 10% error in the thickness of a 10 nm film [21, pp. 266]. The measurement of Ψ and Δ is, however, precise enough in a modern instrument to reliably detect sub-monolayer changes in a film.

†The same convergence of trajectories repeats each period d. Therefore, in the full range of film thicknesses, there exist periodic windows where the refractive index cannot be accurately determined and, likewise, the film thickness can only be determined if a refractive index is first arbitrarily chosen. Except for the window near zero film thickness, these cases can be resolved by changing the ellipsometer's incidence angle or by using another wavelength.

The actual measurement of Ψ and Δ can be done in various ways. One common method is a rotating analyzer ellipsometer (RAE) instrument depicted in Figure 3.3. A light source, typically a laser, is followed by a stationary linear polarizer, usually set at a 45° azimuth. Next a quarter wave plate (compensator) that can be switched in or out of the beam path is used to make the light circularly polarized. After reflection from the sample, the beam passes through an analyzer rotating at constant angular speed, and finally enters a photodetector. The detected intensity I is a function of time:

$$I(t) = I_0 \left[1 + \alpha \cos 2A(t) + \beta \sin 2A(t) \right]$$

where

$$A(t) = 2\pi f t + A_c$$

where f is the known rotation frequency of the analyzer and A_c is a constant phase offset (*i.e.* the angular position of the analyzer at the start of the measurement) which is not used. The coefficients α and β are obtained by Fourier analysis of the digitized intensity signal. [85, pp. 587–594; 102]

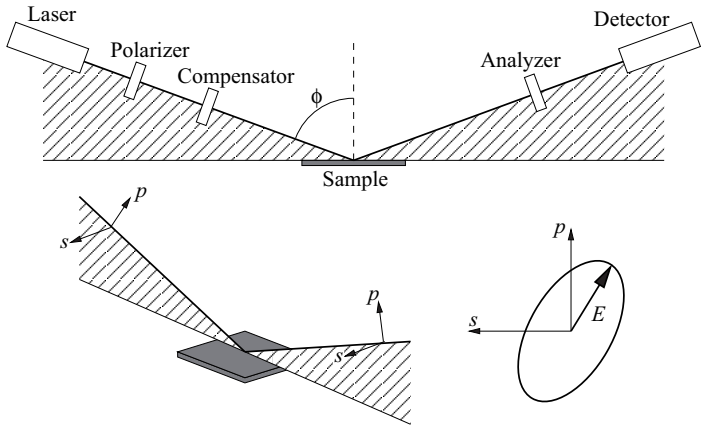

Figure 3.3: Schematic illustration of a RAE ellipsometer. The p and s components of the elliptically polarized beam of light are parallel and perpendicular to the plane of incidence (hatched), respectively.

The ellipsometer used in this work is a Philips SD 2300 of the rotating analyzer type, with a helium-neon laser with a wavelength $\lambda = 632.8$ nm as the light source. The incidence angle to the sample is $\phi = 70°$. The ellipsometric parameters are calculated [86] from the obtained Fourier coefficients with the compensator both in and out of the beam path, as indicated by subscripts:

$$\Psi = \frac{1}{2} \arccos \alpha_{\text{out}}$$

$$\Delta = \arccos \frac{h_{\text{out}}}{\sqrt{h_{\text{in}}^2 + h_{\text{out}}^2}}$$

where

$$h = \frac{\beta}{\sqrt{1-\alpha^2}}$$

3.2 Effect of environmental factors on ellipsometry

Adsorption of atmospheric gases is easily demonstrated by ellipsometry. When a substrate with a suitable thin film is repeatedly measured with an ellipsometer, an idea of the repeatability of the measurement is obtained. If a drop of liquid, *e.g.* isopropyl alcohol, is suspended at the end of a pipette close to the laser spot on the substrate (but not touching the substrate nor entering the laser beam) and the measurement is repeated, a distinct increase in measured film thickness is observed due to adsorption of the solvent vapor to the substrate surface. When the pipette is removed, the adsorbed species desorb, and the original thickness values are obtained. Figure 3.4 demonstrates this effect observed on a 4 nm oxide film.

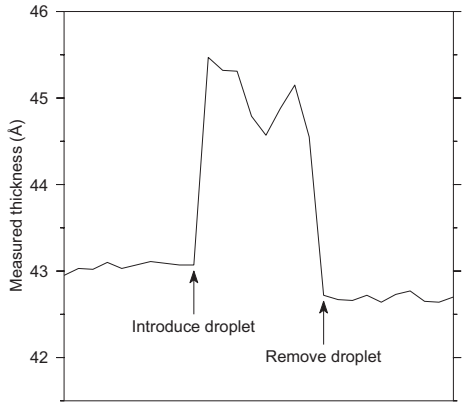

Figure 3.4: The effect of solvent vapors on ellipsometer measurements. A droplet of isopropanol is introduced on the tip of a pipette near the laser spot during a series of measurements from the same spot on an oxidized silicon wafer.

In addition to high-concentration solvent vapors (as demonstrated above), also the adsorption of atmospheric gases such as oxygen and water vapor can be seen by ellipsometry. If a thermally oxidized wafer is taken immediately after unloading from the furnace and measured, and measured again at a later time, a rising trend in the film thickness is seen. This rising trend will soon begin to even out. Since the atmosphere of a cleanroom is carefully controlled, especially in temperature and humidity (21 ± 0.5°C and 45 ± 5% RH in the Micronova [103] cleanroom), the resulting adsorbed film will lend a more-or-less constant and predictable contribution to the measured film thickness, once the wafer has been allowed to come into equilibrium with the atmosphere. Accumulation of atmospheric contaminants continues, however, at a lower rate. Despite all the precautions taken in a cleanroom, some

contamination from airborne particles and outgassing plastics will nevertheless end up on the wafer.

Figure 3.5 shows the adsorption of atmospheric gases and contaminants on the surface of a recently oxidized wafer. The thickness is measured using a fixed refractive index $n = 1.465$, the bulk refractive index of silicon dioxide. Since the wafer must cool down considerably before it can be handled, some adsorbed gases are already present in the first data point measured at $t = 4$ min, so the actual thickness of the silicon dioxide layer cannot be known for certain. The measured thickness increases rapidly during the first day, and then begins to taper off. Thus, in order to consistently (if not accurately) measure the oxide thickness, the measurement should be performed either as soon as possible after unloading the sample, or after a consistent period, say a day or two, in the laboratory air. Even after this time, the sample surface will continue to accumulate contaminants at a rate of a few Ångströms per year.

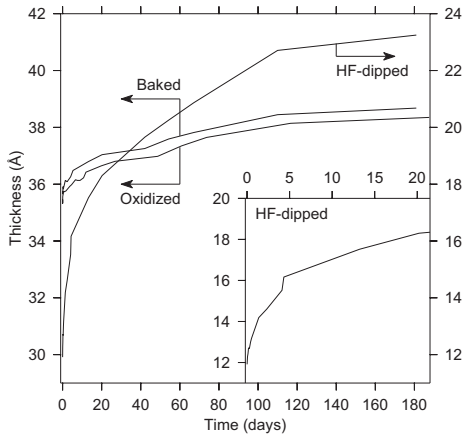

Figure 3.5: Formation of native oxide on a bare HF-dipped silicon wafer, and adsorption of atmospheric contaminants on wafers stored in a plastic box in cleanroom air. The inset shows the beginning of native oxide formation. A silicon dioxide film ($n = 1.465$) was assumed in the ellipsometer measurements.

Figure 3.5 also depicts the behavior of another oxidized silicon sample, which has been in the laboratory ambient after oxidation, but which has subsequently been baked in an oven at 120°C for 60 minutes to remove most adsorbed species. It exhibits an increase in measured thickness that is nearly identical to the recently oxidized sample. Also shown is the growth of native oxide on a wafer dipped in HF. The change in its measured oxide thickness is vastly greater than in the other two samples, as it is actually being oxidized in the laboratory ambient, instead of only adsorbing atmospheric species on its surface.

The intrinsically inhomogeneous structure of ultrathin films makes it difficult to measure their thickness accurately. Since the film stack of native oxide, deposited

film and adsorbed species is seen by the ellipsometer as if it were a single film, its refractive index is certainly different from the bulk refractive index of the deposited film. It must therefore be kept in mind that all film thicknesses herein are calculated, using a probably incorrect refractive index, from an ellipsometric signal to which contribute not only the film itself, but also any interfacial native oxides, as well as all adsorbed species. The thickness values expressed are therefore not actual thicknesses, but rather some experimental values which for the most part reflect the actual thickness in a more-or-less linear fashion.

Under controlled conditions, however, this convenient measurement does serve its purpose as a useful metric for ensuring process repeatability, and does also work as a thickness metric (albeit in arbitrary units, despite being labeled as nanometers or Ångströms) for analytical and optimization purposes. After all, one rarely requires a film of exactly 4.0 nm thickness—rather, one requires that thickness of film which gives optimal results in the end application. That thickness can be optimized just as well in arbitrary units, as in nanometers. But were an ultrathin film deposition process transferred to another fabrication facility, or the measurement instrumentation upgraded, a full process optimization procedure would likely be needed using the different arbitrary units of the new instrumentation.

3.3 Fabrication of ultrathin films

Most thin film deposition methods are best suited for thin films of "normal" thickness, *i.e.* on either side of a hundred nanometers. Thicker films can usually be produced simply by increasing deposition time (provided that film stresses do not crack the thick film), but ultimately thin films can be more problematic. In almost any process, a finite amount of time is required before the process is stabilized (*i.e.* gas flows, reactor pressure, temperature, RF power and other parameters settle at their set points). Even if process parameters are optimized for a low deposition rate (which will, of course, affect film properties as well), the deposition time may still be very short. That means the stabilization time may constitute a significant fraction of the total deposition time, and process repeatability is consequently degraded. Especially suited for ultrathin films are thermal oxidation, whose oxidation rate can be lowered by changing the oxidation temperature with little effect on oxide quality, and atomic layer deposition, whose very nature enables atomic level control of film thickness.

3.3.1 Thermal oxidation

Thermal oxidation is a well established and highly repeatable process, producing silicon dioxide films of excellent quality. In fact it is almost the only silicon dioxide process routinely used in CMOS gate dielectrics (although LPCVD oxides have also been demonstrated to work with proper annealing procedures [104], and new high-k materials are beginning to replace silicon dioxide as the gate dielectric [105,106]). Its

versatility is exemplified by the range of oxide thicknesses which can be repeatably produced: Anything between a few nanometers and several micrometers is possible. Its features in the ultrathin film regime have been published elsewhere [23–26]. In this work, a dry oxidation process using low oxidation temperature and a reduced oxygen atmosphere was devised (Publications **I**–**III** and **V**). Figure 3.6 presents some oxide thicknesses produced at 850°C temperature at 100% and 10% oxygen concentrations on (100) and (111) oriented silicon wafers. From the two data points obtained using 100% oxygen, the difficulty of fine-tuning the oxide thickness in the regime around 4 nm can be seen. Reducing the oxygen concentration to 10% decreased the oxide growth rate enough to make control of its thickness easier. The wafers are loaded into the oxidation furnace at 700°C temperature, and the temperature is ramped up to 850°C in a 5% oxygen atmosphere. The data points at 0 minutes oxidation time show the oxide thickness grown during these loading and ramping phases. After oxidation, temperature is ramped down in 100% nitrogen.

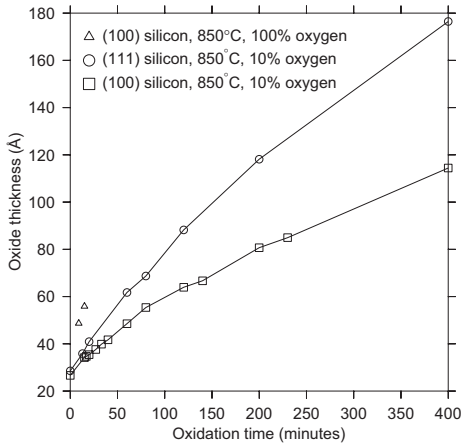

Figure 3.6: Oxidation of (100) and (111) silicon at 850°C in a 10% oxygen atmosphere. Two data points for (100) silicon in 100% oxygen are also shown.

Since the native oxide thickness on silicon is a significant fraction of the final tunneling oxide thickness, it is vital that RCA-cleaning be performed immediately prior to oxidation with an HF-dip last, and that after rinsing and drying, the wafers be loaded into the furnace without delay.

After HF treatment, the silicon surface is hydrogen terminated [107, 108], and soon begins to oxidize at a rate that greatly depends on the humidity of air or, when immersed in water, its oxygen content [109]. After some time, the exact state of the surface is no longer known. Typically after several days the native oxide will be close to its final thickness of ∼1–2 nm,[†] and the silicon surface is once again at a known and relatively reproducible state. Figure 3.5 shows the native oxidation

[†]Under certain conditions, however, electrochemical mechanisms may lead to native oxides thicker than 10 nm on patterned, metallized wafers. [110]

of (100) silicon. As can be seen from the figure, the rate of change in thickness remains higher than in the already oxidized samples for a significant time, so some process other than atmospheric adsorption must remain in effect long after HF-treatment. Also, this data shows that significant atmospheric adsorption will occur while native oxide is still growing, thus incorporation of atmospheric contaminants into the film will make the composition of the native oxide highly questionable. This only emphasizes the necessity of native oxide removal immediately prior to oxidation.

3.3.2 Atomic layer deposition

Atomic layer deposition is intrinsically suited to deposition of ultimately thin films, since it offers atomic level control of film thickness. A variety of dielectric materials can be deposited by using suitable precursor materials. Aluminum oxide is used in Publications **III**–**V** as it is an easily optimized process and has excellent dielectric properties. Native or anodic aluminum oxide has also been used previously in HECL applications on a bulk aluminum substrate.

What does produce a level of uncertainty in ALD film thickness is the onset of deposition. Once deposition has commenced, the adsorption of precursor materials on the growing film is well established and uniform over the entire substrate, but the adsorption of the first precursor monolayers may depend on the composition of the substrate surface. At the same time, the substrate surface itself may react with the precursors, or over time, with the deposited film, to change the interface properties and the effective thickness of the film.

The deposition of alumina on bare silicon surfaces has been investigated [111] using cryogenic ICP etching of the silicon substrate to demonstrate the continuity of the deposited alumina film. The film was found to become continuous after 10 deposition cycles in a TMA/water process, but after only 5 cycles in a TMA/ozone process.

A delay in the onset of deposition is evident on many metal substrates as well (or, in this case, on sputtered metal thin films). The thickness of deposited films was measured by ellipsometry after various numbers of deposition cycles, and the results are presented in Table 1 of Publication **IV**. Obviously an aluminum sample with its native oxide is suitable for immediate deposition of more alumina, but it turns out that titanium, platinum and chromium take several cycles to initiate deposition. During these first cycles, either the metal surface is modified to a suitable form for precursor adsorption, or growth nucleation occurs randomly at various sites on the metal surface to finally form a continuous and growing film. The latter mechanism would account for the observed poor HECL efficiencies of these alumina-covered metals as working electrodes: Emission of hot electrons into solution cannot occur if bare metal is exposed to the solution, and by the time the ALD film has become continuous, the initial islands have already grown too thick for efficient tunneling. No island structures were, however, seen in AFM images, nor was a region of slower deposition rate seen in ellipsometry data at the beginning of deposition.

At the silicon/alumina interface, it is likely that a native silicon dioxide will eventually form, just like one forms in an air ambient. Published results from C-V and ellipsometric measurements suggest the interfacial SiO_2 layer is 11–13 Å thick [112]. Whether the oxygen comes from the nearby alumina leaving behind a region of non-stoichiometric oxygen-deficient alumina, or by diffusion from the ambient, the properties of the composite film no doubt differ somewhat from those of the original alumina film. The thinner the deposited film, the more pronounced this change will be.

3.3.3 Other deposition methods

While thermal oxidation and ALD are easily controlled processes in the ultrathin regime, other materials deposited by other processes may have desirable properties for HECL application. Therefore silicon nitride and silicon dioxide deposited by LPCVD, PECVD and LPD were also investigated.

For production use, an LPCVD recipe for silicon nitride could be tailored to yield a sufficiently low deposition rate. For testing purposes, however, reasonable control of film thickness was obtained with existing standard recipes and short enough deposition times. Times of 0.5, 1.0, 1.5 and 2.0 minutes were used, and the resulting film thickness was still very linear with respect to time. As with thermal oxidation, RCA-cleaning and an HF-dip were performed immediately before deposition. During loading, however, the wafers are briefly exposed to high temperatures in an oxygen-containing atmosphere, therefore a native oxide is no doubt formed underneath the nitride. Etching tests in BHF confirmed that the etch rate in the last 1–2 nm of material is substantially higher than in the rest of the film, and therefore the interface consists of something other than high quality silicon nitride (Publication **III**). The Si_3N_4 film itself is remarkably uniform and completely free of pinholes, which was demonstrated by depositing 1 nm of nitride over a thick thermal oxide, and etching in BHF. Since oxide etches over 100 times faster than nitride in BHF, any pinholes in the latter would have caused visible discoloration in the oxide.

Plasma-enhanced CVD is a suitably low temperature process that metallized wafers and even some plastic substrates can be used. Deposition processes of silicon dioxide and silicon nitride were tailored to yield a lower deposition rate by reducing RF power and silane flow.

Liquid phase deposition of silicon dioxide (Section 2.2.4) is naturally a fairly slow deposition process, ∼10–60 nm/h, depending on the deposition temperature and the amount of boric acid addition [36]. It is therefore a natural candidate for the fabrication of ultrathin films. Not all its properties, however, are even near those of high-quality thermal oxide [113].

4 Hot electron electrochemiluminescence

Luminescence is the emission of light from a substance relaxing from an excited electronic state to its ground state. The excited state can be produced by various processes, *e.g.* absorption of light at a suitable wavelength (*photoluminescence*), a chemical reaction (*chemiluminescence*) or an electrochemical reaction (*electrochemiluminescence*, ECL). In ECL, the luminophore is typically not excited directly by the electrode reactions, but rather, other added chemicals (coreactants) in the sample solution are electrochemically induced to produce intermediate species, which then react with the luminophore to produce the excited state. [114]

Since the intermediate species produced are highly reactive, and the lifetime of the excited luminophore is short, luminescence is confined to the immediate vicinity of the electrode surface where the reaction chain initiates. Therefore it is natural to classify ECL as *anodic* or *cathodic* ECL, according to which electrode luminesces. Conventional ECL uses ordinary inert metal electrodes and normal electrochemical methods for potential control, usually in the common three electrode arrangement (working electrode, counter electrode and reference electrode) [114]. Cathodic *hot electron-induced ECL* (HECL) differs in the way the electrochemical reaction is initiated: Instead of reduction/oxidation reactions occurring directly on the electrode surface, hot electrons are tunnel emitted from an insulator-covered cathode (working against an inert metal anode in a two-electrode configuration using coulostatic electrical pulses at high voltage) into the sample solution [38, 114]. These electrons become solvated and act as the initial reducing species in the ECL reaction chain.

4.1 Hot electron emission into aqueous solution

Hot or solvated electrons are extremely strong reducing species in solution. This is hardly surprising, since reduction, *i.e.* changing of the oxidation state of an atom from a more positive state to a more negative state, involves gaining an electron from somewhere. Most commonly the source of an electron is another chemical species which is correspondingly oxidized as it loses an electron, or the electron is supplied from a non-reactive metal electrode, *e.g.* in an electrolysis cell. The potentials of the reduced species that can be achieved by conventional methods are, however, limited by the potential of the reducing species, or in an electrolysis cell, by the breakdown of water that begins to occur above 1.23 V [115, pp. 8.28]. Hot electron electrochemistry can push back the boundaries of conventional electrochemistry by introducing more strongly reducing species into the equation.

Traditionally hot electrons have been produced in solution by methods such as pulse radiolysis [116–118] or photoionization [119,120]. Pulse radiolysis involves producing an intense electron beam pulse in a linear accelerator and directing it into the sample. The fast phenomena induced by this pulse are then detected by optical means, using either Cherenkov radiation produced by the electron beam itself, or more recently

a laser pulse externally synchronized to the electron pulse. This is the method by which hydrated electrons were initially discovered in 1962 by Boag, Hart and Keene [121, 122]. Photoionization uses high-energy laser pulses to produce solvated electrons by two-photon excitation, which are again detected spectroscopically by a subsequent probe pulse.

Modern pulse radiolysis and photoionization systems offer extremely high time resolutions of picoseconds and below, making them ideal for investigating the electron solvation process and other fast phenomena. They are, however, rather cumbersome methods if the objects of study are the much slower electrochemical reactions induced by the solvated electrons. For these purposes, there is a much simpler method of producing solvated electrons, namely tunnel emission of hot electrons into solution from a conductive cathode covered by an ultrathin insulating film, while an inert electrode such as platinum serves as the anode.

This tunnel emission mechanism in the creation of cathodic electrochemiluminescence was first detailed by Kulmala *et al.* [38, 39]. The tunneling process is basically the same as in non-volatile memory devices [123] and M/I/M diodes [124], and emission of electrons from this metal/insulator/electrolyte (M/I/E) junction into solution is similar to the tunnel emission of electrons into vacuum [125, 126]. This tunnel emission was demonstrated by the electrochemiluminescence produced in certain luminophores. Especially (9-fluorenyl)methanol (FMOC-OH) produces luminescence at 309 nm (4.0 eV), which is higher in energy than is possible in aqueous solution with ordinary active metal electrodes. Also, since the onset of luminescence from various luminophores with differing redox potentials occurred at the same pulse potential (and in fact multiple luminophores could be excited simultaneously [39]), their excitation pathways must begin with the same primary process. The role of hydrated electrons as the common intermediary is supported by the luminescence-quenching action of electron scavengers such as hexaamminecobalt(III) ($Co(NH_3)_6^{3+}$), nitrate (NO_3^-) and dihydrogen phosphate ($H_2PO_4^-$). The efficiency of the quenching action was directly correlated with the reactivity of the electron scavenger, hexaamminecobalt(III) being the most reactive ($k = 8.7 \cdot 10^{10}$ $dm^3mol^{-1}s^{-1}$), followed by nitrate ($k = 9.7 \cdot 10^9$ $dm^3mol^{-1}s^{-1}$) and dihydrogen phosphate ($k = 1.9 \cdot 10^7$ $dm^3mol^{-1}s^{-1}$) [38].

The thickness of the tunneling dielectric is critical for the efficient generation of hydrated electrons. For the thinnest dielectric films (below ∼4–5 nm or so), electrons are transported ballistically through the dielectric, without entering the dielectric's conduction band and with low loss of energy. In thicker films, the Fowler-Nordheim tunneling mechanism dominates, and electrons are transported through the insulator's conduction band. Direct tunneling results in higher-energy electrons above the conduction band edge of water (hot electrons) which may then thermalize and become solvated (aqueous electrons, e_{aq}^-). Due to band-bending under strong cathodic pulse conditions (Figure 4.1), the FN-mechanism results in lower-energy electrons, and e_{aq}^- cannot be efficiently produced. The observation of strongest electrochemiluminescence when dielectric thickness is in the vicinity of 5 nm thus also supports e_{aq}^- as the initial reactant [38].

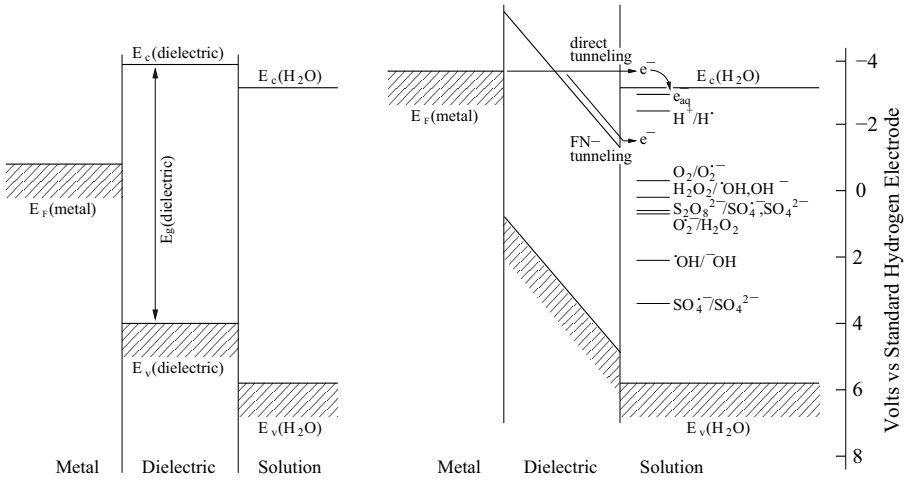

Figure 4.1: Energy diagram at the surface of a dielectric-coated HECL working electrode without applied voltage (*left*) and during strong cathodic polarization (*right*). [38]

Pulse radiolysis studies have shown that in low concentrations aqueous electrons are unreactive towards water. This enables them to react even with low concentrations of other solvated species in aqueous solution. In high concentrations, however, aqueous electrons form pairs which readily react with water to form hydrogen [127].

4.2 Application of hot-electron electrochemiluminescence

Many luminophores that produce anodic ECL will also produce cathodic HECL. However, many other compounds, *e.g.* some Tb(III) chelates [128], produce HECL although they are not luminescent under ordinary anodic ECL. Table 4.1 presents some HECL luminophores which have been investigated and reported in the literature by Kulmala *et al.*

One application of hot electron electrochemistry is the determination of the concentration of luminophores in solution or on the surface of the working electrode by hot electron electrochemiluminescence. This is useful, as many luminophores can be bound to biological materials such as antibodies, DNA, proteins *etc.*, and can work as labels in the determination of those compounds. Immunoassays and DNA hybridization assays have long utilized radioactive or fluorescent labels to detect the analyte [160–163], and lately various nanoparticles have been utilized as well [164–166]. Anodic ECL has also been used as a detection method [167]. Cathodic hot electron electrochemiluminescent assays differ mainly in the principle of detection of the label. HECL offers several advantages, including simpler instrumentation, the possibility of simultaneous excitation of multiple labels and multi-analyte determination based on spectral response (ranging from the 309 nm

Luminophore	References
Terbium(III) ions	[129]
Various terbium(III) chelates:	
2,6-pyridinedicarboxylic acid (dipicolinic acid, DPA)	[130]
4-(phenylethyl)-2,6-bis[N,N-bis(carboxymethyl)aminomethyl]pyridine	[130]
N^1-(4-isothiocyanatobenzyl)diethylenetriamine-N^1,N^2,N^3,N^3-tetraacetate	[131]
N^1-(4-aminobenzyl)diethylenetriamine-N^1,N^2,N^3,N^3-tetraacetate	[132, 133]
2,6-bis[N,N-bis(carboxymethyl)aminomethyl]-4-(phenylethyl)phenol	[128, 130, 133]
2,6-bis[N,N-bis(carboxymethyl)aminomethyl]-4-methylphenol	[131, 132, 134, 135]
2,6-bis[N,N-bis(carboxymethyl)aminomethyl]-4-benzoylphenol	[37, 128, 132, 133, 135–140]†
Yttrium and gadolinium chelates:	
2,6-bis[N,N-bis(carboxymethyl)-aminomethyl]-4-methylphenol and	
2,6-bis[N,N-bis(carboxymethyl)-aminomethyl]-4-benzoylphenol	[134, 141]
Europium(III) 2,6-bis[N,N-bis(carboxymethyl)-aminomethyl]-4-benzoylphenol	[142]
Ytterbium, chelated by 11 different ligands	[143]
Ruthenium(II) chelates:	
tris(2,2′-bipyridine) (commonly denoted as $Ru(bpy)_3^{2+}$)	[38, 130, 136, 144–146]†
[4-ethoxycarbonyl-4′-carboxy-2,2′-bipyridine]bis(2,2′-bipyridine)	[147]
Heteronuclear yttrium(III)-dysprosium(III) and yttrium(III)-samarium(III)	
2,6-bis[N,N-bis(carboxymethyl)aminomethyl]-4-benzoylphenol chelates	[148]
Metalloporphyrins (platinum(II) coproporphyrin)	[149]
Coproporphyrin ketone	[130]
Fluorescein (2-(6-hydroxy-3-oxo-xanthen-9-yl)benzoic acid)	[150, 151]
Fluorescein isothiocyanate	[130]
Eosin	[130]
Luminol (5-amino-2,3-dihydrophthalazine-1,4-dione) and derivatives	
N-(6-aminohexyl)-N-ethylisoluminol (AHEI) and	
N-(6-aminobutyl)-N-ethylisoluminol (ABEI)	[152, 153]†
Lucigenin (N,N′-dimethyl-9-9′-biacridiniumdication)	[154]
9-fluorenylmethyl chloroformate (FMOC)	[130]
(9-fluorenyl)methanol (FMOC-OH)	[38, 136]
Rhodamine B	[155]
Tetramethylrhodamine (TAMRA) dye	[156]
Coumarin derivatives: 7-hydroxy-4-methylcoumarin (HMC),	
6,7-dihydroxy-4-methylcoumarin (DHMC) and	
7-amino-4-methylcoumarin (AMC)	[130, 157]
1-aminonaphthalene-4-sulfonate (ANS)	[136, 158]
Toluene, phenol	[39]
Solutions of silver nanoclusters	[159]

†Includes Publications **I**–**IV**

Table 4.1: Some luminophores tested for HECL by Kulmala *et al.*

near-UV emission of FMOC-OH [38] to 977 nm near-IR of Yb(III) chelates [143]) or time-resolved detection (lifetimes ranging from microseconds of $Ru(bpy)_3^{2+}$ to milliseconds of Tb(III) chelates [142, 144]), and a wider variety of label compounds. Compared to fluorescence methods, where the excitation is commonly done by ultraviolet radiation, the sample cell need only be transparent to the emitted radiation, since excitation is done electrically. The electrical excitation is often accomplished by a coulostatic pulse generator which can be a very simple design [133], and which is vastly cheaper than any UV laser currently on the market.

Luminescence occurs close to the surface of the working electrode (cathode), since the high reactivity and consequent short lifetime of the species involved precludes long diffusion distances. The distance from the working electrode, within which HECL occurs, has been estimated from e_{aq}^- reactivity and diffusion coefficients to be on the order of 200 nm [131, 168]. To perform an immunoassay, therefore, antibodies (or complementary oligonucleotide targets in the case of a DNA hybridization assay [156]) can be bound directly onto the surface of the working electrode. An immunoassay can then be performed by two general methods, as a non-competitive (or "sandwich") assay, or a competitive assay. The non-competitive assay proceeds as follows [133, 137, 138, 169, 170]:

- The HECL working electrode is coated with monoclonal antibodies.
- Sample solution containing the analyte protein and labeled secondary antibodies is introduced to the HECL working electrode and incubated. Analyte proteins bind to antibodies on the electrode surface, and labeled secondary antibodies bind to the proteins.
- After rinsing, an electrolyte solution is introduced and HECL is measured from the working electrode surface.

This results in the analyte molecule being "sandwiched" between two antibodies, one bound to the electrode, the other labeled with a luminophore. Alternatively, a competitive assay can be performed thus [131, 169]:

- The HECL working electrode is coated with antibodies.
- Sample solution containing the analyte protein and a known concentration of separately synthesized labeled analyte is introduced to the HECL working electrode and incubated. Both the labeled and unlabeled analyte bind to the antibodies in the ratio of their concentrations in the solution.
- After rinsing, HECL is measured as above.

The competitive assay results in all the proteins (both the unlabeled analyte proteins, and the added labeled proteins) being bound to single antibodies on the electrode. Thus this method requires only a single epitonic site (*i.e.* a site to which an antibody can selectively bind) on the analyte protein. The HECL signal detected in

the assay, however, reflects the relative concentration of the *added* protein, not the analyte itself. Thus, when the analyte concentration is low, the relative change in the HECL signal is small, resulting in lower sensitivity. In the non-competitive assay, on the other hand, the HECL signal directly reflects the analyte concentration, but at least two epitonic sites are required on the analyte molecule. [133, 169]

In either case, the procedure may be simplified by omitting the final rinse (making it a homogeneous assay, where both bound and unbound labels are present at the time of detection, as opposed to a heterogeneous assay, where only bound labels remain). Since HECL only occurs close to the electrode surface, the surface concentration of bound luminophores will dominate the HECL signal [131, 133].

The sensitivity and selectivity of HECL can be improved by using optical interference filters to select only the desired emission line of the luminophore, thus reducing interference from other possible luminophores and broadband background emission. Also, since some luminophores exhibit relatively long luminescence lifetimes up to milliseconds [144], it is possible to use time-resolved detection to count only the long-lived luminescence signal and to exclude short-lived interference *e.g.* intrinsic cathodic luminescence of the oxide film itself [129]. Alternatively, different labels can be used to simultaneously detect multiple analytes, using either wavelength or time discrimination, or both [39, 142, 144].

The HECL method has been slow in its adoption by other research groups. Some interesting recent developments include the discovery of efficient hot-electron emission from antimony oxide covered gold-antimony alloy electrodes, as reported by Wu *et al.* [171]. The significance of a gold-based working electrode lies in the ease of creating self-assembled thiol monolayers on its surface, for the purpose of binding antibodies. Another interesting application by the same group utilizes the intrinsic cathodic ECL of an oxide-covered glassy carbon electrode, which is effectively quenched by the attachment of ferrocene at its surface. When ferrocene was used to modify a molecular beacon sensitive to a given DNA fragment, the intensity of the intrinsic ECL became dependent on the concentration of that DNA fragment in sample solution, essentially creating a reagent-free DNA biosensor [172].

Since the various optical analysis methods commonly used in microfluidic applications are based on different physical phenomena, and are sensitive to different analytes, direct comparison between them is difficult. Generally, laser-induced fluorescence (LIF) is one of the most sensitive, as it is well suited to analysis of small fluid volumes. Picomolar detection limits have been reported for analytes such as rhodamine 6G by LIF. Mercury lamp-based fluorescence methods are significantly less sensitive, with nanomolar detection limits reported for analytes such as fluorescein isothiocyanate (FITC). Absorbance-based methods do not perform well in microfluidic devices, as optical paths within the sample are short. Fluorescein has been detected by UV-absorbance only down to micromolar levels. [173, 174]

HECL detection with some luminophores can be sensitive down to sub-nanomolar concentrations, thus placing it on par with lamp-based fluorescence methods. As

demonstrated later in this chapter, HECL will also work with very small sample volumes, down to 15 µl. The sample must, however, be spread over a sufficient surface area for efficient detection, which consumes real-estate on the microfluidic device, but is easily accomplished *e.g.* with PDMS fluidics.

4.3 Materials for HECL electrodes

The HECL sample cell normally contains two electrodes: the working electrode (cathode) and counter electrode (anode). The counter electrode's effect on HECL performance has not been investigated too extensively, as the electron tunneling and subsequent HECL occur on the working electrode only. The counter electrode must simply provide electrical contact to the solution, and resist anodic oxidation during the electrical pulses. A platinum wire has been used as the counter electrode in most work, although transparent counter electrodes of indium tin oxide (ITO) coated glass or plastic have also been used [133]. The working electrode, on the other hand, is of utmost importance in HECL. The factors influencing its performance are the conductive electrode material itself, the material of the tunneling dielectric, and the thickness of the dielectric.

Early work used for the most part aluminum or magnesium working electrodes, utilizing either the native oxide, or an anodically formed oxide, as the tunneling dielectric [37–39]. Sometimes a fresh anodic oxide was formed on the working electrode *in situ* between the cathodic pulses [39]. Thermally oxidized highly conductive silicon electrodes have been used in Publications **I** and **II** and other studies [137, 138], as well as anodically oxidized silicon [38, 39]. In an optical detection system such as HECL, transparent electrodes offer an obvious advantage. Therefore some work has been done with transparent working electrodes. Zinc oxide, when doped with group-13 elements such as aluminum, behaves as an *n*-type semiconductor, and is optically transparent. It has been used in thin film form on glass (*n*-ZnO:Al glass), covered by a tunneling dielectric of ALD-deposited MgO [135] or Y_2O_3 [128].

Silicon is an especially attractive working electrode material, since it can be made highly conductive by doping with boron (*p*-type) or phosphorus or antimony (*n*-type), and an exceptionally high-quality dielectric layer of silicon dioxide can be made on its surface simply by thermal oxidation. Also, silicon dioxide is very resistant chemically, being practically inert against everything except hydrofluoric acid (HF) and some other fluorides. The effects of oxidation conditions on are investigated in Publication **III**.

Both silicon dioxide and aluminum oxide, which have proved to be excellent tunneling dielectrics for HECL application, can be produced by many different methods. Certainly the most convenient is the native oxide always present on an aluminum foil, and after any extended storage, on a silicon wafer (although the latter is without doubt of dubious quality, and it is questionable whether it can honestly be called SiO_2 at all, as discussed in Section 3.3.1). More controlled methods of producing the dielectric are therefore preferable, and other dielectric materials may also offer good

HECL performance and possibly other advantages *e.g.* in the binding of antibodies to the electrode surface. Therefore thermal oxidation, PECVD and LPD of silicon dioxide, ALD of aluminum oxide, and PECVD and LPCVD of silicon nitride have been tested for the creation of the tunneling dielectric (Publications **III** and **IV**).

Tunneling dielectrics were evaluated both in terms of HECL emission intensity at optimal film thickness, as well as stability along the course of an extended measurement. The effect of dielectric thickness on HECL performance is shown for selected material combinations in Figure 4.2, left. ALD Al_2O_3 was found to be an excellent tunnel dielectric, comparable to thermal SiO_2. Surprisingly, PECVD SiO_2 performed equally well, in both intensity and stability, despite its low deposition temperature. While the thickness of thermal SiO_2 is quite critical for optimal HECL performance, the deposited dielectrics exhibit wider usable thickness ranges. Shown in Figure 4.2 are Al_2O_3 films deposited with a TMA/H_2O process. Similar results were seen with a TMA/O_3 process, however the usable thickness limits were lower, possibly due to a denser film formed by the more aggressive oxidant.

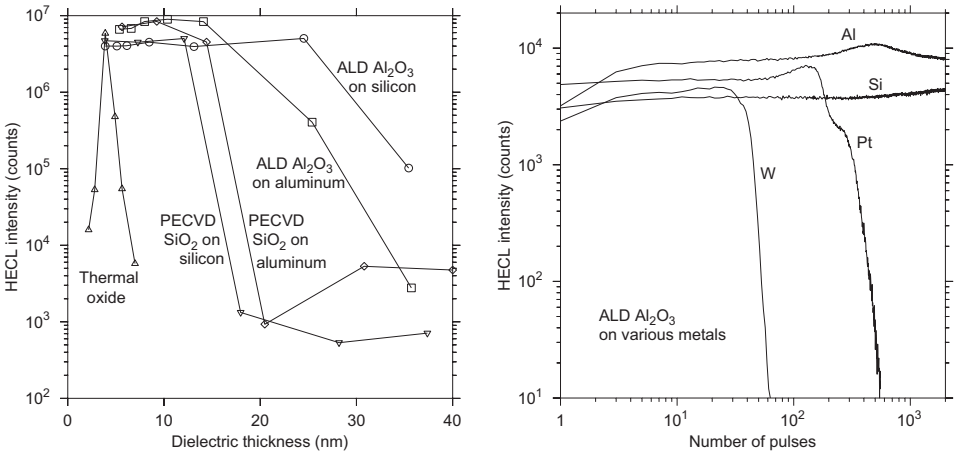

Figure 4.2: *Left:* HECL intensity with various dielectric materials and thicknesses, integrated over 1 000 measurement pulses. *Right:* HECL intensity over consecutive individual measurement pulses, using various electrode materials and Al_2O_3 dielectric.

The stability of the HECL signal over the course of a measurement was greatly affected by the underlying metallization of the working electrode, as shown in Figure 4.2, right. Individual intensities measured from 2 000 consecutive measurement pulses are shown, using ALD-deposited Al_2O_3 dielectrics over four different electrode materials. The performance of silicon and aluminum is excellent over the entire measurement. Platinum and tungsten, on the other hand, start out with good intensity, but the intensity soon falls. In fact, platinum gives a somewhat higher signal than silicon, if only a hundred pulses are recorded and integrated. If, however, thousands of pulses should be integrated, only silicon or aluminum electrodes can be used. Tungsten also begins at a respectably high HECL intensity, but its intensity

falls even sooner. Copper, chromium and titanium never gave any significant signal. Similar results were seen with a PECVD SiO_2 dielectric. The electrode materials investigated in Publications **III** and **IV** are summarized in table 4.2.

Electrode	Performance	Special features
Silicon	Excellent	Thermal oxidation possible
Aluminum	Excellent	Dual purpose as sacrificial material
Platinum	Mediocre	Signal falls after a few hundred pulses Single-metal integrated electrodes
Tungsten	Poor	Signal falls after tens of pulses
Titanium	Bad	Practically no HECL-signal
Chromium	Bad	Practically no HECL-signal
Copper	Bad	Oxidizes during loading Practically no HECL-signal

Table 4.2: Features of various HECL electrode materials

Since vast differences in HECL performance were seen with identical tunneling dielectrics, the eventual failure cannot be intrinsic to the dielectric material itself. Rather, the failure must originate at the electrode/dielectric interface. A strong correlation was seen between HECL signal intensity and delayed deposition of Al_2O_3 and SiO_2 on the metal surface (Publication **IV**), indicating that growth initiation and resulting interface quality affect the HECL performance. The best performers, aluminum and silicon, readily grow a native oxide, and may thus also be able to self-heal any defects in the dielectric film.

Alternatively, delayed initiation of deposition might lead to an island-type growth nucleation, which would produce a non-uniform and thus suboptimal tunneling dielectric film. However, neither ellipsometrically measured thickness data from the early stages of deposition, nor AFM images of the bare and dielectric covered metal surfaces, supported this explanation.

The motivation for testing deposited metal thin films as the conductive material of the working electrode is the possibility of using insulating substrates for HECL devices. Firstly, insulating substrates may offer advantages *e.g.* when combining HECL detection with electrical separation methods such as electrophoresis. Secondly, plastics are insulating materials by nature, and offer interesting possibilities for fabrication of fluidic systems by standard plastic fabrication methods like hot embossing or mold extrusion, not to mention simply being cheap substrate materials. The low temperature ALD Al_2O_3 and PECVD SiO_2 processes are strong candidates for making HECL devices on such substrates, as well as for back-end processing of HECL detection on a chip already containing other devices or electronics. All the deposited dielectrics investigated are summarized in Table 4.3.

Dielectric	Performance	Deposition temperature	Special features
Thermal SiO_2	Excellent	High (850°C)	Excellent thickness control Silicon substrates only
PECVD SiO_2	Excellent	Low (300°C)	
LPD SiO_2	Bad	RT (25–40°C)	Practically no HECL signal
LPCVD Si_3N_4	Excellent	High (770°C)	
PECVD Si_3N_4	Mediocre	Low (300°C)	Fluctuating HECL signal
ALD Al_2O_3	Excellent	Low (110–230°C)	Excellent thickness control Even lower temperatures possible by optimizing the deposition process

Table 4.3: Features of various HECL dielectric materials and deposition methods.

4.4 An integrated electrode HECL chip

For convenient point-of-care diagnostics, an integrated microsystem is desired. The HECL apparatus consists of a pulse generator, the sample cell containing the working and counter electrodes, and an optical detection and data acquisition system. Only the working electrode must necessarily be replaced in normal use, as its tunneling dielectric eventually wears out and ceases to function, and also any antibody coating of the electrode is obviously suited for a single use only.

In most previous work, the sample cell has consisted of a base assembly with electrical contacts, a machined slot for the working electrode, and a PTFE sample cell with an o-ring to create a seal against the working electrode (Figure 4.3, far left). The PTFE sample cell has been manually installed and tightened against the electrode for each individual measurement. The photomultiplier tube assembly for optical detection is finally attached to the base assembly. This repeated disassembly and reassembly of the sample cell is cumbersome and messy. Also the PTFE cell and platinum counter electrode wire need to be cleaned after each measurement to prevent cross-contamination. For practical point-of-care operation, and to preserve the sanity of a laboratory technician routinely working with the HECL method, an integrated system would be preferred, where all fluidics, replaceable parts and contaminated parts (*e.g.* the counter electrode) are integrated into a single disposable chip or cartridge. This chip should be rapidly exchangeable in the measurement device, and preferably should require minimal tools and technique to utilize in a controlled and repeatable fashion.

Based on results with plain silicon or metallized electrodes with various tunneling dielectrics (Publications **III** and **IV**), two primary designs were chosen for further development: a thermally oxidized Si/SiO_2 working electrode, and a thin film Al/Al_2O_3 working electrode on a glass substrate, with an ALD-deposited dielectric. While excellent performance had been obtained with PECVD SiO_2 tunneling dielectrics, the instabilities of the PECVD process made it less desirable at this time. There is nothing wrong with the PECVD silicon dioxide process *per se*, and with further development it should become controlled and repeatable enough to be used

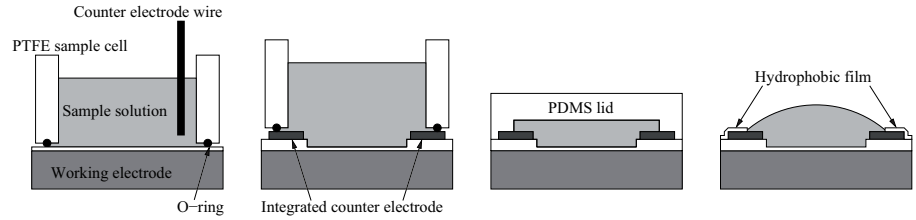

Figure 4.3: Variations on a HECL chip: a plain working electrode chip with a platinum wire counter electrode (*far left*), an integrated electrode chip (*middle left*), an integrated electrode chip with bonded PDMS capillary-filling fluidics (*middle right*), and an integrated electrode chip with hydrophobic sample confinement (*far right*).

in this application as well. The PECVD SiO_2 dielectric would also be usable with alkaline sample solutions, which the ALD Al_2O_3 dielectric cannot withstand.

The platinum counter electrode was integrated onto the same chip as the working electrode (Publication **V**), as shown schematically in Figure 4.3, middle left. A variety of electrode geometries was tested, including interdigitated electrode structures of various widths and densities, ring-shaped electrodes and simple wires. Examples of geometries tested are shown in Figure 2 of Publication **V**. Since the electrode geometry had very little effect on HECL efficiency (provided that both the working and counter electrode had sufficient surface area), two of the simplest designs were chosen. In the glass device, 200 µm separation was maintained between the working and counter electrodes. In the silicon version, a thick thermal oxide dielectric insulated the counter electrode from the substrate. All processes used cheap plastic film photomasks with limited resolution of some tens of micrometers, so alignment tolerances of 100 µm were maintained. The fabrication processes are detailed in Appendices A.1 and A.2, and results are presented in Section 4.7. Both the silicon and the glass devices were 10×19 mm in size.

Since platinum metallization is needed for the counter electrodes, the fabrication process would be simplified by using platinum as the working electrode material as well. Aluminum was, however, preferred due to its better HECL efficiency (Publication **IV**). A single metal process with platinum working electrodes could, however, be used in applications where ultimately high sensitivity is not of primary importance. It is possible, however, that any jagged edges left by the lift-off process (Figure 2.4 on page 36) would be detrimental in the working electrode, so some optimization of the lift-off process may be required.

Aiming for low-cost, disposable devices, DuPont™ Kapton® HN 500 polyimide and Teijin® Teonex® Q65 FA polyethylene-naphthalate films have also been tested as the substrate material. Being insulating materials, they are similar to glass as a substrate. The biggest difference is in the practical issues of handling thin plas-

tic films.† Although especially Kapton® can tolerate relatively high temperatures, other polymers may not withstand the standard 210°C ALD temperature. Also Kapton® and Teonex® exhibit some shrinkage and warping at high temperature, which can hinder alignment of the last masklevels in the fabrication process. To that end, the effect of lowered ALD temperature on HECL performance was preliminarily tested. Figure 4.4 shows the results with silicon, aluminized Kapton® and aluminized Teonex® substrates. The deposition temperature is obviously not critical. At 80°C the unoptimized ALD process probably turned to CVD behavior, producing a film six times thicker than nominal. Since electrically high-quality alumina films have been deposited at temperatures down to 33°C [31], there is no evident reason why 80°C or even lower deposition temperatures should not work in a HECL application, once the deposition process is optimized. This work is ongoing and yet unpublished.

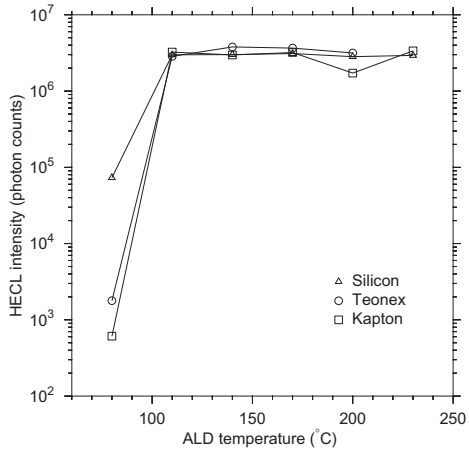

Figure 4.4: The effect of ALD temperature on HECL signal intensity with various substrates.

4.5 Integration of a fluidic system on the HECL chip

Two approaches to fluidics were tested with integrated electrode silicon HECL devices: hydrophobic sample confinement, and enclosed PDMS chambers (Publication **V**). The processing steps for hydrophobic confinement are detailed in Appendix A.1, and fabrication of the PDMS chambers is detailed in Appendix A.3. Another method of producing fluidic chambers is SU-8 photopatternable epoxy [52], and preliminary tests showed that the SU-8 process does not leave any residues on

†Deposited films and photoresist tend to distort the substrate. Therefore carrier wafers are used during sputtering, and in lithography, the aligner must not release the wafer vacuum between loading and exposure stages. Wet processing, normally done on a batch scale, is done one substrate at a time, since the flexible substrates do not stay in an ordinary wafer cassette.

the working electrode, which would hinder HECL performance. However, the adhesion of SU-8 to silicon dioxide is poor, and enclosed channels on the integrated HECL devices could not be produced by that method.[†] One possible alternative similar to SU-8 could be ORMOCER®[‡] microfluidics [176].

The hydrophobically confined HECL devices have a plasma-deposited hydrophobic fluoropolymer ring, patterned by lift-off, around the electrode (Figure 4.3, far right). They are processed to completion on the wafer scale, and are therefore suited as such to mass production. Their use in a modified sample holder (Figure 4.5) is simple: The chip, with its electrical contact pads at one end, is inserted into the sample holder containing wire springs for front side electrical contacts, and a metal base for backside contact to the substrate. The electrode chip is adequately held in position by the force of the contact springs. 100 µl of sample solution is pipetted onto the working electrode, where it reproducibly forms a nearly hemispherical droplet. No further assembly of the sample holder is needed, save for lifting the photomultiplier tube onto the base assembly. After measurement, the sample solution can be absorbed into a piece of tissue paper before removal of the electrode chip from the sample holder.

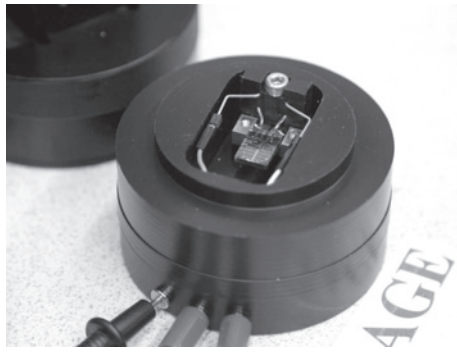

Figure 4.5: The new sample holder for HECL measurements. A silicon HECL chip with a PDMS lid is shown inserted into the holder. The two front side contacts and the substrate contact are wired to the three terminals in the holder base. A separate photomultiplier tube assembly fits over the sample holder.

The PDMS chips (Figure 4.3, middle right) were filled with 15 µl of sample solution by dipping the inlet channel at the end of the chip into a drop of sample solution. The chip was then attached to the same sample holder for measurement. The manufacture of the PDMS fluidic chips, however, requires more manual processing, although the process could surely be automated if large-scale production were being considered. To some degree, the whole PDMS fluidic system was considered only a proof-of-concept design to demonstrate the applicability of HECL detection in

[†]Newer SU-8 variants supposedly have improved adhesion to many substrates including glass [175]. Coolant water and silicon dust entering the fluidic chambers during wafer dicing would, however, remain a problem.

[‡]ORMOCER® is a trademark of the Fraunhofer-Gesellschaft zur Förderung der angewandten Forschung e.V. München.

integrated microfluidic systems. While an integrated electrode chip with a sample chamber filling by capillary force is a useful device, its use in actual practice is limited by the decreasing hydrophilicity of the PDMS surface over time. After several days of storage, the sample chamber no longer fills by capillary action. However, this does not preclude its use as part of a pressure-driven microfluidic system, nor is this design of integrated fluidic chip necessarily limited to PDMS: any other plastic or other optically transparent material that can be bonded to the HECL chip by adhesive or other means can be used to create the sample chamber. By choosing a suitable material, reliable capillary filling of the chamber can be assured.

4.6 Restoration of PDMS hydrophilicity

In the course of this work, it was observed that the hydrophilic nature of a PDMS sample chamber could be restored even after months of storage. The completed PDMS fluidic HECL chips were briefly subjected to the same oxygen plasma treatment as in their manufacturing stage (Appendix A.3, step 16), after which they could again be filled by capillary action.

To further investigate this phenomenon, long PDMS channels with dimensions of 100×50 µm, 200×100 µm and 500×350 µm (width×height) were fabricated and bonded to silicon, and allowed to become hydrophobic during several weeks or even months of storage. They were subsequently exposed to the oxygen plasma (Technics Plasma GmbH[†] TePla-400 reactor, 800 W RF power, 800 sccm O_2 flow, ∼2.3 mbar pressure) for varying lengths of time, and the length to which a droplet of water filled the channel by capillary action was measured for each. Figure 4.6 shows the results. The parabolic shape of the curve suggests that whatever reactive oxygen species are responsible for modifying the PDMS surface to a hydrophilic state, they diffuse in the vacuum process inside the enclosed PDMS channel and reactivate its inside surfaces to a hydrophilic state again. Tan *et al.* have recently reported on a similar method in the device fabrication stage to extend the time the PDMS remains hydrophilic [177]. Apparently the same method is also effective for PDMS devices that have already become hydrophobic.

While a plasma reactor is decidedly not practical as part of a point-of-care microanalytical procedure, this method does facilitate looser analysis schedules in the laboratory and research environment.

4.7 Results

As mentioned previously, the effect of electrode geometry was found to be noncritical in the integrated HECL chip, and maximizing the working electrode surface area was the primary criterion in attaining high sensitivity. However, the addition of a fluidic system—either hydrophobic confinement or a PDMS sample chamber—changed this.

[†]Now PVA Tepla AG.

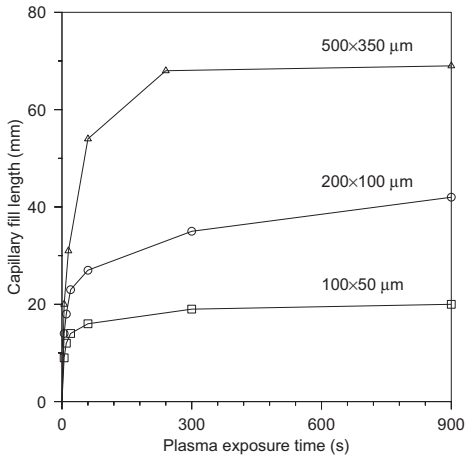

Figure 4.6: Restoration of the hydrophilicity of an enclosed PDMS channel, measured as filling length by capillary action after varying treatment times in an oxygen plasma. The channel dimensions (width×height) are shown.

When an electrical pulse is applied between the working and counter electrodes, the aim is to create a potential difference across the tunneling dielectric and thus to effect tunneling of electrons into the sample solution. However, since the counter electrode is separated from the working electrode by the sample solution itself, which is of finite electrical conductivity, a potential gradient is formed in the solution as well. As long as the change in potential within the sample solution is small compared to the potential change across the tunneling dielectric, it has little effect on anything. Such is the case in the standard measurement setup with its PTFE sample cell that accommodates 500 µl of sample solution. However, when the sample solution is drawn into a large-surface area but relatively shallow PDMS sample chamber, resistance within the solution increases drastically, and the resulting voltage drop within the solution increases with lateral distance from the counter electrode. This means a consequently smaller potential difference across the tunneling dielectric, as distance from the counter electrode increases. That, in turn, confines HECL to the immediate vicinity of the counter electrode's edge, lowering the overall HECL signal. The same effect occurs, to a lesser degree, in the hydrophobically confined sample setup, where the sample solution exists as a thicker film than in the PDMS sample chamber, but still thinner than in the PTFE cell.

The non-uniformity of HECL emission in various fluidic setups could be clearly seen in long-exposure photographs of the devices in operation (Figure 5 in Publication **V**). This qualitative information together with HECL intensity measurements with standard sample solutions helped design a suitable electrode mesh which is dense enough to produce uniform, high-intensity luminescence, yet not too dense to waste the valuable surface area of the working electrode. Figure 4.7 shows calibration curves obtained for the various types of devices with their optimized electrode

geometries. Evidently, the addition of on-chip fluidics (hydrophobic confinement or a PDMS chamber) degrades the sensitivity of the device somewhat, but sub-nanomolar sensitivity is still attainable.

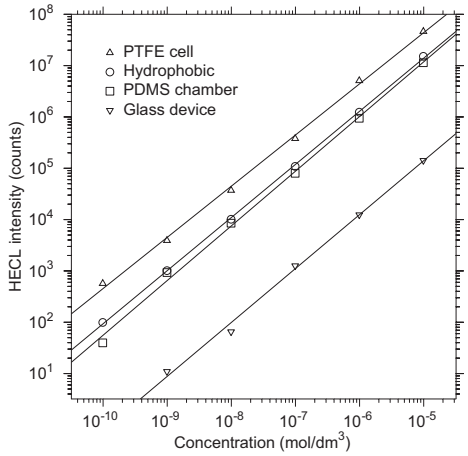

Figure 4.7: Calibration curves of various integrated HECL devices. Three silicon devices are shown: without on-chip fluidics in a PTFE sample cell (as shown in Figure 4.3, far left), with hydrophobic sample confinement (Fig. 4.3, far right), and with a capillary-filling PDMS sample chamber (Fig. 4.3, middle right). A glass device without on-chip fluidics is also shown.

Since HECL is believed to occur only within 200 nm or so of the working electrode's surface [131, 168], most of the sample solution in any measurement setup never participates in the luminescence reactions. Thus an arbitrarily small amount of sample might be concluded to suffice for a HECL analysis. In practice, however, other factors limit how small the sample volume can be made. The voltage drop within the sample solution becomes worse as the height of the PDMS sample chamber is decreased. This could be alleviated either by the use of a denser counter electrode mesh or, preferably, a transparent counter electrode of equal surface area, arbitrarily close to the working electrode. However, a more serious problem would likely be encountered. The PDMS sample chambers were initially fabricated in two heights, 50 µm and 350 µm. The latter was used for most tests, and it performed well once the electrode geometry had been optimized. The former, however, never produced significant HECL signals. Even the increased electrical resistance in the thinner sample solution film could not account for its poor performance. Rather, the emission intensity was found to start out normal (albeit decreased due to the aforementioned resistance), and then to collapse to zero, as shown in Figure 6 of Publication **V**. After measurement, the fluidic chamber was found to be nearly empty of liquid, purged by the action of gas bubbles formed during the HECL measurement. These may be either oxygen formed at the anode, or hydrogen formed by aqueous electron pairs reacting with water [127]. Bubbles were also seen in the 350 µm high fluidic chips, but their larger total volume was better able to accommodate some bubbles without purging the sample completely out of the chip. These factors will most likely limit the sample volume in HECL detection to a minimum of ∼15 µl.

5 Microhotplate gas sensor

The gas sensor component, with the working name *Lakana*, was developed as a testing platform for different gas sensor materials in microhotplate (MHP) gas sensors. The primary material in mind was tin dioxide, the most common gas sensing film in semiconductor gas sensors, but deposited by ALD for the first time in a microhotplate process (Publication **VI**).

In a typical fabrication process, the microhotplate platform is first processed to completion, including release of the hotplate, as shown in Figure 5.1, left (a–b). The sensing film is subsequently deposited by thick film methods such as screen printing or drop coating (c). In the *Lakana* process (Figure 5.1, right), SnO_2 was deposited by ALD (b), and the deposited film was processed as a standard thin film material like all others, changing the fabrication process significantly: The film was patterned as thin films usually are, by lithography and wet etching (c), and bulk etching of the MHP was performed last (d). This makes fabrication more straightforward, as all processing is done by standard wafer-scale microfabrication methods on a robust, unetched wafer.

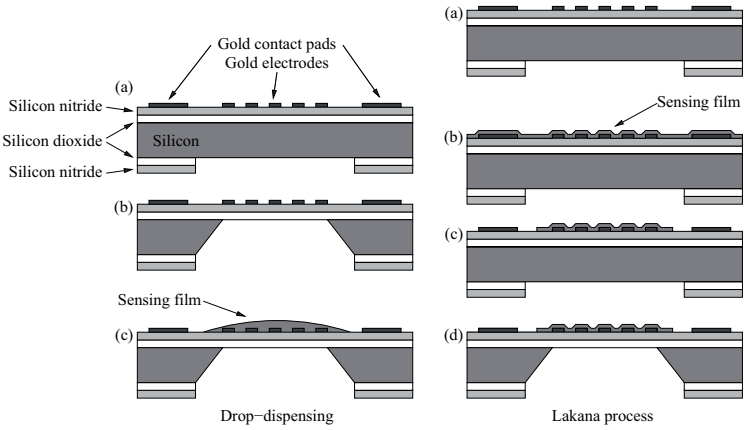

Figure 5.1: A conventional MHP process with drop-dispensing of the SnO_2 sensing film (*left*), and the *Lakana* process with ALD SnO_2 (*right*).

The MHP structure itself was made using available materials and techniques, which is convenient in the device prototyping stage, although the chosen process ultimately resulted in reduced device lifetime, requiring different process options for production devices. A detailed process description is provided in Appendix B.

5.1 Semiconductor gas sensors

Gas sensors can utilize many different principles of detection. Examples include calorimetric sensors or *pellistors* which detect the energy output of burning combustible gases on a catalytic surface, electrochemical gas cells which amperometrically detect an electrochemical reaction with the gas species (much like in a fuel cell), mass sensitive sensors which detect adsorbed molecules *e.g.* with a quartz crystal microbalance or a surface acoustic wave sensor, and various optical detection methods. [46, 178, 179]

Semiconductor gas sensors are relatively simple devices in comparison. They are based on the change of resistivity of a semiconducting metal oxide material such as WO_3, TiO_2 or SnO_2 when exposed to various gases. Especially the latter is widely used and much studied, not only as a gas-sensitive material, but also as a transparent electrical conductor, an oxidation catalyst, and in novel nanostructured materials [180]. A wide variety of other metal oxides have also been investigated as gas sensing materials [181]. The underlying mechanism is relatively simple: When heated to a high temperature, typically between 200–500°C [182], oxygen adsorbed on the surface of the nanocrystalline metal oxide grains becomes ionized, forming O_2^-, O^- or O^{2-}. The electric charge of the oxygen ions creates potential barriers at grain boundaries in the *n*-type semiconducting film (Figure 5.2, left), much in the same way as gate charge does in a MOSFET. Charge carriers must overcome this barrier in order for current to flow across the grain boundary. When exposed to reducing gases such as carbon monoxide, hydrogen, methane or solvent vapors, the adsorbed oxygen ions react with the gas, decreasing their concentration on the grain surfaces. This lowers the potential barriers (Figure 5.2, right), consequently decreasing the resistance of the film. Oxidizing gases such as NO_2 have an opposite effect. [46, 179, 182] Since the grain surface is a determining factor in gas sensitivity, the grain size and morphology in the film have a great effect. [183, 184]

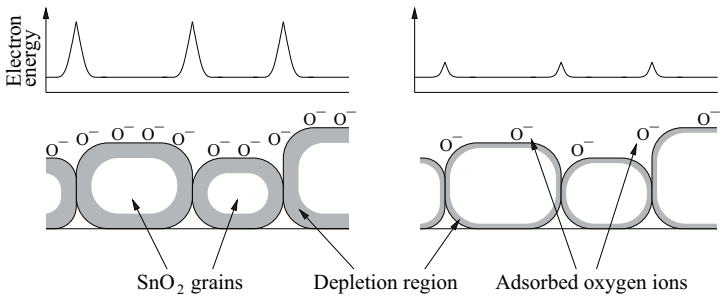

Figure 5.2: Principle of operation of a semiconductor gas sensor: Adsorbed oxygen ions create potential barriers at grain boundaries (*left*), increasing the resistance of the film. A reducing gas consumes oxygen ions (*right*), lowering the potential barriers, leading to decreased resistance.

The conductance response of MOS gas sensors to analyte gases is commonly of the form:

$$G = \frac{1}{R} = G_0 + A\, p_{\text{gas}}^{\beta}$$

where p_{gas} is the partial pressure of the analyte gas, and G_0, A and β depend on the sensor and analyte gas. For combustible gases, $\beta \approx 0.5 \ldots 1$, whereas for an oxidizing gas like oxygen, $\beta \approx -0.25 \ldots -0.55$. [46]

The sensitivity S of a sensor can either be defined as the change in its resistance when exposed to a partial pressure p_{gas} of analyte gas:

$$S = \frac{\Delta R}{p_{\text{gas}}}$$

or as the ratio of conductance in a specified concentration of analyte gas to that in pure (often synthetic) air [179]:[†]

$$S = \frac{G_{\text{gas}}}{G_{\text{air}}} = \frac{R_{\text{air}}}{R_{\text{gas}}}$$

Since the gas sensor's response is basically towards the reducing or oxidizing character of gases, there cannot be much selectivity between different reducing or oxidizing gas species. Selectivity can be improved by selection of the sensing film material [181], doping the film with sensitizing catalyst materials [46] (which can also be used to improve sensitivity and to lower the required operating temperature), optimizing the operating temperature of the sensor [179], or optimizing the morphology of the sensing film [184]. In a complete gas sensing system, selectivity can further be improved by first filtering out interfering gases, by using an array of differently tailored sensors with known selectivities [184], or by observing the transient response of a sensor, rather than its eventual steady-state resistance [185, 186].

The sensing layer itself can be made in a multitude of ways. Most commonly, nanocrystalline metal oxide powders are made by milling, sol-gel methods or spray pyrolysis, and mixed with suitable binder materials for screen-printing or drop-coating onto sensor devices. Sintering subsequently forms a porous, high-surface area thick film [46]. In the more fragile MHP devices, thinner films are required, which have been produced by sputtering [187, 188], CVD [189], laser ablation [190] and sol-gel methods [49]. Localized thermal CVD or sol-gel deposition by enhanced evaporation on the device have been effected by heating the MHP with its own heaters [184], and the use of photopatternable spin-on metal-organic SnO_2 coatings has also been published [191].

To minimize power consumption of the device, the heated sensor element must be thermally insulated from the substrate. Thick silicon dioxide [192] or porous

[†]It is somewhat misleading to call this ratio *sensitivity*, as it is not formulated *per concentration of the analyte*. Instead, it is common practice to express this "sensitivity" graphically, plotted as a function of p_{gas}. Intuitively, sensitivity should be the *slope* of that plot.

silicon [193] can be used for thermal insulation in gas sensors and other heated microdevices, but various microhotplate designs are more efficient. These can be made either as *closed* membranes, *i.e.* membranes that are not punctured, and are released from the wafer backside, or *suspended* membranes, which are released by etching and undercutting silicon from the front side, through holes patterned in the membrane film [194]. The two types of membranes are shown in Figure 5.3.

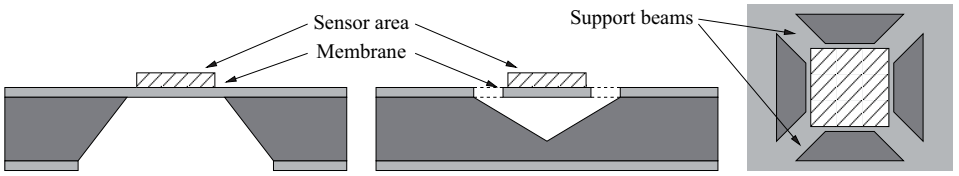

Figure 5.3: A closed membrane etched from the backside (*left*) and a suspended membrane etched from the front side (*middle*). The latter is shown also from above (*right*).

5.2 "Lakana" microhotplate structure

The microhotplate of the *Lakana* device is fabricated on a (100) silicon substrate and released by backside etching of the silicon in potassium hydroxide (KOH) solution, *i.e.* a closed membrane is used. This way the entire wafer front side can easily be protected from the KOH solution during bulk etching, thus protecting the SnO_2 sensing film which has *already been deposited* at this stage. The closed membrane is also more resistant to the water jets present in the wafer dicing process, which is done after bulk etching of the membrane.[†] The fabrication process is summarized as follows (details are in Appendix B):

- Oxidation and Si_3N_4 LPCVD for the membrane
- Sputtering and patterning of tungsten heater resistors
- PECVD and annealing of intermetal dielectric
- Contact hole etching in dielectric
- Patterning of backside Si_3N_4 and SiO_2
- Sputtering and patterning of gold sensor electrodes
- SnO_2 sensing film deposition and patterning
- Backside bulk etching, dicing and packaging

For a testing and development device, materials and methods readily available at the Micronova [103] fab had to be used. The hotplate membrane is, as usual, a stack

[†]Photopatternable ProTEK® material [71], which has since become commercially available, could make a suspended membrane design equally convenient to fabricate. Dicing, however, might remain problematic.

of thermal oxide and LPCVD deposited silicon nitride. The buried metallizations, however, are made of tungsten, and the various metallizations are separated from each other by PECVD deposited silicon dioxide.

The tungsten heater resistor is deposited by sputtering and patterned by dry etching in a SF_6 plasma. A second resistor is patterned in the same metallization layer, meandering between the lines of the heater resistor, to act as a resistive temperature sensing element. To improve the stability of the tungsten film, tungsten nitride is deposited above and below these resistors. The whole $WN_x/W/WN_x$ stack is easily deposited in a single process step by reactive sputtering, *i.e.* by introducing nitrogen into the sputter's chamber at the beginning and end of the deposition, while the tungsten film itself is sputtered with pure argon. In the etching step, the same plasma chemistry etches tungsten nitride as well as tungsten.

The silicon dioxide dielectric was deposited using a standard PECVD process at 300°C, but it soon became apparent that outgassing of residual hydrogen or other gaseous species from the film caused delamination of subsequent metal layers during the ALD deposition of the SnO_2 sensing layer. Figure 5.4, left, shows an optical microscope image of this occurring on an intermediate electrode layer[†] over the heater resistors. There is no damage evident in the surrounding dielectric, where outgassing species can diffuse out of the PECVD SiO_2 film. Under the electrode metallization, however, bubbles formed, as shown in the schematic cross-section on the right. Therefore the dielectric film was annealed immediately after deposition at a temperature of 500°C, which would not be exceeded during further processing nor operation of the component.

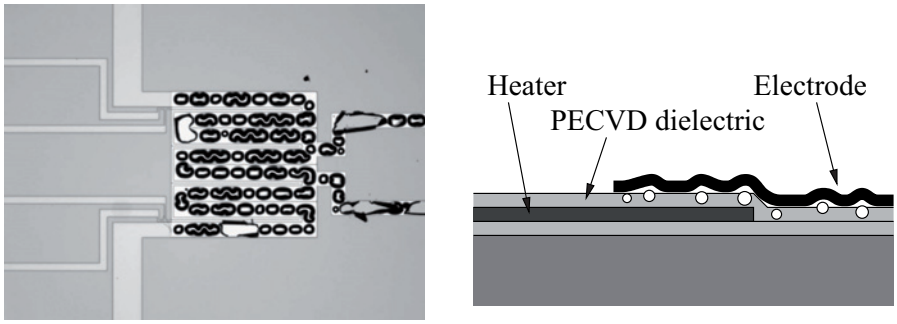

Figure 5.4: Outgassing of PECVD SiO_2 causes delamination of metallization: The metal lines coming from the left are underlying heater and thermometer wires. The lines leading to the right are the overlying electrode metallization. The latter suffers delamination as the PECVD intermetal dielectric outgasses during high-temperature processing.

[†]In some batches of devices, an extra biasing electrode was fabricated between the heater and sensor electrode layers (process steps 11–16 in Appendix B), intended to provide an equipotential plane *e.g.* if a future device were to utilize the Seebeck effect [195]. This intermediate metallization was ultimately not used in the devices, and was omitted to alleviate the outgassing issues.

Various geometries of sensing electrodes were tested, including interdigitated comb electrodes of various linewidths and densities, as well as a "multi-sensor" arrangement containing four individual electrodes at various distances from each other. These were all fabricated in gold, which does not corrode during the SnO_2 deposition process where HCl is produced, nor in the aggressive SnO_2 etchant solution, and which is an easy material to bond electrical contact wires to. The sputtered gold film was patterned by wet etching, using diluted Aqua Regia ($HCl + HNO_3$) and a standard photoresist mask. To improve adhesion, a thin film of titanium or titanium-tungsten alloy was sputtered underneath the gold film, and this was wet etched in dilute hydrogen peroxide.

5.3 Sensing film processing

Instead of depositing the sensing film on an otherwise finished MHP component as is commonly done [194], it was deposited like any other film in the fabrication process, on the whole unetched wafer. At this time the wafer is still robust, and able to withstand a variety of deposition and patterning processes without risk of breakage.

The tin dioxide sensing film was deposited by our coworkers. The main deposition method was ALD, using a $SnCl_4/H_2O$ process [196]. Reactively sputtered SnO_2 films were also tested, produced by sputtering tin in an oxygen-containing atmosphere, followed by oxygen annealing to improve the stoichiometry of the film. As these deposition processes were done on the whole wafer, the tin dioxide had to be patterned to expose the contact pad areas of the chip. In the ALD variant, this was done by wet etching, using a chromic acid solution activated by zinc powder [197]. This etchant is very aggressive also towards the photoresist mask, which was significantly damaged, but did nevertheless survive the short etch process, albeit with significant broadening of the etched structures. This was not a problem, however, as the contact pads were sufficiently far from the active sensor area. Reactive sputtering, on the other hand, is a low-temperature process, and lift-off was used to pattern the SnO_2 film prior to annealing.

The *Lakana* device is set apart from other microhotplate gas sensors by how the sensing film is processed. In both the ALD and reactive sputtering variants, the *Lakana* process uses only wafer-scale or batch-scale processes and standard semiconductor fabrication techniques throughout. In contrast, in most other fabrication processes the sensing film is deposited last, on the otherwise complete device. Regardless of the deposition method, this involves more handling of the fragile bulk-etched wafers, and possibly much chip-scale processing as well.

5.4 Release of the microhotplate

KOH etching of the silicon wafer backside was the last wafer-scale process performed. Since KOH is a rather aggressive etchant, special precautions must be taken to protect the wafer's front side. A newly developed spin-on etch-protective coating called ProTEK® by Brewer Science Inc. was used for this purpose. While the coating itself was not attacked by the etchant to any visible degree, its adhesion to the substrate slowly degraded during the long etching process, and the film began to peel away, beginning at the wafer edges.† Therefore a special wafer holder was used, which exposed only one side of the wafer to the etchant. The ProTEK® film was still used as additional protection, in case a single device broke during etching and allowed etchant to leak to the wafer front surface. The ProTEK® film was left on the wafer also for the duration of dicing to individual chips, which subjects the device to water jets and particle contamination. With the relatively thick ProTEK® layer in place, the devices survived dicing without breakage. Following dicing, the ProTEK® layer was removed using a sequence of solvents.

MHP devices were made both on a simple SiO_2/Si_3N_4 dual layer membrane by a single KOH etching step, as was shown in Figure 2.6, left, on page 39, and on a membrane with a silicon island underneath as in Figure 2.6, middle, both to provide additional mechanical support and to help maintain uniform temperature throughout the sensor. With the unoptimized etchant, the shape and thickness of the silicon islands were not very controllable, and in many cases they only concentrated film stresses causing breakage of the MHP membrane. Also the timing of the second etching step was very critical, requiring constant monitoring at the end of the nearly 3-hour etch process. While the boron etch-stop process shown in Figure 2.6, right does require multiple extra processing steps in the front-end, the improved dimensional control of the island and the simplification of the bulk etching process would make that alternative preferable for further development. The thickness of the silicon island would, however, be limited by the diffusion depth of the dopant.

Another alternative release method that was not tested is plasma etching by cryogenic ICP RIE. The thick thermal oxide layer on the wafer backside is quite sufficient as an etch mask, and the oxide at the bottom of the MHP membrane would serve well as an etch stop. This method would not enable any island structures by boron etch-stop, although two-stage timed etching would be possible using suitable mask materials. Plasma etching would, however, reduce the size of each sensor chip, as the through-etched sidewall profiles are vertical instead of slanted. This would enable more devices to be produced per wafer.

†Newer versions of ProTEK® are claimed to have improved adhesion and to resist such peeling in a through-wafer etching process.

5.5 Results

The successful application of ALD in the fabrication of MHP gas sensors was demonstrated, as well as a novel fabrication process where the SnO_2 sensing layer was deposited and patterned before release of the microhotplate. Also, unconventional tungsten heater metallizations and PECVD SiO_2 intermetal dielectrics were demonstrated to work well in the short term for prototyping and testing of MHP gas sensors.

In the long term, the tungsten heaters were not, however, very stable. Oxidation of the heater resistors was evident after approximately two weeks of continuous operation, possibly initiated from point defects at the line edges. However, the ALD SnO_2 technology and its associated process flow does not affect the hotplate structure and processing *per se*, and a trial batch of *Lakana* devices, using conventional platinum metallizations and Si_3N_4 dielectrics, was processed at another fab to demonstrate this. The required heating power for 300°C operation of the hotplate (with tungsten heaters) was 80–180 mW, depending on device variant, which is comparable to other reported MHP devices [194], and the operating temperature stabilized within seconds.

Figure 5.5 shows the sensor's response to three analyte gases at two concentrations each. The response of the device was fast, as seen from the risetimes to 50% of maximum shown in Table 5.1. Drift in the output signal was low, and further decreased with time. ALD SnO_2 is therefore seen as a viable and stable material for MHP gas sensor applications. The sensitivity of the devices was, however, quite low in the current generation of devices. But since no sensitizing dopants had been added to the SnO_2 film, this was expected, and much higher sensitivities should be possible to obtain with the same basic design. The sensitizers could either be deposited over the SnO_2 film by evaporation or sputtering, or they could be incorporated within the film itself during deposition. The ALD process is ideally suited for the latter, as individual pulses of various dopant precursors can be introduced between the repeating $SnCl_4$ and H_2O pulses to tailor the film composition with great accuracy and reproducibility.

Gas	Concentration	S	$t_{50\%}$ (s)
Ethanol	100 ppm	1.51	3.4
	500 ppm	1.64	2.3
Acetone	100 ppm	1.23	8.1
	500 ppm	1.38	4.2
Acrylonitrile	20 ppm	1.008	3.0
	100 ppm	1.035	5.2

Table 5.1: Sensitivities and response times of *Lakana* gas sensor devices to various concentrations of analyte gases

Temperature uniformity in the sensing film can conceivably have a major impact on device performance in terms of sensitivity, selectivity and response time. Whether a

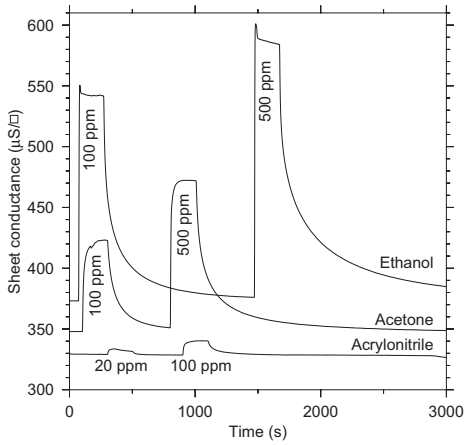

Figure 5.5: Response of the *Lakana* sensor to various gases. (For clarity, the curves for acetone and ethanol are shifted up by 20 and 40 µS/□, respectively.)

silicon island under the MHP actually makes a noticeable improvement ought to be investigated more thoroughly with well-defined boron etch-stop islands. In pulsed operation, *e.g.* to reduce battery consumption in a portable instrument, the rigidity provided by the island may also improve device lifetime, as flexing of the MHP during heating and cooling is minimized.

6 Conclusions and outlook

Hot electron-induced electrochemiluminescence

Hot electron-induced electrochemiluminescence is a versatile method for bioassays, with many advantages. The HECL chips designed and tested in this work provide a practical approach to using HECL methods in routine analysis. High sensitivity to the model Tb(III) chelate was demonstrated with small sample volumes, on a completely disposable chip that requires no washing of parts between analyses, and minimal assembly for each measurement. The time required per measurement was thus reduced to a fraction of that needed with conventional plain silicon or aluminum electrodes and separate counter electrode wires.

The sample containment schemes that were investigated are complementary: Neither one is an obvious all-round winner for all conceivable applications. Hydrophobic confinement is simple to fabricate and does not degrade in storage, but does require a modicum of laboratory routine to use. With an adjustable micropipette, uniform droplets can be formed on the hydrophobic chip, resulting in good reproducibility. Due to its open structure, modification of the electrode surface with antibodies should be relatively easy, and work is ongoing to utilize these devices in bioassays. The PDMS capillary-filling device, on the other hand, would be more convenient for point-of-care use, as uniform sample volumes can be obtained without much skill or equipment.

Unfortunately, the lifetime of the hydrophilic PDMS surface is limited, and although restoration of surface hydrophilicity in an enclosed PDMS fluidic system after storage was demonstrated, this is inconvenient or impossible in a point-of-care application. Therefore, alternative materials and bonding methods ought to be investigated for the fluidic part of the chip. In fact, the PDMS sample chambers were first envisioned only as a proof-of-concept for the use of HECL detection in microfluidic systems, where PDMS, despite its problems, remains widely used. While the simple PDMS devices were demonstrated to work with good sensitivity, an actual microfluidic system combining sample pretreatment, labeling, binding, flushing and detection, remains still to be implemented.

Work is already ongoing to use polymeric substrates for the HECL chips. This approach may eventually yield viable solutions also for fabricating the on-chip fluidic system *e.g.* by hot embossing or mold extrusion. For a low-cost device, use of a cheap plastic substrate is only a first step. Since the linewidth requirements of these devices are very relaxed, patterning of the electrode metal films could be effected by evaporation or sputtering through a shadow mask. Alignment could conceivably be done by purely mechanical means, using pins in a substrate holder and holes in the polymeric substrates and shadow masks to align the two with sufficient precision. If a low-temperature ALD process is used, the Al_2O_3 film could be patterned by lift-off. If the lift-off resist were applied by screen printing, the entire fabrication process could be accomplished without any expensive lithography steps.

Since HECL occurs only in a relatively narrow thickness range of tunneling dielectrics, and the optimal thickness is in the vicinity of only 4 nm, special considerations and precautions are needed in both the fabrication and characterization of the films. Deposition processes therefore had to be optimized to be reproducible, or indeed possible, in this ultrathin regime. A variety of common microelectronic materials were tested for HECL electrode application in this work, but an infinitely greater variety exists that can be deposited *e.g.* by ALD. What precisely determines a tunnel dielectric's performance in HECL is not yet fully understood, so other materials and process parameters should be further investigated in the hope of shedding some light on the underlying processes. Thence, a search for the ultimate tunnel dielectric could be undertaken.

To be truly useful, the entire HECL measurement setup should be miniaturized. A prototype instrument might utilize a high-sensitivity solid-state detector (*e.g.* an avalanche photodiode), and a suitable microcontroller for data acquisition and processing. Controllers such as the Philips/NXP LPC 21xx series, the Microchip PIC 16 and PIC 18 series, and many others, offer on-chip analog-to-digital converters for digitizing the HECL signal, or they can interfaced to an external converter for better speed and resolution. They also offer various amounts of non-volatile memory that can be used to store calibration data and results, as well as the necessary bus lines for interfacing to a keypad and display for independent use, or to a computer if desired. The coulostatic pulse generator [133] is simple in design, and easily adapted to microprocessor control. If a cascade were used to generate the high voltages required for the pulse generator and photodiode biasing, the instrument could be entirely battery powered. A prototype instrument should fit in a case the size of a thick paperback novel, and with some optimization, a complete HECL system might not be much larger than a modern cellular phone.

ALD films in semiconductor gas sensors

The application of ALD to deposit the SnO_2 sensing film in a microhotplate gas sensor device was successfully demonstrated. Fast response time to gases and low drift in the output signal demonstrate the capabilities of ALD in the deposition of the sensing film. For research purposes, a microhotplate fabrication process using available materials and methods (tungsten heater metallizations and PECVD-deposited intermetal dielectrics) was presented, and the new etch-protective material ProTEK® was utilized in bulk etching and dicing. The photopatternable variant of ProTEK®, which has since become commercially available, could be employed to further improve the fabrication process. For production devices, conventional platinum heaters and silicon nitride dielectrics would be preferable to ensure long-term stability of the microhotplate, but the stability of the ALD SnO_2 sensing film itself was excellent within the limits tested.

Whereas in conventional MHP gas sensors the sensing film is deposited last onto the completed MHP platform, in the *Lakana* process the SnO_2 film was deposited

and patterned earlier in the fabrication process. It was therefore used like any other material in semiconductor device fabrication, thus more tightly integrating the sensing film deposition into the fabrication process. This is possible since the ALD-deposited SnO_2 is denser and more robust than a conventional porous thick-film material, and can thus withstand standard processing methods.

The high density of the ALD-deposited SnO_2 film may in part decrease the sensitivity of the sensor. However, only undoped SnO_2 films have thus far been tested in the *Lakana* devices. Therefore, doping of the film is expected to greatly improve the sensitivity. Doping could be done *ex situ* by evaporation onto the finished device, or dopant materials could be incorporated *in situ* in the ALD process. The potential offered by ALD for the production of a variety of gas-sensitive materials or highly tailored sensing film stacks also remains to be investigated.

References

[1] K. E. Petersen, Silicon as a mechanical material, *Proc. IEEE* **70** (1982) 420–457.

[2] J. B. Angell, S. C. Terry, P. W. Barth, Silicon micromechanical devices, *Sci. Am.* **248** (1983) 36–47.

[3] S. A. Campbell, *The Science and Engineering of Microelectronic Fabrication*, Oxford University Press, New York, 2001.

[4] J.-P. Raskin, F. Iker, N. André, B. Olbrechts, T. Pardoen, D. Flandre, Bulk and surface micromachined MEMS in thin film SOI technology, *Electrochim. Acta* **52** (2007) 2850–2861.

[5] W. Noell, P.-A. Clerc, L. Dellmann, B. Guldimann, H.-P. Herzig, O. Manzardo, C. R. Marxer, K. J. Weible, R. Dändliker, N. de Rooij, Applications of SOI-based optical MEMS, *IEEE J. Sel. Topics. Quantum Electron.* **8** (2002) 148–154.

[6] J. S. Mellors, V. Gorbounov, R. S. Ramsey, J. M. Ramsey, Fully integrated glass microfluidic device for performing high-efficiency capillary electrophoresis and electrospray ionizaton mass spectrometry, *Anal. Chem.* **80** (2008) 6881–6887.

[7] V. Saarela, M. Haapala, R. Kostiainen, T. Kotiaho, S. Franssila, Glass microfabricated nebulizer chip for mass spectrometry, *Lab Chip* **7** (2007) 644–646.

[8] K. M. Knowles, A. T. J. van Helvoort, Anodic bonding, *Int. Mater. Rev.* **51** (2006) 273–311.

[9] M. A. Meador, Recent advances in the development of processable high-temperature polymers, *Annu. Rev. Mater. Sci.* **28** (1998) 599–630.

[10] E. I. DuPont de Nemours and Co., Wilmington, DE., *Summary of Properties for Kapton® Polyimide Films*, `http://www2.dupont.com/Kapton/en_US/assets/downloads/pdf/Gen_Specs.pdf`.

[11] H. Becker, C. Gärtner, Polymer microfabrication technologies for microfluidic systems, *Anal. Bioanal. Chem.* **390** (2008) 89–111.

[12] P. Abgrall, A.-M. Gué, Lab-on-chip technologies: Making a microfluidic network and coupling it into a complete microsystem — A review, *J. Micromech. Microeng.* **17** (2007) R15–R49.

[13] N. Inagaki, S. Tasaka, T. Umehara, Effects of surface modification by remote hydrogen plasma on adhesion in poly(tetrafluoroethylene)/copper composites, *J. Appl. Polym. Sci.* **71** (1999) 2191–2200.

[14] S. Wu, E. T. Kang, K. G. Neoh, H. S. Han, K. L. Tan, Surface modification of poly(tetrafluoroethylene) films by graft copolymerization for adhesion

improvement with evaporated copper, *Marcomolecules* **32** (1999) 186–193.

[15] N. Inagaki, S. Tasaka, M. Masumoto, Improved adhesion between kapton film and copper metal by plasma graft polymerization of vinylimidazole, *Macromolecules* **292** (1996) 1642–1648.

[16] Y.-S. Lin, H.-M. Liu, Enhanced adhesion of plasma-sputtered copper films on polyimide substrates by oxygen glow discharge for microelectronics, *Thin Solid Films* **516** (2008) 1773–1780.

[17] R. J. Good, Contact angle, wetting and adhesion: A critical review, *J. Adhesion Sci. Technol.* **6** (1992) 1269–1302.

[18] V. Jokinen, S. Franssila, Capillarity in microfluidic channels with hydrophilic and hydrophobic walls, *Microfluid. Nanofluid.* **5** (2008) 443–448.

[19] E. M. Liston, L. Martinu, M. R. Wertheimer, Plasma surface modification of polymers for improved adhesion: A critical review, *J. Adhesion Sci. Technol.* **7** (1993) 1091–1127.

[20] W. A. MacDonald, M. K. Looney, D. MacKerron, R. Eveson, R. Adam, K. Hashimoto, K. Rakos, Latest advances in substrates for flexible electronics, *J. Soc. Inf. Disp.* **15** (2007) 1075–1083.

[21] E. A. Irene, *Surfaces, Interfaces, and Thin Films for Microelectronics*, Wiley-Interscience, Hoboken, NJ, 2008.

[22] B. E. Deal, A. S. Grove, General relationship for the thermal oxidation of silicon, *J. Appl. Phys.* **36** (1965) 3770–3778.

[23] S. Dimitrijev, H. B. Harrison, Modeling the growth of thin silicon oxide films on silicon, *J. Appl. Phys.* **80** (1996) 2467–2470.

[24] S. M. Hu, Thermal oxidation of silicon: Chemisorption and linear rate constant, *J. Appl. Phys.* **55** (1984) 4095–4105.

[25] H. Z. Massoud, J. D. Plummer, E. A. Irene, Thermal oxidation of silicon in dry oxygen growth-rate enhancement in the thin regime, *J. Electrochem. Soc.* **132** (1985) 2685–2693.

[26] E. P. Gusev, H. C. Lu, T. Gustafsson, E. Garfunkel, The initial oxidation of silicon: New ion scattering results in the ultra-thin regime, *Appl. Surf. Sci.* **104–105** (1996) 329–334.

[27] J. D. Plummer, M. D. Deal, P. B. Griffin, *Silicon VLSI Technology*, Prentice Hall, Upper Saddle River, NJ, 2000.

[28] T. Suntola, J. Hyvärinen, Atomic layer epitaxy, *Ann. Rev. Mater. Sci.* **15** (1985) 177–195.

[29] S. M. George, Atomic layer deposition: An overview, *Chem. Rev.* **110** (2010) 111–131.

[30] R. L. Puurunen, Surface chemistry of atomic layer deposition: A case study

for the trimethylaluminum/water process, *J. Appl. Phys., Applied Physics Reviews* **97** (2005) 121301.1–121301.52.

[31] M. D. Groner, F. H. Fabreguette, J. W. Elam, S. M. George, Low-temperature Al_2O_3 atomic layer deposition, *Chem. Mater.* **16** (2004) 639–645.

[32] F. H. Fabreguette, R. A. Wind, S. M. George, Ultrahigh X-ray reflectivity from W/Al_2O_3 multilayers fabricated using atomic layer deposition, *Appl. Phys. Lett.* **88** (2006) 013116.1–013116.3.

[33] D. A. Glocker, S. I. Shah (editors), *Handbook of Thin Film Process Technology*, Institute of Physics Publishing, Bristol, 1995.

[34] H. Nagayama, H. Honda, H. Kawahara, A new process for silica coating, *J. Electrochem. Soc.* **135** (1988) 2013–2016.

[35] J.-S. Chou, S.-C. Lee, The initial growth mechanism of silicon oxide by liquid-phase deposition, *J. Electrochem. Soc.* **141** (1994) 3214–3218.

[36] A. J. Niskanen, *Liquid Phase Deposition of Silicon Dioxide Thin Films*, Master's thesis, Helsinki University of Technology, 2002.

[37] S. Kulmala, K. Haapakka, Mechanism of electrogenerated luminescence of terbium(III)-{2,6-bis[N,N-bis(carboxymethyl)aminomethyl]-4-benzoylphenol} chelate at an oxide-covered aluminium electrode, *J. Alloys Compd.* **225** (1995) 502–506.

[38] S. Kulmala, T. Ala-Kleme, L. Heikkilä, L. Väre, Energetic electrochemiluminescence of (9-fluorenyl)methanol induced by injection of hot electrons into aqueous electrolyte solution, *J. Chem. Soc., Faraday Trans.* **93** (1997) 3107–3113.

[39] S. Kulmala, T. Ala-Kleme, H. Joela, A. Kulmala, Hot electron injection into aqueous electrolyte solution from thin insulating film-coated electrodes, *J. Radioanal. Nucl. Chem.* **232** (1998) 91–95.

[40] J. W. Diggle, T. C. Downie, C. W. Goulding, Anodic oxide films on aluminum, *Chem. Rev.* **69** (1969) 365–405.

[41] J. A. Bardwell, K. B. Clark, D. F. Mitchell, D. A. Bisaillion, G. I. Sproule, B. MacDougall, M. J. Graham, Growth and characterization of room temperature anodic SiO_2 films, *J. Electrochem. Soc.* **140** (1993) 2135–2138.

[42] J. A. Bardwell, N. Draper, P. Schmuki, Growth and characterization of anodic oxides on Si(100) formed in 0.1 M hydrochloric acid, *J. Appl. Phys* **79** (1996) 8761–8769.

[43] S. Taylor, J. F. Zhang, W. Eccleston, A review of the plasma oxidation of silicon and its applications, *Semicond. Sci. Technol.* **8** (1993) 1426–1433.

[44] T. Majamaa, *Ultrahigh Vacuum Plasma oxidation in the Fabrication of Ultrathin Silicon Dioxide Films*, Ph.D. thesis, Helsinki University of Technology,

2000.

[45] M. Akizuki, J. Matsuo, S. Ogasawara, M. Harada, A. Doi, I. Yamada, Low-temperature oxidation of silicon by O_2 cluster ion beams, *Jpn. J. Appl. Phys.* **35** (1996) 1450–1453.

[46] C. O. Park, S. A. Akbar, Ceramics for chemical sensing, *J. Mat. Sci.* **38** (2003) 4611–4637.

[47] G. C. Cheek, R. P. Mertens, R. van Overstraeten, L. Frisson, Thick-film metallization for solar cell applications, *IEEE Trans. Electron Devices* **ED-31** (1984) 602–609.

[48] N. O. Savage, S. A. Akbar, P. K. Dutta, Titanium dioxide based high temperature carbon monoxide selective sensor, *Sens. Actuators, B.* **72** (2001) 239–248.

[49] O. K. Varghese, L. K. Malhotra, G. L. Sharma, High ethanol sensitivity in sol-gel derived SnO_2 thin films, *Sens. Actuators, B* **55** (1999) 161–165.

[50] T. Sahm, L. Mädler, A. Gurlo, N. Barsan, S. E. Pratsinis, U. Weimar, Flame spray synthesis of tin dioxide nanoparticles for gas sensing, *Sens. Actuators, B* **98** (2004) 148–153.

[51] K. Y. Lee, N. LaBianca, S. A. Rishton, S. Zolgharnain, J. D. Gelorme, J. Shaw, T. H.-P. Chang, Micromachining applications of a high resolution ultrathick photoresist, *J. Vac. Sci. Technol. B* **13** (1995) 3012–3016.

[52] A. del Campo, C. Greiner, SU-8: A photoresist for high-aspect-ratio and 3D submicron lithography, *J. Micromech. Microeng.* **17**.

[53] H. Klose, R. Sigush, W. Arden, Image reversal of positive photoresist: Characterization and modeling, *IEEE Trans. Electron Devices* **ED-32** (1985) 1654–1661.

[54] Clariant GmbH, Wiesbaden, *Product datasheet, AZ5214 E Image Reversal Photoresist.*

[55] MicroChem Corp., Newton, MA., *LOR*$^{\text{TM}}$ *Lift-Off Resists*, `http://www.microchem.com/products/pdf/lor_data_sheet.pdf`.

[56] D. J. Elliott, *Integrated Circuit Fabrication Technology*, McGraw-Hill, New York, 1982.

[57] W. Kern, D. A. Puotinen, Cleaning solutions based on hydrogen peroxide for use in silicon semiconductor technology, *RCA Rev.* **31** (1970) 187–206.

[58] W. Kern (editor), *Handbook of Semiconductor Wafer Cleaning Technology*, Noyes Publications, Westwood, NJ, 1993.

[59] T. Hattori (editor), *Ultraclean Surface Processing of Silicon Wafers*, Springer, Berlin, 1998.

[60] J. Ruzyllo, T. Hattori, R. E. Novak, P. Mertens, P. Besson, Evolution of

silicon cleaning technology over the last twenty years, *ECS Trans.* **11** (2007) 3–7.

[61] G. L. Weibel, C. K. Ober, An overview of supercritical CO_2 applications in microelectronics processing, *Microelectron. Eng.* **65** (2003) 145–152.

[62] W. I. Jang, C. A. Choi, M. L. Lee, C. H. Jun, Y. T. Kim, Fabrication of MEMS devices by using anhydrous HF gas-phase etching with alcoholic vapor, *J. Micromech. Microeng.* **12** (2002) 297–306.

[63] H. V. Jansen, M. J. de Boer, S. Unnikrishnan, M. C. Louwerse, M. C. Elwenspoek, Black silicon method X: A review on high speed and selective plasma etching of silicon with profile control: An in-depth comparison between Bosch and cryostat DRIE processes as a roadmap to next generation equipment, *J. Micromach. Microeng.* **19** (2009) 1–41.

[64] M. J. Walker, Comparison of Bosch and cryogenic processes for patterning high aspect ratio features in silicon, *Proc. SPIE* **4407** (2001) 89–99.

[65] L. Sainiemi, *Cryogenic Deep Reactive Ion Etching of Silicon Micro and Nanostructures*, Ph.D. thesis, Helsinki University of Technology, 2009.

[66] H. Seidel, L. Csepregi, A. Heuberger, H. Baumgärtel, Anisotropic etching of crystalline silicon in alkaline solutions, I: Orientation dependence and behavior of passivation layers, *J. Electrochem. Soc.* **137** (1990) 3612–3626.

[67] H. Seidel, L. Csepregi, A. Heuberger, H. Baumgärtel, Anisotropic etching of crystalline silicon in alkaline solutions, II: Influence of dopants, *J. Electrochem. Soc.* **137** (1990) 3626–3632.

[68] D. Briand, A. Krauss, B. van der Schoot, U. Weimar, N. Bârsan, W. Göpel, N. F. de Rooij, Design and fabrication of high-temperature micro-hotplates for drop-coated gas sensors, *Sens. Actuators, B* **68** (2000) 223–233.

[69] K. Ruben, T. Flaim, C. Li, Polymeric protective coatings for MEMS wet-etch processes, *Proc. SPIE* **5342** (2004) 212–220.

[70] G. Canavese, S. L. Marasso, M. Quaglio, M. Cocuzza, C. Ricciardi, C. F. Pirri, Polymeric mask protection for alternative KOH silicon wet etching, *J. Micromech. Microeng.* **17** (2007) 1387–1393.

[71] J. Dalvi-Malhotra, X. F. Zhong, C. Planje, G. Brand, K. Yess, A spin-on photosensitive polymeric etch protection mask for anisotropic wet etching of silicon, *J. Micromech. Microeng.* **18** (2008) 1–8.

[72] J. C. McDonald, D. C. Duffy, J. R. Anderson, D. T. Chiu, H. Wu, O. J. A. Schueller, G. M. Whitesides, Fabrication of microfluidic systems in poly(dimethylsiloxane), *Electrophoresis* **21** (2000) 27–40.

[73] M. A. Eddings, M. A. Johnson, B. K. Gale, Determining the optimal PDMS-PDMS bonding technique for microfluidic devices, *J. Micromech. Microeng.* **18** (2008) 1–4.

[74] K. C. Tang, E. Liao, W. L. Ong, J. D. S. Wong, A. Agarwal, R. Nagarajan, L. Yobas, Evaluation of bonding between oxygen plasma treated polydimethyl siloxane and passivated silicon, *J. Phys.: Conf. Ser.* **34** (2006) 155–161.

[75] H. Hillborg, M. Sandelin, U. W. Gedde, Hydrophobic recovery of polydimethylsiloxane after exposure to partial discharges as a function of crosslink density, *Polymer* **42** (2001) 7349–7362.

[76] D. T. Eddington, J. P. Puccinelli, D. J. Beebe, Thermal aging and reduced hydrophobic recovery of polydimethylsiloxane, *Sens. Actuators, B* **114** (2006) 170–172.

[77] C. de Menezes Atayde, I. Doi, Highly stable hydrophilic surfaces of PDMS thin layer obtained by UV radiation and oxygen plasma treatments, *Phys. Status Solidi C* **7** (2010) 189–192.

[78] B. Kim, E. T. K. Peterson, I. Papautsky, Long-term stability of plasma oxidized PDMS surfaces, in *Proceedings of the 26th Annual International Conference of the IEEE EMBS*, pp. 5013–5016, 2004.

[79] T. Murakami, S.-I. Kuroda, Z. Osawa, Dynamics of polymeric solid surfaces treated with oxygen plasma: Effect of aging media after plasma treatment, *J. Colloid Interface Sci.* **202** (1998) 37–44.

[80] F. Niklaus, G. Stemme, J.-Q. Lu, R. J. Gutmann, Adhesive wafer bonding, *J. Appl. Phys., Applied Physics Reviews — Focused Review* **99** (2006) 031101.1–031101.28.

[81] H. Wu, B. Huang, R. N. Zare, Construction of microfluidic chips using polydimethylsiloxine for adhesive bonding, *Lab Chip* **5** (2005) 1393–1398.

[82] S. Schlautmann, G. A. J. Besselink, G. R. Brabhu, R. B. M. Schasfoort, Fabrication of a microfluidic chip by UV bonding at room temperature for integration of temperature-sensitive layers, *J. Micromech. Microeng.* **13** (2003) S81–S84.

[83] V. P. Ganesh, C. Lee, Overview and emerging challenges in mechanical dicing of silicon wafers, in *8th Electronics Packaging Technology Conference*, pp. 15–21, 2006.

[84] D. L. Rode, V. R. Gaddam, J. H. Yi, Subnanometer surface roughness of DC magnetron sputtered Al films, *J. Appl. Phys.* **102** (2007) 024303.1–024303.8.

[85] D. K. Schroder, *Semiconductor Material and Device Characterization*, Wiley-Interscience, New York, 2nd edition, 1998.

[86] PLASMOS GmbH, München, *SD Series Ellipsometer Software User Manual*, 01.97 edition, 1995.

[87] J. F. Verweij, J. H. Klootwijk, Dielectric breakdown I: A review of oxide breakdown, *Microelectron. J.* **27** (1996) 611–622.

[88] C. K. O'Sullivan, G. G. Guilbault, Commercial quartz crystal microbalances — Theory and applications, *Biosens. Bioelectron.* **14** (1999) 663–670.

[89] S. Deki, Y. Aoi, Y. Asaoka, A. Kajinami, M. Mizuhata, Monitoring the growth of titanium oxide thin films by the liquid-phase deposition method with a quartz crystal microbalance, *J. Mater. Chem.* **7** (1997) 733–736.

[90] C. Yao, T. Zhu, J. Tang, R. Wu, Q. Chen, M. Chen, B. Zhang, J. Huang, W. Fu, Hybridization assay of hepatitis B virus by QCM peptide nucleic acid biosensor, *Biosens. Bioelectron.* **23** (2008) 879–885.

[91] R. Hao, D. Wang, X. Zhang, G. Zuo, H. Wei, R. Yang, Z. Zhang, Z. Cheng, Y. Guo, Z. Cui, Y. Zhou, Rapid detection of bacillus anthracis using monoclonal antibody functionalized QCM sensor, *Biosens. Bioelectron.* **24** (2009) 1330–1335.

[92] V. Holý, J. Kuběna, I. Ohlídal, X-ray reflection from rough layered systems, *Phys. Rev. B* **47** (1993) 15896–15903.

[93] J. Tiilikainen, *Novel Genetic Fitting Algorithms and Statistical Error Analysis Methods for X-Ray Reflectivitys Analysis*, Ph.D. thesis, Helsinki University of Technology, 2008.

[94] B. B. Burton, F. H. Fabreguette, S. M. George, Atomic layer deposition of MnO using bis(ethylcyclopentadienyl)manganese and H_2O, *Thin Solid Films* **517** (2009) 5658–5665.

[95] M. L. Green, A. J. Allen, J. L. Jordan-Sweet, J. Ilavsky, Annealing behavior of atomic layer deposited HfO_2 films studied by synchrotron X-ray reflectivity and grazing incidence small angle scattering, *J. Appl. Phys.* **105** (2009) 103522.1–103522.11.

[96] A. Niskanen, *Radical Enhanced Atomic Layer Deposition of Metals and Oxides*, Ph.D. thesis, University of Helsinki, 2006.

[97] P. Drude, Ueber Oberflächenschichten. I. Theil, *Annalen der Physik und Chemie* **36** (1889) 532–560, reprinted in [101].

[98] P. Drude, Ueber Oberflächenschichten. II. Theil, *Annalen der Physik und Chemie* **36** (1889) 865–897, reprinted in [101].

[99] Rayleigh, On reflexion from liquid surfaces in the neighborhood of the polarizing angle, *Philosophical Magazine* **32** (1892) 1–19, reprinted in [101].

[100] A. Rothen, Measurements of the thickness of thin films by optical means, from Rayleigh and Drude to Langmuir, and the development of the present ellipsometer, in E. Passaglia, R. R. Stromberg, J. Kruger (editors), *Symp. Proc. on Ellipsometry in the Measurement of Surfaces and Thin Films*, pp. 7–21, National Bureau of Standards Miscellaneous Publication 256, 1964, reprinted in [101].

[101] R. M. A. Azzam (editor), *Selected Papers on Ellipsometry*, volume MS 27 of

SPIE Milestone Series, SPIE Optical Engineering Press, Bellingham, WA, 1991.

[102] H. G. Tompkins, *A User's Guide to Ellipsometry*, Academic Press, Boston, MA, 1993.

[103] *Anon.*, Micronova — Center for micro and nanotechnology, `http://www.micronova.fi/`, 2010.

[104] S. Ang, S. Wilson, Rapid thermal annealed low pressure chemical-vapor-deposited SiO_2 as gate dielectric in silicon MOSFETs, *J. Electrochem. Soc.* **134** (1987) 1254–1258.

[105] G. D. Wilk, R. M. Wallace, J. M. Anthony, High-κ gate dielectrics: Current status and materials properties considerations, *J. Appl. Phys.* **89** (2001) 5243–5275.

[106] D. Misra, H. Iwai, H. Wong, High-k gate dielectrics, *Interface* **14** (2005) 30–34.

[107] Y. J. Chabal, G. S. Higashi, K. Raghavachari, Infrared spectroscopy of Si(111) and Si(100) surfaces after HF treatment: Hydrogen termination and surface morphology, *J. Vac. Sci. Technol. A* **7** (1989) 2104–2109.

[108] G. S. Higashi, Y. J. Chabal, G. W. Trucks, K. Raghavachari, Ideal hydrogen termination of the Si(111) surface, *Appl. Phys. Lett.* **56** (1990) 656–658.

[109] M. Morita, T. Ohmi, E. Hasegawa, M. Kawakami, K. Suma, Control factor of native oxide growth on silicon in air or in ultrapure water, *Appl. Phys. Lett.* **55** (1989) 562–564.

[110] H. Kahn, C. Deeb, I. Chasiotis, A. H. Heuer, Anodic oxidation during MEMS processing of silicon and polysilicon: Native oxides can be thicker than you think, *J. Microelectromech. Syst.* **14**.

[111] K. Grigoras, S. Franssila, V.-M. Airaksinen, Investigation of sub-nm ALD aluminum oxide films by plasma assisted etch-through, *Thin Solid Films* **516** (2008) 5551–5556.

[112] M. D. Groner, J. W. Elam, F. H. Fabreguette, S. M. George, Electrical characterization of thin Al_2O_3 films grown by atomic layer deposition on silicon and various metal substrates, *Thin Solid Films* **413** (2002) 186–197.

[113] T. Homma, Y. Murao, Properties of liquid-phase-deposited SiO_2 films for interlayer dielectrics in ultralarge-scale integrated circuit multilevel interconnections, *Thin Solid Films* **249** (1994) 15–21.

[114] S. Kulmala, J. Suomi, Current status of modern analytical luminescence methods, *Anal. Chim. Acta* **500** (2003) 21–69.

[115] D. R. Lide (editor), *CRC Handbook of Chemistry and Physics*, CRC Press, Boca Raton, 76th edition, 1995.

[116] M. J. Bronskill, R. K. Wolff, J. W. Hunt, Picosecond pulse radiolysis studies. I. The solvated electron in aqueous and alcohol solutions, *J. Chem. Phys.* **53** (1970) 4201–4210.

[117] M. J. Bronskill, R. K. Wolff, J. W. Hunt, Picosecond pulse radiolysis studies. II. Reactions of electrons with concentrated scavengers, *J. Chem. Phys.* **53** (1970) 4211–4215.

[118] Y. Muroya, M. Lin, Z. Han, Y. Kumagai, A. Sakumi, T. Ueda, Y. Katsumura, Ultra-fast pulse radiolysis: A review of the recent system progress and its application to study on initial yields and solvation processes of solvated electrons in various kinds of alcohols, *Radiat. Phys. Chem.* **77** (2008) 1176–1182.

[119] A. Migus, Y. Gauduel, J. L. Martin, A. Antonetti, Excess electrons in liquid water: First evidence of a prehydrated state with femtosecond lifetime, *Phys. Rev. Lett.* **58** (1987) 1559–1562.

[120] R. Laenen, T. Roth, A. Laubereau, Novel precursors of solvated electrons in water: Evidence for a charge transfer process, *Phys. Rev. Lett.* **85** (2000) 50–53.

[121] J. W. Boag, E. J. Hart, Absoprtion spectra in irradiated water and some solutions — Absorption spectra of hydrated electron, *Nature* **197** (1963) 45–47.

[122] J. P. Keene, Absoprtion spectra in irradiated water and some solutions — Optical absorptions in irradiated water, *Nature* **197** (1963) 47–48.

[123] P. Pavan, R. Bez, P. Olivo, E. Zanoni, Flash memory cells — An overview, *Proc. IEEE* **85** (1997) 1248–1271.

[124] E. W. Cowell III, N. Alimardani, C. C. Knutson, J. F. Conley Jr., D. A. Keszler, B. J. Gibbons, J. F. Wager, Advancing MIM electronics: Amorphous metal electrodes, *Adv. Mater.* **23** (2011) 74–78.

[125] C. A. Mead, Operation of tunnel-emission devices, *J. Appl. Phys.* **32** (1961) 646–652.

[126] J. Cohen, Tunnel emission into vacuum, *J. Appl. Phys.* **33** (1962) 1999–2000.

[127] G. V. Buxton, C. L. Greenstock, W. P. Helman, A. B. Ross, Critical review of rate constants for reactions of hydrated electrons, hydrogen atoms and hydroxyl radicals ($\cdot$OH/$\cdot$O$^-$) in aqueous solution, *J. Phys. Chem. Ref. Data* **17** (1988) 513–886.

[128] M. Håkansson, M. Helin, M. Putkonen, Q. Jiang, M. Kotiranta, J. Suomi, A. J. Niskanen, T. Ala-Kleme, S. Kulmala, Electrochemiluminescence of Tb(III) chelates at optically transparent tunnel emission electrodes fabricated by atomic layer deposition, *Anal. Chim. Acta* **541** (2005) 137–141.

[129] S. Kulmala, A. Kulmala, M. Helin, I. Hyppänen, Hot electron-induced time-

resolved electrogenerated luminescence of Tb(III) ions at stationary oxide-covered aluminium electrodes, *Anal. Chim. Acta* **359** (1998) 71–86.

[130] S. Kulmala, M. Helin, T. Ala-Kleme, L. Väre, D. Papkovsky, T. Korpela, A. Kulmala, Electrochemiluminescent labels for applications in fully aqueous solutions at oxide-covered aluminium electrodes, *Anal. Chim. Acta* **386** (1999) 1–6.

[131] J. Eskola, P. Mäkinen, L. Oksa, K. Loikas, M. Nauma, Q. Jiang, M. Håkansson, J. Suomi, S. Kulmala, Competitive immunoassay by hot electron-induced electrochemiluminescence detection and using a semiautomatic electrochemiluminometer, *J. Lumin.* **118** (2006) 238–244.

[132] S. Kulmala, A. Kulmala, T. Ala-Kleme, J. Pihlaja, Primary cathodic steps of electrogenerated chemiluminescence of lanthanide(III) chelates at oxide-covered aluminum electrodes in aqueous solution, *Anal. Chim. Acta* **367** (1998) 17–31.

[133] S. Kulmala, M. Håkansson, A.-M. Spehar, A. Nyman, J. Kankare, K. Loikas, T. Ala-Kleme, J. Eskola, Heterogeneous and homogeneous electrochemiluminoimmunoassays of hTSH at disposable oxide-covered aluminum electrodes, *Anal. Chim. Acta* **458** (2002) 271–280.

[134] S. Kulmala, T. Ala-Kleme, Room temperature phosphorescence emission in fully aqueous medium induced by injection of hot electrons into an electrolyte solution, *Anal. Chim. Acta* **355** (1997) 1–5.

[135] M. Håkansson, Q. Jiang, M. Putkonen, A. J. Niskanen, S. Pahlberg, T. Ala-Kleme, L. Heikkilä, J. Suomi, S. Kulmala, Cathodic Tb(III) chelate electrochemiluminescence at oxide-covered magnesium and n-ZnO:Al/MgO composite electrodes, *Electrochim. Acta* **51** (2005) 289–296.

[136] T. Ala-Kleme, S. Kulmala, M. Latva, Generation of free radicals and electrochemiluminescence at pulse-polarized oxide-covered silicon electrodes in aqueous solutions, *Acta Chem. Scand.* **51** (1997) 541–546.

[137] M. Helin, L. Väre, M. Håkansson, P. Canty, H.-P. Hedman, L. Heikkilä, T. Ala-Kleme, J. Kankare, S. Kulmala, Electrochemiluminoimmunoassay of hTSH at disposable oxide-coated n-silicon electrodes, *J. Electroanal. Chem.* **524–525** (2002) 176–183.

[138] T. Ala-Kleme, P. Mäkinen, T. Ylinen, L. Väre, S. Kulmala, P. Ihalainen, J. Peltonen, Rapid electrochemiluminoimmunoassay of human C-reactive protein at planar disposable oxide-coated silicon electrodes, *Anal. Chem.* **78** (2006) 82–88.

[139] A. J. Niskanen, T. Ylinen-Hinkka, S. Kulmala, S. Franssila, Ultrathin tunnel insulator films on silicon for electrochemiluminescence studies, *Thin Solid Films* **517** (2009) 5779–5782.

[140] A. J. Niskanen, T. Ylinen-Hinkka, M. Pusa, S. Kulmala, S. Franssila, De-

posited dielectrics on metal thin films using silicon and glass substrates for hot electron-induced electrochemiluminescence, *Thin Solid Films* **519** (2010) 430–433.

[141] S. Kulmala, T. Ala-Kleme, M. Latva, K. Loikas, H. Takalo, Hot electron-induced electrogenerated chemiluminescence of rare earth (III) chelates at oxide-covered aluminum electrodes, *J. Fluoresc.* **8** (1998) 59–65.

[142] Q. Jiang, M. Håkansson, A.-M. Spehar, J. Ahonen, T. Ala-Kleme, S. Kulmala, Hot electron-induced time-resolved electrogenerated chemiluminescence of a europium(III) label in fully aqueous solutions, *Anal. Chim. Acta* **558** (2006) 302–309.

[143] T. Ala-Kleme, K. Haapakka, M. Latva, Near-infrared electrogenerated chemiluminescence of ytterbium(III) chelates in aqueous electrolytes, *Anal. Chim. Acta* **395** (1999) 205–211.

[144] T. Ala-Kleme, S. Kulmala, L. Väre, P. Juhala, M. Helin, Hot electron-induced electrogenerated chemiluminescence of $Ru(bpy)_3^{2+}$ chelate at oxide-covered aluminum electrodes, *Anal. Chem.* **71** (1999) 5538–5543.

[145] Q. Jiang, J. Suomi, M. Håkansson, A. J. Niskanen, M. Kotiranta, S. Kulmala, Cathodic electrogenerated chemiluminescence of $Ru(bpy)_3^{2+}$ chelate at oxide-coated heavily doped silicon electrodes, *Anal. Chim. Acta* **541** (2005) 159–165.

[146] Q. Jiang, H. Ketamo, A. J. Niskanen, J. Suomi, M. Håkansson, S. Kulmala, Effects of thermal oxidation conditions of silicon electrodes on cathodic electrochemiluminescence of $Ru(bpy)_3^{2+}$ chelate, *Electrochim. Acta* **51** (2006) 3332–3337.

[147] Q. Jiang, S. Sun, M. Håkansson, K. Langel, T. Ylinen, J. Suomi, S. Kulmala, Electrochemiluminescence and chemiluminescence of a carboxylic acid derivative of ruthenium(II) tris-(2,2′-bipyridine) chelate synthesized for labeling purposes, *J. Lumin.* **118** (2006) 265–271.

[148] T. Ala-Kleme, K. Haapakka, M. Latva, Y(III)-enhanced Dy(III) and Sm(III)-specific electrogenerated luminescence of heterodinuclear 1-Y(III)-Dy(III)-1 and 1-Y(III)-Sm(III)-1 chelates, *J. Alloys Compd.* **275–277** (1998) 911–914.

[149] P. Canty, L. Väre, M. Håkansson, A.-M. Spehar, D. Papkovsky, T. Ala-Kleme, J. Kankare, S. Kulmala, Time-resolved electrochemiluminescence of platinum(II) coproporphyrin, *Anal. Chim. Acta* **453** (2002) 269–279.

[150] T. Ylinen, J. Suomi, M. Helin, T. Ala-Kleme, S. Kulmala, Time-resolved detection of hot electron-induced electrochemiluminescence of fluorescein in aqueous solution, *J. Fluoresc.* **16** (2006) 27–33.

[151] J. Suomi, T. Ylinen, M. Håkansson, M. Helin, Q. Jiang, T. Ala-Kleme, S. Kulmala, Hot electron-induced electrochemiluminescence of fluorescein in aqueous solution, *J. Electroanal. Chem.* **586** (2006) 49–55.

[152] S. Kulmala, T. Ala-Kleme, A. Kulmala, D. Papkovsky, K. Loikas, Cathodic electrogenerated chemiluminescence of luminol at disposable oxide-covered aluminum electrodes, *Anal. Chem.* **70** (1998) 1112–1118.

[153] J. Suomi, M. Håkansson, Q. Jiang, M. Kotiranta, M. Helin, A. J. Niskanen, S. Kulmala, Time-resolved detection of electrochemiluminescence of luminol, *Anal. Chim. Acta* **541** (2005) 167–169.

[154] Q. Jiang, M. Håkansson, J. Suomi, T. Ala-Kleme, S. Kulmala, Cathodic electrochemiluminescence of lucigenin at disposable oxide-coated aluminum electrodes, *J. Electroanal. Chem.* **591** (2006) 85–92.

[155] Q. Jiang, A.-M. Spehar, M. Håkansson, J. Suomi, T. Ala-Kleme, S. Kulmala, Hot electron-induced cathodic electrochemiluminescence of rhodamine B at disposable oxide-coated aluminum electrodes, *Electrochim. Acta* **51** (2006) 2706–2714.

[156] A.-M. Spehar-Deleze, J. Suomi, Q. Jiang, N. de Rooij, M. Koudelka-Hep, S. Kulmala, Heterogeneous oligonucleotide-hybridization assay based on hot electron-induced electrochemiluminescence of a rhodamine label at oxide-coated aluminum and silicon electrodes, *Electrochim. Acta* **51** (2006) 5438–5444.

[157] M. Helin, Q. Jiang, H. Ketamo, M. Håkansson, A.-M. Spehar, S. Kulmala, T. Ala-Kleme, Electrochemiluminescence of coumarin derivatives induced by injection of hot electrons into aqueous electrolyte solution, *Electrochim. Acta* **51** (2005) 725–730.

[158] M. Helin, M. Håkansson, P. Canty, A.-M. Spehar, S. Kulmala, Hot electron-induced electrogenerated chemiluminescence of 1-aminonaphthalene-4-sulphonate at oxide-covered aluminium electrodes in aqueous solution, *Anal. Chim. Acta* **454** (2002) 193–201.

[159] I. Díez, M. Pusa, S. Kulmala, H. Jiang, A. Walther, A. S. Goldmann, A. H. E. Müller, O. Ikkala, R. H. A. Ras, Color tunability and electrochemiluminescence of silver nanoclusters, *Angew. Chem. Int. Ed.* **48** (2009) 2122–2125.

[160] A. E. Bolton, W. M. Hunter, The labelling of proteins to high specific radioactivities by conjugation to a ^{125}I-containing acylating agent, *Biochem. J.* **133** (1973) 529–539.

[161] L. M. Smith, J. Z. Sanders, R. J. Kaiser, P. Hughes, C. Dodd, C. R. Connell, C. Heiner, S. B. H. Kent, L. E. Hood, Fluorescence detection in automated DNA sequence analysis, *Nature* **321** (1986) 674–679.

[162] B.-W. Ying, D. Fourmy, S. Yoshizawa, Substitution of the use of radioactivity by fluorescence for biochemical studies of RNA, *RNA* **13** (2007) 2042–2050.

[163] G. L. Igloi, Strategies for introducing non-radioactive labels during the automated sequence analysis of nucleic acids, *Electron. J. Biotechnol.* **1** (1998) 23–30.

[164] H. Wu, Q. Huo, S. Varnum, J. Wang, G. Liu, Z. Nie, J. Liu, Y. Lin, Dye-doped silica nanoparticle labels/protein microarray for detection of protein biomarkers, *Analyst* **133** (2008) 1550–1555.

[165] S. X. Wang, G. Li, Advances in giant magnetoresistance biosensors with magnetic nanoparticle tags: Review and outlook, *IEEE Trans. Magn.* **44** (2008) 1687–1702.

[166] G. Liu, J. Wang, H. Wu, Y. Lin, Y. Lin, Nanovehicles based bioassay labels, *Electroanalysis* **19** (2007) 777–785.

[167] A.-M. Spehar-Deleze, L. Schmidt, R. Neier, S. Kulmala, N. de Rooij, M. Koudelka-Hep, Electrochemiluminescent hybridization chip with electric field aided mismatch discrimination, *Biosensors and Bioelectronics* **22** (2006) 722–729.

[168] S. Kulmala, Personal communication, 2010.

[169] E. P. Diamandis, Analytical methodology for immunoassays and DNA hybridization assays — Current status and selected systems — Critical review, *Clin. Chim. Acta* **194** (1990) 19–50.

[170] M. Håkansson, Q. Jiang, J. Suomi, K. Loikas, M. Nauma, T. Ala-Kleme, J. Kankare, P. Juhala, J. U. Eskola, S. Kulmala, Cathodic electrochemiluminescence at double barrier $Al/Al_2O_3/Al/Al_2O_3$ tunnel emission electrodes, *Anal. Chim. Acta* **556** (2006) 450–454.

[171] A.-H. Wu, J.-J. Sun, Y.-M. Fang, X.-L. Su, G.-N. Chen, Hot electron induced cathodic electrochemiluminescence at AuSb alloy electrode for fabricating immunosensor with self-assembled monolayers, *Talanta* **82** (2010) 1455–1461.

[172] A.-H. Wu, J.-J. Sun, R.-J. Zheng, H.-H. Yang, G.-N. Chen, A reagentless DNA biosensor based on cathodic electrochemiluminescence at a C/C_xO_{1-x} electrode, *Talanta* **81** (2010) 934–940.

[173] S. Götz, U. Karst, Recent developmens in optical detection methods for microchip separations, *Anal. Bioanal. Chem.* **387** (2007) 183–192.

[174] B. Kuswandi, Nuriman, J. Huskens, W. Verboom, Optical sensing systems for microfluidic devices: A review, *Anal. Chim. Acta* **601** (2007) 141–155.

[175] MicroChem Corp., Newton, MA., *SU-8 Permanent Photoresists*, `http://www.microchem.com/products/pdf/SU-8 3000 Data Sheet.pdf`.

[176] S. Aura, T. Sikanen, T. Kotiaho, S. Franssila, Novel hybrid material for microfluidic devices, *Sens. Actuators, B* **132** (2008) 397–403.

[177] S. H. Tan, N.-T. Nguyen, Y. C. Chua, T. G. Kang, Oxygen plasma treatment for reducing hydrophobicity of a sealed polydimethylsiloxane microchannel, *Biomicrofluidics* **4** (2010) 032204.1–032204.8.

[178] A. Hierlemann, H. Baltes, CMOS-based chemical microsensors, *Analyst* **128** (2003) 15–28.

[179] D. Kohl, Function and applications of gas sensors, *J. Phys. D* **34** (2001) R125–R149.

[180] M. Batzill, U. Diebold, The surface and materials science of tin oxide, *Prog. Surf. Sci.* **79** (2005) 47–154.

[181] G. Eranna, B. C. Joshi, D. P. Runthala, R. P. Gupta, Oxide materials for development of integrated gas sensors — A comprehensive review, *Crit. Rev. Solid State Mater. Sci.* **29** (2004) 111–188.

[182] N. Barsan, U. Weimar, Conduction model of metal oxide gas sensors, *J. Electroceram.* **7** (2001) 143–167.

[183] M. K. Kennedy, F. E. Kruis, H. Fissan, Tailored nanoparticle films from monosized tin oxide nanocrystals: Particle synthesis, film formation, and size-dependent gas-sensing properties, *J. Appl. Phys.* **93** (2003) 551–560.

[184] S. Semancik, R. E. Cavicchi, M. C. Wheeler, J. E. Tiffany, G. E. Poirier, R. M. Walton, J. S. Suehle, B. Panchapakesan, D. L. DeVoe, Microhotplate platforms for chemical sensor research, *Sens. Actuators, B* **77** (2001) 579–591.

[185] A. P. Lee, B. J. Reedy, Temperature modulation in semiconductor gas sensing, *Sens. Actuators, B* **60** (1999) 35–42.

[186] R. Gutierrez-Osuna, A. Gutierrez-Galvez, N. Powar, Transient response analysis for temperature-modulated chemoresistors, *Sens. Actuators, B* **93** (2003) 57–66.

[187] Y. Shen, T. Yamazaki, Z. Liu, C. Jin, T. Kikuta, N. Nakatani, Porous SnO_2 sputtered films with high H_2 sensitivity at low operation temperature, *Thin Solid Films* **516** (2008) 5111–5117.

[188] M. C. Horrillo, P. Serrini, J. Santos, L. Manes, Influence of the deposition conditions of SnO_2 thin films by reactive sputtering on the sensitivity to urban pollutants, *Sens. Actuators, B* **45** (1997) 193–198.

[189] J. R. Brown, P. W. Haycock, L. M. Smith, A. C. Jones, E. W. Williams, Response behaviour of thin oxide thin film gas sensors grown by MOCVD, *Sens. Actuators, B* **63** (2000) 109–114.

[190] Y. Zhao, Z. Feng, Y. Liang, SnO_2 gas sensor films deposited by pulsed laser ablation, *Sens. Actuators, B* **56** (1999) 224–227.

[191] H.-H. Park, H.-H. Park, R. H. Hill, Direct-patterning of SnO_2 thin film by photochemical metal-organic deposition, *Sens. Actuators, A* **132** (2006) 429–433.

[192] C. Zhang, K. Najafi, Fabrication of thick silicon dioxide layers for thermal isolation, *J. Micromech. Microeng.* **14** (2004) 769–774.

[193] D. N. Pagonis, G. Kaltsas, A. G. Nassiopoulou, Fabrication and testing of an integrated thermal flow sensor employing thermal isolation by a porous silicon

membrane over an air cavity, *J. Micromech. Microeng.* **14** (2004) 793–797.

[194] I. Simon, N. Bârsan, M. Bauer, U. Weimar, Micromachined metal oxide gas sensors: Opportunities to improve sensor performance, *Sens. Actuators, B* **73** (2001) 1–26.

[195] F. Rettig, R. Moos, Direct thermoelectric hydrocarbon gas sensors based on SnO_2, *IEEE Sens. J.* **7** (2007) 1490–1496.

[196] G. Natarajan, D. C. Cameron, Influence of oxygen depletion layer on the properties of tin oxide gas-sensing films fabricated by atomic layer deposition, *Appl. Phys. A* **95** (2009) 621–627.

[197] P. W. Simon, Etchant and method of etching tin oxide film, U.S. Pat. 4,009,061, 1977.

Appendix A HECL chip fabrication process

The HECL devices are processed using economical plastic film photomasks, of the type used in printed circuit board production. This enables fast turnaround of prototype devices. The minimum linewidths and alignment tolerances between masklevels were 100 µm, although patterns down to approximately 20 µm could be realized with plastic masks. Since the plastic film is not as uniformly transparent as glass photomasks, significant overexposure is required to avoid photoresist residues in exposed areas. Likewise slight overdevelopment is used. At these linewidths, however, overexposure and overdevelopment pose no problems.

A.1 Silicon devices

1. Wafer selection: 100 mm, n^+ type, 0.005–0.018 Ω·cm, (111) orientation, single-side polished
2. RCA-cleaning
   - 10 minutes SC-1 (5:1:1 $H_2O : NH_4OH : H_2O_2$ at 80°C), DI-water rinse
   - 15 minutes SC-2 (5:1:1 $H_2O : HCl : H_2O_2$ at 80°C), DI-water rinse
   - 30 seconds 50:1 $H_2O : HF$ at RT, DI-water rinse
   - Drying
3. Field oxide growth: Centrotherm furnace, wet oxidation, 950°C, 90 minutes

   $\Longrightarrow$ Approx. 380 nm oxide thickness measured by ellipsometer
4. Photolithography (Field oxide mask)
   - Oven baking, 120°C, 10 minutes
   - HMDS-priming, 10 minutes in vacuum desiccator
   - AZ5214 E photoresist spinning, 4 000 rpm, 30 seconds
   - Oven baking, 90°C, 20 minutes
   - Exposure, plastic photomask, 4 seconds (Süss Microtec MA-6)
   - Development, 1:5 AZ351 B : H_2O, 1 minute
   - Rinsing, drying
   - Oven baking, 120°C, 30 minutes
5. Field oxide etching: SioEtch BHF, 32°C, 4 minutes, rinsing, drying
6. Photoresist removal
   - 10 minutes, acetone in ultrasonic bath
   - Rinse in clean acetone
   - Rinse in clean isopropanol
   - DI water rinse, drying
7. RCA-cleaning as in step 2

8. Tunnel oxide growth: Centrotherm furnace, dry oxidation, 850°C, 10% oxygen
   - Loading at 700°C
   - Ramp to 850°C at 10°C/min in 5% oxygen
   - Oxidation 20 minutes at 850°C in 10% oxygen, 90% nitrogen
   - Annealing 30 minutes at 850°C in 100% nitrogen
   - Ramp to 700°C at 4°C/min in nitrogen, unloading

   $\Longrightarrow$ Approx. 4 nm oxide thickness measured by ellipsometer
9. Photolithography (Pt lift-off mask) as in step 4
10. Sputtering of platinum: Oxford PlasmaLab System 400
    - Chromium adhesion layer: 10 seconds, 200 W, 50 sccm argon
    - Platinum: 15 seconds, 500 W, 70 sccm argon

    $\Longrightarrow$ Approx. 50 nm total thickness measured by profilometer
11. Lift-off of platinum
    - 30 minutes, acetone in ultrasonic bath
    - 10 minutes, clean isopropanol in ultrasonic bath
    - DI water rinse, drying
12. Protection of wafer front side with photoresist
    - Oven baking, 120°C, 10 minutes
    - HMDS-priming, 10 minutes in vacuum desiccator
    - AZ5214 E photoresist spinning, 4 000 rpm, 30 seconds
    - Oven baking, 120°C, 30 minutes
13. Oxide etching from wafer backside: SioEtch BHF, 32°C, 1 minute, rinsing, drying
14. Sputtering of aluminum on backside: Oxford PlasmaLab System 400, 1 minute, 1 000 W, 70 sccm argon
15. Photoresist removal as in step 6

Steps 16–18 only for devices with hydrophobic sample confinement:

16. Photolithography (hydrophobic lift-off mask) as in step 4
17. Fluoropolymer deposition: Oxford PlasmaLab 80+, 5 minutes, 50 W, 100 sccm CHF_3 $\Longrightarrow$ $\sim$30 nm film
18. Liftoff of fluoropolymer as in step 11

19. Wafer dicing

A.2 Glass devices

1. Wafer selection: 100 mm borosilicate glass
2. Partial RCA-cleaning
   - 10 minutes SC-1 (5:1:1 $H_2O : NH_4OH : H_2O_2$ at 80°C)
   - DI-water rinse, drying
3. Sputtering of aluminum: Oxford PlasmaLab System 400, 1 minute 15 seconds, 2 000 W, 70 sccm argon

   $\Longrightarrow$ Approx. 400 nm thickness measured by profilometer
4. Photolithography (Platinum lift-off mask) as in A.1, step 4
5. Wet etching of aluminum: PS 80-16-04 etchant, 2 minutes at 50°C (approx. 100% overetch)
6. Sputtering of platinum as in A.1, step 10
7. Lift-off of platinum as in A.1, step 11
8. Photolithography (Aluminum electrode mask) as in A.1, step 4
9. Wet etching of aluminum: PS 80-16-04 etchant, 1 minute at 50°C
10. Photoresist removal as in A.1, step 6
11. Atomic layer deposition of Al_2O_3: Beneq TFS-500, 40 A-B cycles of TMA and H_2O at 210°C
12. Photolithography (Tunnel dielectric mask) as in A.1, step 4
    - Development time of 3 minutes: Overdevelopment etches Al_2O_3 film
13. Photoresist removal as in A.1, step 6
14. Wafer dicing

A.3 PDMS fluidics

The master mold is fabricated of SU-8 epoxy on a silicon wafer in a single masklevel process, using a plastic film photomask. The type of wafer is not critical. A single mold can be used for casting multiple copies in PDMS.

1. Wafer selection: any polished silicon wafer
2. Oxide removal: SioEtch BHF, 32°C, 1 minute, rinsing, drying
3. Bake 120°C, 30 minutes
4. Dispense SU-8 100, spin 30 seconds at 1 000 rpm (∼350 µm layer)
5. Prebake on hotplate
   - Ramp from RT to 65°C in 3 min
   - Bake at 65°C for 25 min

   - Ramp from 65°C to 95°C in 3 min
   - Bake at 95°C for 150 min
   - Ramp to RT

6. Exposure, plastic photomask, 85 seconds (Süss Microtec MA-6)
7. Postbake on hotplate
   - Ramp from RT to 95°C in 5 min
   - Bake at 95°C for 40 min
   - Ramp to RT
8. Development with SU-8 developer while agitating, approx. 30 minutes or until unexposed areas are fully removed
9. Rinse with clean SU-8 developer
10. Rinse with clean isopropanol, drying
11. Fluoropolymer deposition as in A.1, step 17

The PDMS lids are made outside the cleanroom by casting an approximately 2 mm thick layer of PDMS over the master mold in a Petri dish.

12. Casting of PDMS on master mold: Sylgard 184 elastomer mixed in 10:1 ratio (base and curing agent)
13. Outgassing of PDMS in vacuum desiccator, 20 minutes
14. Oven curing of PDMS, 50°C, 2 hours
15. Peeling of PDMS from master, dicing manually with a knife
16. Plasma treatment of PDMS lids and HECL chips: Technics Plasma GmbH[†] TePla-400, 30 seconds, 800 W, 800 sccm O_2
17. Bonding of PDMS lids to HECL chips: manual alignment and finger pressure for 5 seconds
18. (If necessary) Trimming of PDMS from bonded device with a knife
19. (If necessary) Re-activation by oxygen plasma as in step 16

[†]Now PVA TePla AG.

Appendix B Gas sensor fabrication process

The *Lakana* microhotplate gas sensor fabrication process uses up to eight masklevels. Five photomasks are standard glass/chromium masks, while three have more relaxed linewidth requirements and use cheaper plastic film masks. These require a longer exposure time due to lower transparency and imperfections.

1. Wafer selection (not critical): 100 mm, *p*-type, 5–7 Ω·cm, (100) orientation, double-side polished
2. RCA-cleaning
   - 10 minutes 5:1:1 $H_2O : NH_4OH : H_2O_2$ at 80°C, DI-water rinse
   - 15 minutes 5:1:1 $H_2O : HCl : H_2O_2$ at 80°C, DI-water rinse
   - 30 seconds 50:1 $H_2O : HF$ at RT, DI-water rinse
   - Drying
3. Oxidation: Centrotherm furnace, wet oxidation, 1 000°C, 80 minutes

   $\Longrightarrow$ 416 nm thickness measured by ellipsometer
4. Silicon nitride LPCVD: 770°C, 70 minutes

   $\Longrightarrow$ 263 nm thickness measured by ellipsometer
5. Sputtering of tungsten: Oxford PlasmaLab System 400
   - Tungsten nitride: dynamic, 5 rpm, 600 W, 30 sccm Ar, 100 sccm N_2, 1 min
   - Tungsten: dynamic, 5 rpm, 500 W, 70 sccm Ar, 19 min
   - Tungsten nitride: dynamic, 5 rpm, 600 W, 30 sccm Ar, 100 sccm N_2, 1 min

   $\Longrightarrow$ 210–220 nm thickness measured by profilometer
6. Photolithography (Heater resistor mask)
   - Oven baking, 120°C, 10 minutes
   - HMDS-priming, 10 minutes in vacuum desiccator
   - AZ5214 E photoresist spinning, 4 000 rpm, 30 seconds
   - Oven baking, 90°C, 20 minutes
   - Exposure, 4.5 seconds (Electronic Visions AL-6)
   - Development, 1:5 AZ351 B : H_2O, 1 minute
   - Rinsing, drying
   - Oven baking, 120°C, 30 minutes
7. Tungsten etching: Oxford PlasmaLab 80+, 100 W, 100 sccm SF_6, 100 mTorr, 2 min 10 s
8. Photoresist removal
   - 10 minutes, acetone in ultrasonic bath
   - Rinse in clean acetone

- Rinse in clean isopropanol
- DI water rinse, drying
- Oxygen plasma: Oxford PlasmaLab 80+, 50 W, 45 sccm O_2, 250 mTorr, 1 min

9. Silicon dioxide PECVD: Oxford PlasmaLab 80+, 20 W, 8.5 sccm SiH_4, 710 sccm N_2O, 161.5 sccm N_2, 1 000 mTorr, 350°C, 5 min

   $\Longrightarrow$ ∼325 nm thickness measured by ellipsometer from reference wafer

10. Annealing in nitrogen atmosphere:

    - Ramping from 300°C to 500°C at 1.7°C/min
    - Annealing at 500°C for 24 h
    - Ramping from 500°C to 300°C at 1.7°C/min

Steps 11–16 only for devices with intermediate electrode:

11. Sputtering of tungsten: Oxford PlasmaLab System 400

    - Tungsten nitride: dynamic, 5 rpm, 600 W, 30 sccm Ar, 100 sccm N_2, 1 min
    - Tungsten: dynamic, 5 rpm, 500 W, 70 sccm Ar, 9.5 min
    - Tungsten nitride: dynamic, 5 rpm, 600 W, 30 sccm Ar, 100 sccm N_2, 1 min

    $\Longrightarrow$ 110–120 nm thickness measured by profilometer

12. Photolithography (Intermediate electrode mask) as in step 6

13. Tungsten etching: Oxford PlasmaLab 80+, 100 W, 100 sccm SF_6, 100 mTorr, 1 min 15 s

14. Resist removal as in step 8

15. Silicon dioxide PECVD as in step 9

    $\Longrightarrow$ ∼325 nm thickness measured by ellipsometer from reference wafer

16. Annealing as in step 10

17. Photolithography (1. contact hole mask) as in step 6

18. Oxide etching: SioEtch BHF, 32°C

    With intermediate electrode: etching 1 min 10 s, rinsing, drying
    $\Longrightarrow$ ≥640 nm total depth measured by profilometer

    Without intermediate electrode: etching 40 s, rinsing, drying
    $\Longrightarrow$ ≥340 nm depth measured by profilometer

19. Photoresist removal:

    - 10 minutes, acetone in ultrasonic bath
    - Rinse in clean acetone

- Rinse in clean isopropanol
- DI water rinse, drying

Steps 20–22 only for devices with intermediate electrode:

20. Photolithography (2. contact hole mask) as in step 6
21. Oxide etching: SioEtch BHF, 32°C, 40 s, rinsing, drying

    $\Longrightarrow$ $\geq$340 nm depth measured by profilometer
22. Photoresist removal as in step 19

23. Protection of wafer front side with photoresist
    - Oven baking, 120°C, 10 minutes
    - HMDS-priming, 10 minutes in vacuum desiccator
    - AZ5214 E photoresist spinning, 4 000 rpm, 30 seconds
    - Oven baking, 120°C, 20 minutes
24. Backside photolithography (Nitride hole mask) as in step 6
    - Plastic photomask, exposure time 9.0 s
25. Silicon nitride etching: Oxford PlasmaLab 80+, 150 W, 50 sccm CHF_3, 5 sccm O_2, 55 mTorr, 7 min

Steps 26–28 only for devices with a silicon island under the MHP:

26. Photoresist removal as in step 19
27. Protection of wafer front side with photoresist as in step 23
28. Backside photolithography (Oxide hole mask) as in step 6
    - Plastic photomask, exposure time 9.0 s

29. Oxide etching: SioEtch BHF, 32°C, 5 min, rinsing, drying
30. Photoresist removal as in step 19
31. Wafer front side cleaning by oxygen plasma: Oxford PlasmaLab 80+, 50 W, 45 sccm O_2, 250 mTorr, 10 s
32. Gold sputtering with TiW adhesion layer (done at VTT[†]), $\sim$480 nm
33. Photolithography (Electrode mask) as in step 6

[†]VTT Technical Research Center of Finland, Micronova, Espoo.

34. Gold etching
    - 4:4:1 $H_2O : HCl : HNO_3$, 45 s, DI-water rinse, drying
35. Photoresist removal as in step 19
36. TiW etching
    - 1:1 $H_2O_2 : H_2O$, 2 min, DI-water rinse, drying
37. Particle removal: 10 min, DI-water in ultrasonic bath, DI-water rinse, drying
38. Tin dioxide deposition by ALD, $SnCl_4$ and H_2O at 500°C (done at ASTRaL[†])
39. Photolithography (Contact mask) as in step 6
    - Plastic photomask, exposure time 9.0 s
40. Tin dioxide etching: described elsewhere [197]
41. Photoresist removal as in step 19
42. Wafer front side protection:
    - Spin ProTEK® Primer, 1500 rpm, 60 s
    - Bake on hotplate: 150°C, 60 s
    - Spin ProTEK® B1-18, 1 000 rpm, 90 s
    - Bake on hotplate: 115°C, 120 s; 160°C, 120 s; 205°C, 60 s

Steps 43–44 only for devices with a silicon island under the MHP:

43. Backside etching: 20% KOH solution, 90°C, 20 min, rinsing
44. Oxide etching: SioEtch BHF, RT, 5 min, rinsing

45. Backside etching: 20% KOH solution, 90°C

    With silicon island under the MHP: etching approx. 2 h 30 min, until through-etched, rinsing, drying

    Without silicon island under the MHP: etching approx. 3 h, until through-etched, rinsing, drying
46. Wafer dicing
47. ProTEK® removal: acetone 10 min, rinse in isopropanol, rinse in water, drying
48. Chip packaging

[†]Advanced Surface Technology Research Laboratory (ASTRaL), Lappeenranta University of Technology, Mikkeli.

Errata

In Publication **III**, at the end of section 2, measurements were performed in a 5.6 mm diameter sample cell (not 8 mm), and luminescence was measured after a 50 µs delay following the pulse (not 50 s).

Due to limitations of the HECL measurement setup, luminescence data is recorded only from every second pulse applied. The x-axes of Figures 5 and 6 in Publication **III**, Figures 3 and 5 in Publication **IV** and Figure 6 in Publication **V** do not reflect this fact, and their values should thus be $2\times$ those shown. Likewise, the corresponding numerical values presented in sections 3.2 and 4 of Publication **III** are a factor of 2 too small. The numerical values concerning dielectric stability in Section 3.2 of Publication **IV** are, however, correct.

In Publication **V**, the word "Hydrofobic" in the legend of Figure 7 should be spelled "Hydrophobic".

In Publication **VI**, the fabrication process described in Section 2.1 is missing the patterning steps of the intermetal dielectric (steps 17–19 of the process described in Appendix B).

Aalto-DD 146/2011

ISBN 978-952-60-4450-7
ISBN 978-952-60-4451-4 (pdf)
ISSN-L 1799-4934
ISSN 1799-4934
ISSN 1799-4942 (pdf)

Aalto University
School of Electrical Engineering
Department of Micro and Nanosciences
www.aalto.fi

BUSINESS +
ECONOMY

ART +
DESIGN +
ARCHITECTURE

SCIENCE +
TECHNOLOGY

CROSSOVER

DOCTORAL
DISSERTATIONS